Operational Modal Analysis and its Application for SOFIA Telescope Assembly Vibration Measurements

Operationelle Modalanalyse und ihre Anwendung bei Vibrationsmessungen des SOFIA Teleskops

Studienarbeit von

cand. aer. Benjamin Greiner

IRS-09-S43

Institut für Raumfahrtsysteme, Universität Stuttgart

Dezember 2009

UNIVERSITÄT STUTTGART
INSTITUT FÜR RAUMFAHRTSYSTEME
Direktor: Prof. Dr. Hans-Peter Röser
Pfaffenwaldring 31 · 70569 Stuttgart · Tel.: (0711) 685-62375 · Fax: (0711) 685-63596
www.irs.uni-stuttgart.de

Studienarbeit

für Herrn cand. aer. Benjamin Greiner
Matr. Nr. 2207607

Operational Modal Analysis and its Application for SOFIA Telescope Assembly Vibration Measurements

Operationelle Modalanalyse und ihre Anwendung bei Vibrationsmessungen des SOFIA Teleskops

Thema der Arbeit:

Das Verfahren der operationellen Modalanalyse (OMA) eignet sich gut zur Bestimmung der dynamischen Eigenschaften des SOFIA Teleskops unter realistischen Betriebsbedingungen im Flug. Zu diesem Zweck wurde die kommerzielle OMA Software ARTeMIS am DSI angeschafft. Ziel der Studienarbeit ist es, die hinter der Software stehenden Algorithmen zu verstehen und an einem einfachen Beispiel anzuwenden. Auf Grundlage dieses Beispiels sollen die Stärken und Schwächen der einzelnen Algorithmen ergründet werden und Schlüsse für eine zuverlässige Auswertung von Flugmessdaten der wesentlich komplexeren Teleskopstruktur gezogen werden. Ein weiteres Ziel ist die Vorbereitung der Flugdatenauswertung mit ARTeMIS, indem die Sensormessdaten in ein Gittermodell zur Darstellung der Modalformen eingebunden werden und die Formatierung der Rohmessdaten so automatisiert wird, dass eine zügige und zuverlässige Datenanalyse möglich ist.

Betreuer: Prof. Dr. Alfred Krabbe

Stuttgart, den

Ausgabe: 22. Juni 2009

Abgabe: 22. Dezember 2009

Abstract

The *Stratospheric Observatory For Infrared Astronomy, SOFIA,* is an airborne observatory that will serve the scientific community to study the universe in the infrared spectrum. SOFIA consists of a Boeing 747SP aircraft equipped with a 2.5 m telescope in the rear part of the fuselage. During operational flight, a door will be opened to allow a clear view into the sky.

One particular challenge of such an observatory in an airborne environment is to provide a highly stable image in the focal plane, where the science instrument picks up the light from the telescope. Image jitter at the focal plane is caused by external disturbance loads, e.g. aircraft inertial loads and aerodynamic loads, which cause rigid as well as flexible body motion of the telescope. Flexible body motions play an important role in the pointing optimization effort. Therefore, a good understanding of the dynamic characteristics of the telescope structure needs to be generated.

This study thesis discusses the methods of *Operational Modal Analysis (OMA)* in order to obtain such an understanding and shows how they can be applied to the SOFIA observatory development and improvement process with respect to pointing stabilization and image quality. *Operational Modal Analysis* acquires information about the dynamic characteristics of a structure in terms of eigenfrequencies, damping and mode shapes, without the need for explicit measurement of the vibration inducing loads. Since the exact influence of aerodynamic disturbance loads during operational flight conditions is not measureable, the OMA approach is a promising contribution the SOFIA optimization effort.

Zusammenfassung

SOFIA, das *Stratosphären Observatorium für Infrarot Astronomie*, ist ein fliegendes Observatorium, mit dem das Weltall astronomisch hautpsächlich im Bereich des Infrarotspektrums erforscht werden soll. Es handelt sich um ein umgebautes Flugzeug vom Typ Boeing 747SP, in dessen hintere Rumpfsektion ein Teleskop mit 2.5 m Spiegeldurchmesser eingebaut wurde. Eine sich im Fluge öffnende Schiebetür erlaubt dem Teleskop einen freien Blick in den Nachthimmel.

Eine der Hauptschwierigkeiten eines Flugzeugobservatoriums wie SOFIA ist, dem wissenschaftlichen Instrument in der Fokalebene des Teleskopes ein ausreichend stabiles Bild zu überreichen. Nur ein unverwackeltes Bild ermöglicht hervorragende wissenschaftliche Ergebnisse. Störungen in der Bildbewegung werden durch externe Anregungen hervorgerufen, die sowohl aus der Flugzeugbewegung kommen als auch durch aerodynamische Lasten verursacht werden, welche auf das Teleskop einwirken. Diese Störungen bewirken zum einen, dass sich ungewollt das komplette Teleskop relativ zum Sternenhimmel bewegt (Starrkörperbewegung), als auch dass die Teleskopstrukur angeregt wird zu schwingen. Der Ausgleich dieser Schwingungen spielt eine wichtige Rolle im Bemühen die Ausrichtgenauigkeit des Teleskops zu verbessern. Um dies zu erreichen, ist ein gutes Verständnis der dynamischen Eigenschaften der Teleskopstruktur von Nöten.

Die vorliegende Studienarbeit beschäftigt sich mit den Methoden der *Operationellen Modalanalyse (OMA)* als Möglichkeit dieses Verständnis zu erarbeiten. Die Arbeit zeigt, wie *Operationelle Modalanalyse* im SOFIA Projekt angewandt werden kann um die Optimierung von Ausrichtgenauigkeit und Bildqualität zu unterstützen. Mithilfe der *Operationellen Modalanalyse* können die Eigenfrequenzen, Dämpfungen und Schwingungsformen einer Struktur ermittelt werden, ohne dass dabei die anregenden Kräfte explizit gemessen werden müssen. Weil genau dieses Unterfangen während eines Fluges unter Beobachtungsbedingungen unmöglich ist – besonders die Messung der auf der Struktur räumlich verteilten aerodynamischen Lasten – erscheint der Ansatz der *Operationellen Modalanalyse* als vielversprechender Beitrag um die Leistungsfähigkeit des SOFIA Observatoriums zu optimieren.

Acknowledgments

Without the support of many people, this thesis would not have been possible. I want to thank the whole SOFIA team – the people within NASA, DLR, USRA and DSI – who gave me the opportunity to participate in such an exciting program. First of all, thanks to Professor Dr. Alfred Krabbe, who readily assumed the responsibility to act as my supervising professor, supported me in my applications for a scholarship, showed sincere interest in the topic and gave valuable input throughout the work. I also want to thank Professor Dr. Hans-Peter Röser for his support during the application process, and Professor Dr.-Ing. Jörg Wagner for his sincere interest.

Special thanks to my advisor Ulrich Lampater for offering the thesis topic and for his continuos support and very valuable advice during the work.

I want to thank the TA team located at the DAOF in Palmdale for a very exciting time during my stay. Namely the DSI guys: Dr. Thomas Keilig, Stefan Teufel, Andreas Reinacher, Simon Beckmann, Lars Riepegerste, Josef Trendelkamp, Rainer Strecker, Dr. Holger Jakob, Karsten Bosse, Nadine Hanisch, Marco Lentini, Stefan Huber and many more. The same is true for Phil Watts from USRA. I also want to thank the DSI team in Mountain View: Dr. Jürgen Wolf, Dr. Franziska Harms, Dr. Sven Schmid and Enrico Pfüller provided useful information and support.

This study thesis has been supported by the *Erich-Becker-Stiftung – Eine Stiftung der Fraport AG zur Förderung von Wissenschaft und Forschung*. I am very grateful for the financial support, which they provided in a very fast and unbureaucratic process.

Last but not least, I want to thank my parents, Andrea and Michael, for their love and support throughout my education in every way imaginable and my dear ShaVaughn for the emotional support.

Contents

Nomenclature

Acronyms

AFTIS	Advanced Flight Test Instrumentation System	page 65
ARTeMIS	Ambient Response-Testing and Modal Identification Software	page 37
CFDD	Curve-fit Frequency Domain Decomposition	page 17
CONM2	Concentrated mass element in the FEM software Nastran	page 50
CSV	Comma-separated values text file	page 65
DAOF	Dryden Aircraft Operations Facility	page 2
DFRC	Dryden Flight Research Center	page 2
DSI	Deutsches SOFIA Institut	page 2
EFDD	Enhanced Frequency Domain Decomposition	page 14
EMA	Experimental Modal Analysis	page 9
FBC	Flexible Body Compensation	page 76
FCU	File Conversion Utility	page 65
FDC	Fast Diagnostic Camera	page 70
FDD	Frequency Domain Decomposition	page 11
FEM	Finite Element Method	page 50
FPI	Focal Plane Imager	page 5
FRF	Frequency Response Function	page 11
IRF	Impulse Response Function	page 11
MAC	Modal Assurance Criterion	page 14
MATLAB	Matrix Laboratory, a computational mathematics software	page 64
MST	SOFIA Modal Survey Test, conducted in March 2008	page 6
NASA	National Aeronautics and Space Administration	page 2
OMA	Operational Modal Analysis	page 9
PDF	Probability Density Function	page 20
PSD	Power Spectral Density	page 11
QUAD4	Four node shell element in the FEM software Nastran	page 50

RMS	Root Mean Square	page 5
SDOF	Single Degree of Freedom	page 15
SOFIA	Stratospheric Observatory For Infrared Astronomy	page 1
SSI	Stochastic Subspace Identification	page 11
SVD	Singular Value Decomposition	page 13
SVS	Structural Vibration Solutions A/S	page 37
TA	Telescope Assembly	page 2
TARF	Telescope Assembly Reference Frame	page 64
UFF	Universal File Format	page 37
USRA	Universities Space Research Association	page 2

Symbols used in a generic sense

Greek Symbols

γ	Kurtosis	page 32
γ_k	Modal participation vector	page 12
μ	Mean, or expected value, of a stochastic variable	page 32
ϕ_k	Mode shape vector	page 12
σ	Standard deviation of a stochastic variable	page 32
σ^2	Variance of a stochastic variable	page 32
τ	Time lag	page 11
ω	Circular frequency	page 11
ζ	Damping ratio	page 31

Roman Symbols

C_{kl}	Correlation coefficient	page 34
$\mathbf{D}$	Damping matrix	page 11
f	Frequency	page 17
$f(x)$	Probability density function (PDF)	page 32
$\mathbf{I}$	Identity matrix	page 29
j	Imaginary unit $\left(j^2 = -1\right)$	page 11
$\mathbf{K}$	Stiffness matrix	page 11
$\mathbf{M}$	Mass matrix	page 11
m	Number of measurement channels	page 12

M_k	Modal mass	page 14
n	Number of modes	page 12
n^*	Number of dominant modes	page 13
$\mathbb{R}$	Real numbers	page 22
r	Number of excitation inputs	page 12
T	Sampling interval	page 31
t	Time, continuous or discrete	page 11
$\mathbf{U}_1, \mathbf{S}_1, \mathbf{V}_1$	Non-zero part of Decomposition matrices of SVD	page 29
W_k	Correlation evaluation value of projection channel	page 34

Symbols used in Frequency Domain Decomposition

Greek Symbols

λ_k	Complex pole	page 12
Ω_1	Modal Coherence Indicator threshold	page 18
Ω_2	Modal Domain Indicator threshold	page 19

Roman Symbols

A_i, B_i	Curve-fitting parameters	page 17
d_1	Modal Coherence Indicator	page 18
d_2	Modal Domain Indicator	page 19
d_k	Scalar constant denoting a mode's contribution to overall vibration	page 13
f_0	Reference frequency	page 18
$\mathbf{g}(t)$	Impulse response function	page 11
$\mathbf{G}_{xx}$	PSD matrix of inputs	page 12
$\mathbf{G}_{yy}$	PSD matrix of measurements	page 12
G_{kk}	Auto-PSD of the k^{th} measurement channel	page 12
G_{kl}	Cross-spectral density of the k^{th} measurement channel with the l^{th} measurement channel	page 12
$\mathbf{H}(j\omega)$	Matrix of Frequency Response Functions	page 11
R_k	Residue in partial notation	page 12
$\mathbf{S}_i$	Diagonal matrix of singular values of PSD matrix at frequency ω_i	page 13
s_{ij}	j^{th} singular value of PSD matrix at frequency ω_i	page 13
$\mathbf{U}_i$, $\mathbf{V}_i$	Matrices of left and right singular vectors $\mathbf{u}_{ij}$, $\mathbf{v}_{ij}$	page 13
$\mathbf{u}_{ij}$, $\mathbf{v}_{ij}$	j^{th} left and right singular vectors of PSD matrix at frequency ω_i	page 13
$\mathbf{X}(j\omega)$	Fourier Transform of excitation input	page 11
$\mathbf{x}(t)$	Vector of excitation input	page 11
$\mathbf{Y}(j\omega)$	Fourier Transform of measurement channels	page 11
$\mathbf{y}(t)$	Vector of measurement channels, output	page 11

Symbols used in Stochastic Subspace Identification

Greek Symbols

Γ	Observability matrix	page 26
Γ_i	Extended observability matrix	page 26
Δ_i	Extended controllability matrix	page 25
Λ_i	Output covariance matrix	page 24
ρ_w, ρ_v	Regression residuals	page 21
θ_i	Principal angle	page 23

Roman Symbols

$\mathbf{A}_c$	System matrix (continuous time)	page 20
$\mathbf{A}_d$	System matrix (discrete time)	page 21
$\mathbf{B}$	Input System matrix	page 20
$\mathbf{C}$	Observation matrix	page 20
$\mathcal{C}$	Controllability matrix	page 25
$\mathbf{e}_t$	Innovation process	page 22
$\mathbf{f}(t)$	System input	page 20
i	Number of block rows in the upper and lower halves of the block Hankel matrix	page 26
j	Number of columns in the block Hankel matrix	page 26
$\mathbf{K_t}$	Non-steady state Kalman gain	page 22
$\mathbf{L}_i$	Block Toeplitz matrix of output covariances	page 27
n	State space dimension	page 21
$\mathcal{O}_i$	Common SSI Input matrix	page 28
$\mathbf{G}$	Covariance matrix between output and system states at next time step	page 24
$\mathbf{P}$	State covariance matrix	page 24
$\mathbf{Q}$, $\mathbf{S}$, $\mathbf{R}$	Covariance matrices of process and measurement noise	page 24
$\mathbf{T}$	Arbitrary similarity transformation matrix	page 29
$\mathbf{v}(t)$, $\mathbf{v}_t$	Measurement noise	page 21
$\mathbf{w}(t)$, $\mathbf{w}_t$	Process noise	page 21
$\mathbf{W}_1$, $\mathbf{W}_2$	Weight matrices	page 29
$\hat{\mathbf{X}}_i$	Sequence of Kalman filter state estimates	page 27
$\hat{\mathbf{x}}_t$	Estimated system state	page 21
$\mathbf{x}(t)$, $\mathbf{x}_t$	System states, continuous and discrete	page 20

$\mathbf{Y}$	Matrix of measurement samples	page 26
$\mathbf{y}(t)$	Measurement channels, System output (continuous time)	page 20
$\mathbf{Y}_h$	Block Hankel matrix of measurement samples	page 26
$\mathbf{Y}_{hf}$	The “future”: Lower half of the block Hankel matrix	page 26
$\mathbf{Y}_{hp}$	The “past”: Upper half of the block Hankel matrix	page 26

Mathematical Operators

$\mathbf{A}/\mathbf{B}$	Orthogonal projection of **A** onto the row space of **B**	page 22
$\mathbf{a} \perp \mathbf{b}$	Vector **a** is orthogonal to **b**	page 23
$\mathbf{A}^+$	Moore-Penrose pseudo-inverse of **A**	page 22
$\overline{A}$	Complex conjugate of A	page 12
A^T	Transpose of A	page 12
$a * b$	Convolution of a and b	page 11
δ_{kl}	Kronecker delta	page 24
$\mathrm{E}[x]$	Expected value of x	page 23
$\mathrm{E}[x\|y]$	Expected value of x given y, conditional mean	page 23
$\dot{\mathbf{y}}(t)$	Time derivative of **y**, e.g., velocity	page 20

1 Introduction

1.1 The Stratospheric Observatory For Infrared Astronomy

Figure 1.1: SOFIA during its first flight with fully opened door, December 2009. © NASA Dryden

For more than 400 years, people have used telescopes to look into the stars. Starting with Galileo Galilei, who discovered the Galilean moons of Jupiter by directing his telescope at the sky, the technological advancement of optical instruments enabled astronomers to gain increasing knowledge about our universe. The *Stratospheric Observatory For Infrared Astronomy (SOFIA)* is another step in the series of such technological development.

SOFIA is an airborne observatory that will fly in the stratosphere at an altitude of 12,000 m and above. The observatory consists of a Boeing 747SP aircraft – shown in Figure 1.1 – equipped with a 2.5 m telescope, which is completely integrated into the rear part of the fuselage. With this setting, it is possible to observe objects and areas in the sky that emit radiation in the infrared and sub-millimeter spectrum. Radiation from outer space, which lies within the wavelengths of the infrared and sub-millimeter spectrum, cannot be detected by ground-based observatories, because the earth's atmosphere – mainly due to water vapor – absorbs most of the light in that spectral range – see for instance Figure 1.2. Objects which are interesting for observing or can only be detected in the infrared spectrum include [6]:

- Clouds of dust and gas, which glow in the infrared due to their relatively low temperature, e.g., the area around the Orion constellation as shown in Figure 1.3.
- Objects such as stars or the center of our galaxy, which are embedded into dense regions of molecular clouds of gas and dust, where visible light cannot pass through.
- Distant galaxies with a high redshift

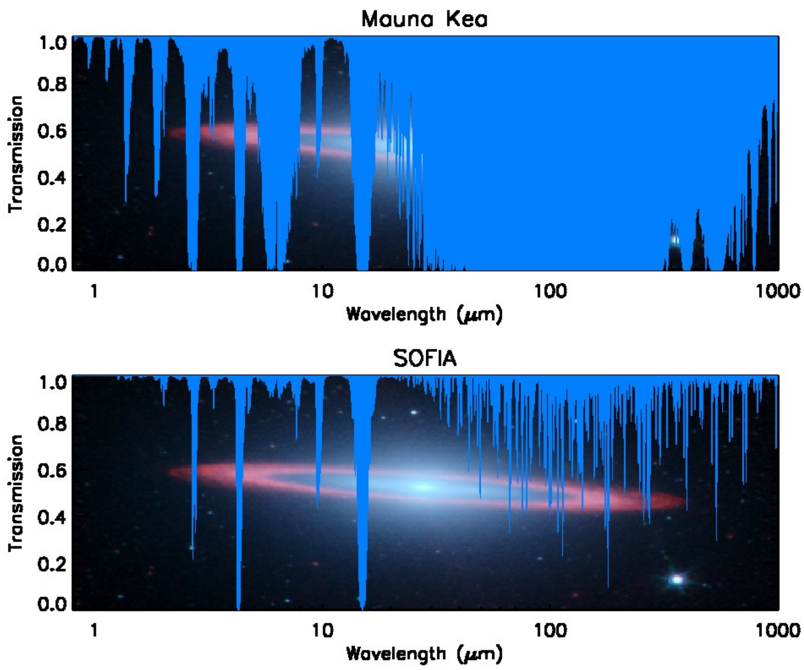

Figure 1.2: Typical atmospheric transmission of infrared and sub-millimeter light for SOFIA at an altitude of 45,000 ft (13.7 km) compared to the transmission on a good night at Mauna Kea, Hawaii (13,800 ft). While the spectral range from 30 to 300 μm is completely blocked for the ground based telescope at Mauna Kea, SOFIA's reception of this band is much better. © USRA/NASA

- Exoplanets

The SOFIA project is a joint program by the United States' *National Aeronautics and Space Administration (NASA)* and the German Aerospace Center *Deutsches Zentrum für Luft- und Raumfahrt (DLR)*. While aircraft systems and flight operations are managed by the *NASA Dryden Flight Research Center (DFRC)*, the German built SOFIA Telescope Assembly (TA) is developed and optimized by the *Deutsches SOFIA Institut (DSI)*. The SOFIA aircraft is based at the *NASA Dryden Aircraft Operations Facility (DAOF)* in Palmdale, California.

Another major stakeholder in the SOFIA project is the *Universities Space Research Association (USRA)*, which built up and manages the *SOFIA Science Center (SSC)*, located at NASA Ames Reseach Center in Moffett Field, California. The SSC is responsible for the science productivity of the mission. USRA and DSI both have a part in science operation and mission planning, providing the science platform to various science teams throughout the year, selected from peer-reviewed proposals within the science programs of NASA and the DLR.

A schematic view of the SOFIA Observatory is shown in Figure 1.4. The TA resides in the rear part of the fuselage with the main part in an open cavity environment. The telescope views the sky through a port-side doorway, which can be opened during flight at high altitudes. It is actuated by magnetic torquers around a spherical bearing, which resides in a pressure bulkhead – shown as a green disc in Figure 1.5. This configuration enables an unimpaired view of the telescope optics from the open cavity into the sky. The science instrument is mounted to the TA on the cabin side of the pressure bulkhead inside the pressurized cabin and can easily be accessed by scientists and engineers.

The SOFIA telescope is a Cassegrain design with a Nasmyth focus. The primary mirror has a diameter of 2.7 m and is made of a light weighted Zerodur structure. The effective optical aperture is 2.5 m. The parabolic shape of the primary mirror directs the incoming light onto the hyperbolic secondary mirror, which in turn deflects the optical beam to the tertiary mirror tower. A dichroic tertiary mirror reflects the infrared light through the Nasmyth

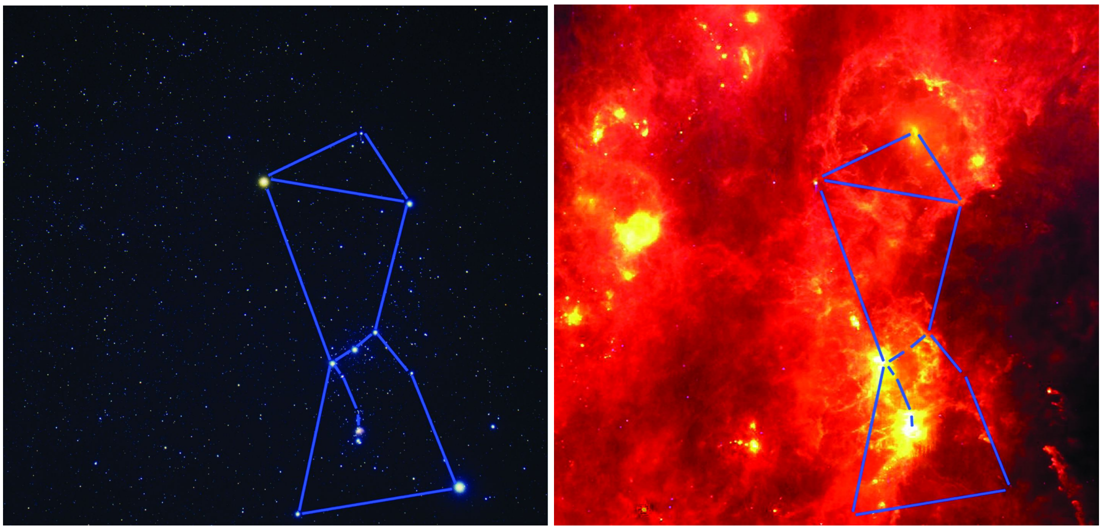

(a) Visible light spectrum © Akitu, Fujii (b) Infrared spectrum © IRAS

Figure 1.3: The Orion constellation as seen in visible light and in the infrared. Stellar emission dominates the image to the left, taken in the visible spectrum. The image to the right shows the same portion of the sky taken by the Infrared Astronomical Satellite IRAS. A large region of interstellar dust emits light visible in the infrared spectrum. Stellar emission vanishes almost entirely.

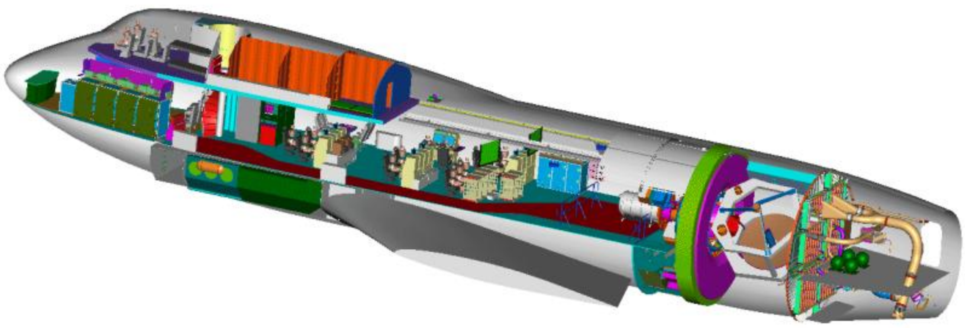

Figure 1.4: A cutaway view of SOFIA. The telescope structure with its mirrors and the metering structure can be seen on the right side of the image, just behind the trailing edge of the wing. In the middle section, there are controlling consoles for the scientist and engineers. Most computer racks and other technical equipment are located in the front, on the main deck below the cockpit. © NASA

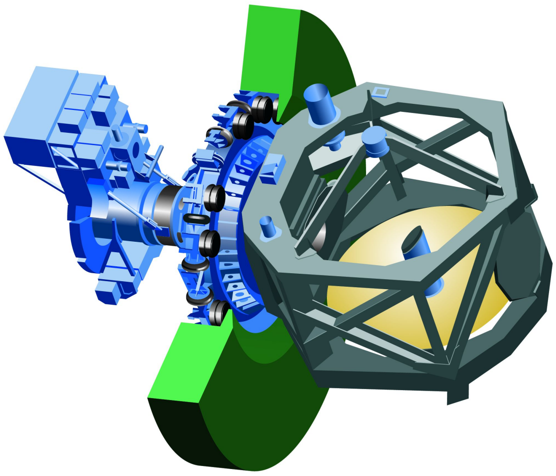

Figure 1.5: CAD drawing of the SOFIA Telescope Assembly. The green disc represents the pressure bulkhead, where the Telescope Assembly is mounted by a hydrostatic bearing. The mirrors and metering structure on the right side are located in the open cavity, whereas the science instrument (not shown) is mounted at the flange on the cabin side to the left of the image. © DSI

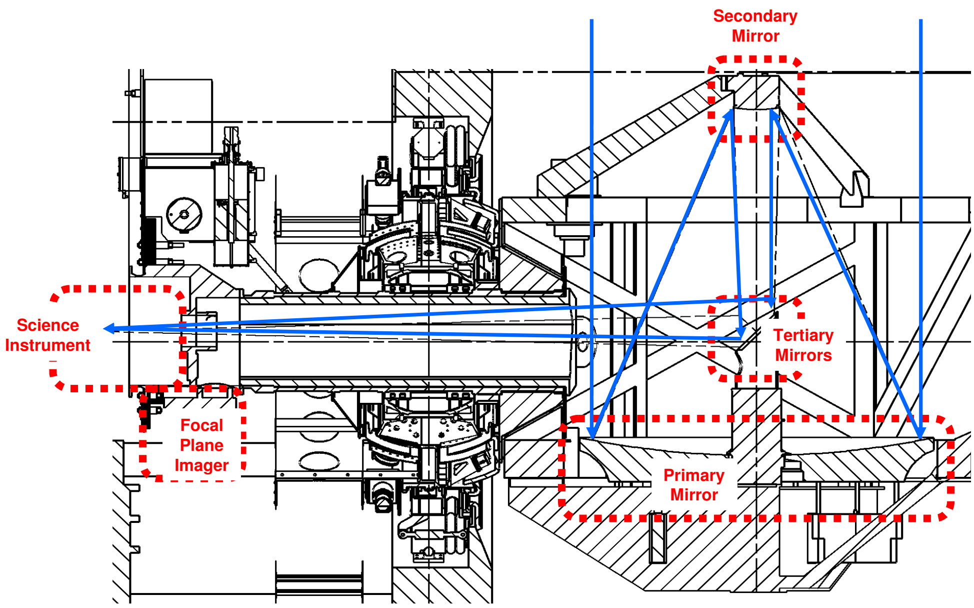

Figure 1.6: The optical path of the SOFIA telescope, designed as a Cassegrain configuration with a Nasmyth focus. See text for details. © MAN Technologie

Table 1.1: Error sources and limitations affecting pointing stability and image quality (Source: [17])

Pointing stability	Image quality
• Vibrations of telescope structure (under 70 Hz) – induced by aircraft vibrations – induced by aero-acoustic vibrations • Random drift of gyroscopes and its estimation process • Centroid error and contributions from tracking system	• Diffraction • Imperfection of manufactured optical elements • Optical abberations – due to gravity – due to slow temperature and pressure variations in flight • Seeing – due to shear layer – atmospheric • Vibrations of telescope structure (above 70 Hz)

tube into the focus, where the science instrument is located. The visible portion of the light beam passes through the dichroic tertiary and is reflected by an additional flat tertiary mirror, also through the Nasmyth tube, into a guiding camera, the Focal Plane Imager (FPI). For an illustration of the optical path, see Figure 1.6.

1.2 Pointing Stability and Image Quality

One of the major challenges in an airborne environment for an observatory are *pointing stability* and *image quality*. Pointing stability is defined as the measure of relative motion of a science object of interest in the focal plane of the telescope [17]. The technical goal of the SOFIA project is to reach a pointing stability of 1.0 arcsec root mean square (RMS) at the first scientific flights and 0.2 arcsec (RMS) in the long-term operational phase. The image quality requirement for SOFIA is expressed in terms of the diameter of a circle enclosing 80% of the energy from a stellar image at a wavelength of 0.633 μm at the infrared focus. The image quality budget allows a diameter of 1.5 arcsec according to that definition [17].

Table 1.1 lists error and disturbance sources which have influence on these variables. One of these disturbance sources, which appears on both measures, is vibration of the telescope structure. The vibration includes rigid and flexible body motion. Rigid body motion is the motion of the telescope assembly around its mounting suspension while it is assumed that the telescope structure would be indefinitely stiff. The magnitude of the pointing stability error due to rigid body motion is mainly dependent on the the implementation of the pointing control system. In addition to the rigid body motion, the telescope structure is also subject to flexible vibration, which contributes to the image quality budget as well. The specified distinction that structural vibrations below 70 Hz affect the pointing stability budget, whereas vibrations above 70 Hz affect the image quality budget, is due to the technical specification and was set with the reason in mind that most science instruments are not able to resolve the image with higher bandwidths [20].

1.3 Modal Analysis

From an engineering point of view, it is desirable to be able to characterize the flexible body motion in order to develop pointing control and image quality improvement strategies. For this purpose, an integrated end-to-end simulation model was developed, which includes:

- Geometrical and structural information manifested in a finite element model
- A model of the cavity disturbance environment
- A model of the pointing control system

Such a model needs constant updating and verification. With every design modification and new test results, the information incorporated into the model is updated. Generally, the model becomes more and more accurate during the design process.

One way of characterizing the dynamical behavior of a system is to describe it by its normal modes [8]. As long as the design of the system ensures linearity, every motion of a system can be described as a weighted superposition of fundamental normal modes, which are an inherent property of the structure. The excitation of the system determines, which mode contributes how much to the overall motion. The first step to obtain information about the normal modes is an analytical modal analysis performed with the finite element model (*FE model*). This yields a so called modal model, which contains[1]

- the natural frequencies of the modes.
- the deflection of the structure corresponding to the natural frequencies, called the mode shapes.

The analytical model is later validated experimentally and the results from such experimental modal analyses serve as basis for updating the analytical model. Such a experimental modal analysis has been performed with the SOFIA Observatory in the so called Modal Survey Test (MST) in March 2008 [3]. During that test campaign, the TA was equipped with several hundred accelerometers and the structure was excited by electrodynamic shakers at well defined locations. These exciters were driven by random signals with defined spectral properties and their excitation location was chosen in order to reach all significant target modes, which means that all the important modes were excited enough so that the structure really vibrated in these modes and they could be recognized from the measurement data. The MST provided detailed information about the dynamic behavior of the TA and is of great benefit for the engineering process.

On the other hand, the environment during the MST did not reflect the environment during operational flights. While the MST yielded information about the TA under free vibration, due to the nature of the method, the structure will be constantly excited into forced vibration during operational conditions. The TA will be mainly excited by aerodynamic and acoustic loads originating in the air flow and turbulences around the aircraft and the open cavity door. This kind of excitation is not measurable to the full extend and it has a large non-deterministic component. Also, when the door is open at high altitudes, temperatures of the cavity and the telescope structure will be at around -30 °C to -40 °C. This has significant effects on the material properties of the structure, also affecting the modal behavior.

Thus, the difference in the dynamic environment demands an additional, or new, approach to obtain a modal model, which covers these conditions. This is where *Operational Modal Analysis (OMA)* comes at hand. OMA depends on the stochastic nature of the excitation input and is conducted directly during operation conditions, without specific need to measure the excitation. It is thus desirable to have an expertise about OMA within the SOFIA project and be able to employ it in order to improve the performance of the observatory.

[1] The third parameter in a modal model, the damping ratio of a mode, can usually not be obtained by analytical methods such as FEM

1.4 Thesis Objectives and Outline

The purpose of this study thesis is to characterize the methods of Operational Modal Analysis and to show how it is applied during the SOFIA optimization process now and in the near future. This will aid in maintaining and updating the modal and integrated end-to-end models of the TA structure, and thus hopefully serve as valuable input for the development and improvement of the SOFIA Telescope Pointing Control System as well as other measures to control the flexible body motion. In the long term, this hopefully will also improve the image quality and thus the science performance of SOFIA.

First, the mathematical theory behind OMA is outlined in Chapter 2. The chapter deals briefly with the differences between the classical experimental modal analysis approach – such as conducted in the MST – and the OMA approach. It introduces the theory of two major methods used in OMA: *Frequency Domain Decomposition* (Section 2.2) and *Stochastic Subspace Identification* (Section 2.3). Additionally, some theoretical aspects about detecting harmonic components in the input signal are discussed in Section 2.4; and Section 2.5 introduces a method of selecting only certain measurement channels in order to reduce computational load.

Chapter 3 briefly introduces the software *ARTeMIS Extractor* along with its helper application *ARTeMIS Testor*, both written by *Structural Vibration Solution A/S*, which are employed by the DSI to conduct the operational modal analyses.

In order to familiarize with the software as well as to have a better insight into the algorithms used, a preliminary experiment with a simple aluminium plate equipped with a few accelerometers has been conducted. Motivation, set-up, procedure and results of this experiment are discussed in Chapter 4. Appendix A contains the experimental data.

During preparation for this study thesis and early stages, the initial plan was to familiarize quickly with the OMA method and then focus on extensive analysis of flight test data, which was projected to be available during the author's stay at the DAOF in the summer of 2009. Unfortunately, repeated delays in the SOFIA program schedule caused this effort to slip beyond the time frame of this thesis. This is why Chapter 5 deals with SOFIA instrumentation data in a limited way and the main focus has shifted to Chapter 2. Nevertheless, major effort has been spent to develop and evaluate data conversion and processing tools in order to be able to start data analysis fast as soon as operational data is available. These tools have been developed and employed with data, which was obtained during preparatory pre-flight tests such as the Line Operations of September 2009. Although the quality of this data was not satisfactory enough to be able to extract a modal model by the methods of OMA, it served well as input for the development process of the conversion and processing tools. Chapter 5 discusses these tools as well as the process of obtaining instrumentation data and some results and lessons learned during the process.

By the expertise of this study thesis, the DSI should be able to employ the methods of OMA during future test flight campaigns in a reasonable fast way and with a good confidence on the integrity of obtained model information. Besides summarizing the work done, Chapter 6 tries to give an outlook for possible future developments that need or could be incorporated into the development process of the SOFIA observatory with respect to OMA and the improvement of pointing stability and image quality.

2 Theory of Operational Modal Analysis Techniques

2.1 Motivation for Operational Modal Analysis

Every mechanical structure, called a "system", is subject to flexible movement and vibration. Since all such movement – linear behavior assumed – can be expressed as a combination of fundamental modal movement, it is desirable to characterize the dynamic behavior of a structure by a *modal model*. Such a model consists of

- the resonance or natural frequencies of a structure,
- the corresponding mode shapes, and
- their modal damping.

To determine those parameters from an experimental point of view, *Experimental Modal Analysis (EMA)* has been an established method since decades [2]. In EMA, the structure is excited by a controlled and measured signal at defined locations on the structure and the dynamic response is measured by well placed sensors, e.g. accelerometers. Excitation is usually applied by shakers, impulse hammers or eccentric rotation masses.

A comparison between excitation signal and measured response yields a set of estimated *Frequency Response Functions (FRF)*, which show peaks at resonance frequencies and from which a modal model can be derived.

EMA usually requires a lab environment where it is possible to apply deterministic excitation. However, during the structure's actual operation the dynamic environment can be significantly different. Especially excitations can have various different sources such as aerodynamic loading and engine vibration, all at the same time. These excitations are difficult if not impossible to measure during operation – think of SOFIA during flight conditions.

This is where *Operational Modal Analysis (OMA)* has its application field. The objective of OMA, also known as Output-Only Modal Analysis, is to derive a modal model of the system by using only the measured response and without explicitly knowing the excitation input. Figure 2.2 illustrates the difference of the system scheme compared to the system scheme for EMA as shown in Figure 2.1. The unknown loads created by the operational environment are assumed to be produced by a virtual system loaded by white noise. The white noise is not assumed to drive the structural system but the total system consisting of the real structural system and the virtual loading system. Thus, the identification process of OMA does not yield a model of the structure alone, but the operational environment is also part of the identified system. Since it is of major interest how a structural system's behavior is during operational conditions, this fact is not necessarily a disadvantage. However, it must be kept in mind, when comparing results of an OMA to modal models obtained by EMA or other approaches such as analytical or Finite Element Methods (FEM).

The method of OMA has been introduced some 10 years ago and commercial software has been being available for a few years. There are several methods being used and under research in state-of-the-art OMA [16], including:

- Frequency Domain Decomposition (FDD)
- Stochastic Subspace Identification (SSI)

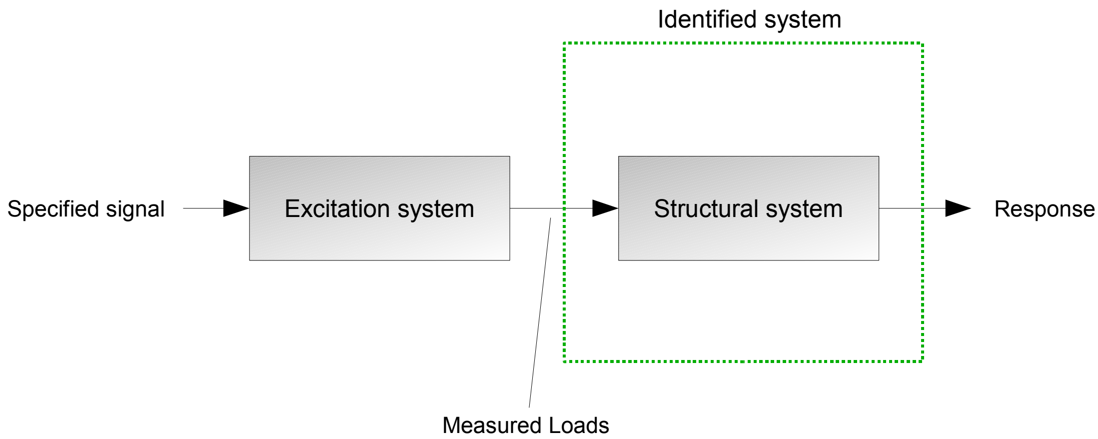

Figure 2.1: System scheme for the classical Experimental Modal Analysis approach. A comparison between the measured loads and the system response yields a direct identification of the structural system.

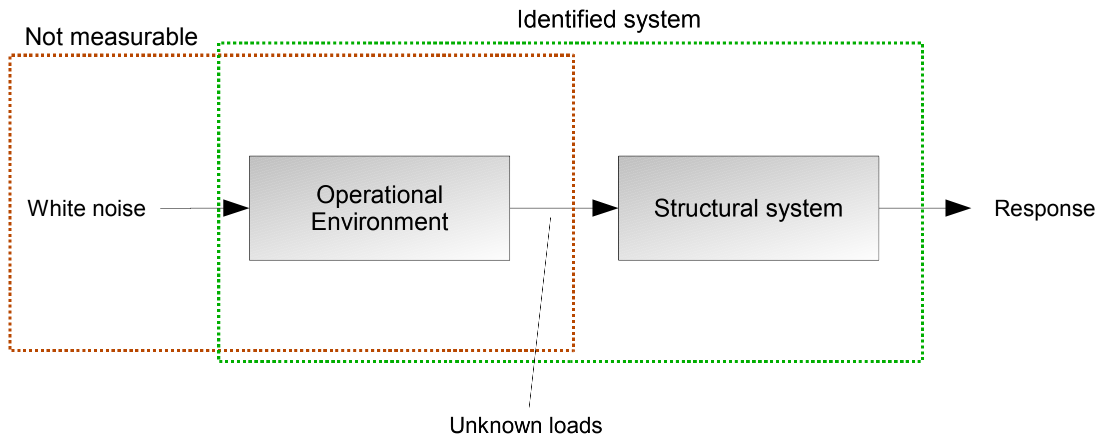

Figure 2.2: System scheme for Operational Modal Analysis. Since the exact influence of the operational environment onto the structural system cannot be measured, OMA assumes white noise as input and identifies a system which includes the structural system and the environment.

- Frequency Domain Subspace
- Natural Excitation Techniques (NExT)
- Operational PolyMAX

The work of this study thesis concentrates on FDD and SSI as these two methods are implemented in the software *ARTeMIS Extractor* by *Structural Vibration Solutions A/S* which is used by the DSI to identify modal parameters of the SOFIA Telescope Assembly. After introducing the theory of those OMA methods in the chapter at hand, a quick overview of that software is given in Chapter 3.

2.2 Frequency Domain Decomposition

2.2.1 Basic Frequency Domain Decomposition

Frequency Domain Decomposition (FDD) is a method very transparent to the user. It has been introduced by Brincker et al. [11] in 2000. FDD is an improvement to the classical approach in EMA to pick resonance peaks from frequency response plots.

The basis of modal analysis from an experimental point of view is the so called system equation

$$\mathbf{y}(t) = \mathbf{g}(t) * \mathbf{x}(t), \tag{2.1}$$

which is here denoted in time domain. It connects the excitation input $\mathbf{x}(t)$ to the measured system response $\mathbf{y}(t)$ via the Impulse Response Function (IRF) $\mathbf{g}(t)$ of the system using convolution:

$$[\mathbf{g} * \mathbf{x}]\,(t) = \int_{-\infty}^{\infty} \mathbf{g}(\tau)\mathbf{x}(t-\tau)\,d\tau \tag{2.2}$$

τ is the time variable integrated from $-\infty$ to ∞. Convolution can be interpreted as the amount of overlap two functions have as they are shifted over each other. In the case of multi-dimensional inputs and outputs, $\mathbf{g}(t)$ is a matrix of IRFs.

The system equation (2.1) is another way of describing the classical equation of motion in dynamical analysis (or rather the particular solution of it):

$$\mathbf{M}\ddot{\mathbf{y}}(t) + \mathbf{D}\dot{\mathbf{y}}(t) + \mathbf{K}\mathbf{y}(t) = \mathbf{x}(t) \tag{2.3}$$

with the system's mass matrix $\mathbf{M}$, damping matrix $\mathbf{D}$ and stiffness matrix $\mathbf{K}$.

By Fourier transform [30], equation (2.1) becomes

$$\mathbf{Y}(j\omega) = \mathbf{H}(j\omega)\mathbf{X}(j\omega) \tag{2.4}$$

in frequency domain, where $\mathbf{H}(j\omega)$ contains the set of Frequency Response Functions (FRFs) of the system. In EMA, where both input $\mathbf{X}(j\omega)$ and output $\mathbf{Y}(j\omega)$ are known, the FRFs can directly be calculated and used for model extraction. Since $\mathbf{X}(j\omega)$ is not known in OMA, though, further mathematics and assumptions are needed.

Equation (2.4) can be enhanced onto power spectral densities (PSD) [30]. In the case of auto-spectral density, the PSD function can be visualized as how the power of a single signal Y_k is distributed within the frequency spectrum. The Integral of the PSD over a certain frequency range denotes the energy contained in the signal at that frequency range. The PSD can be calculated directly from the Fourier transform:

$$G_{kk}(j\omega) = \overline{Y}_k(j\omega) \cdot Y_k(j\omega) = |Y_k(j\omega)|^2 \tag{2.5}$$

Here, the bar over $\overline{Y}_k$ denotes the complex conjugate of a variable.

Using not a single but two different signal channels Y_k and Y_l, the cross-spectral density can be calculated in the same way:

$$G_{kl}(j\omega) = \overline{Y}_k(j\omega) \cdot Y_l(j\omega) \tag{2.6}$$

Arranging auto-spectral densities and cross-spectral densities in a matrix yields a so called power spectral density matrix or PSD matrix. This can be done for both input and output channels:

$$\mathbf{G}_{xx}(j\omega) = \begin{bmatrix} \overline{X}_1(j\omega)X_1(j\omega) & \overline{X}_1(j\omega)X_2(j\omega) & \dots & \overline{X}_1(j\omega)X_r(j\omega) \\ \overline{X}_2(j\omega)X_1(j\omega) & \overline{X}_2(j\omega)X_2(j\omega) & \dots & \overline{X}_2(j\omega)X_r(j\omega) \\ \vdots & \vdots & \ddots & \vdots \\ \overline{X}_r(j\omega)X_1(j\omega) & \overline{X}_r(j\omega)X_2(j\omega) & \dots & \overline{X}_r(j\omega)X_r(j\omega) \end{bmatrix} = \overline{\mathbf{X}}\mathbf{X}^T \tag{2.7}$$

$$\mathbf{G}_{yy}(j\omega) = \begin{bmatrix} \overline{Y}_1(j\omega)Y_1(j\omega) & \overline{Y}_1(j\omega)Y_2(j\omega) & \dots & \overline{Y}_1(j\omega)Y_m(j\omega) \\ \overline{Y}_2(j\omega)Y_1(j\omega) & \overline{Y}_2(j\omega)Y_2(j\omega) & \dots & \overline{Y}_2(j\omega)Y_m(j\omega) \\ \vdots & \vdots & \ddots & \vdots \\ \overline{Y}_m(j\omega)Y_1(j\omega) & \overline{Y}_m(j\omega)Y_2(j\omega) & \dots & \overline{Y}_m(j\omega)Y_m(j\omega) \end{bmatrix} = \overline{\mathbf{Y}}\mathbf{Y}^T \tag{2.8}$$

where $\mathbf{G}_{xx}(j\omega)$ is the $r \times r$ PSD matrix of inputs (unknown in OMA) and $\mathbf{G}_{yy}(j\omega)$ is the PSD matrix of measured response channels, while the number of measured channels is m and thus the size of $\mathbf{G}_{yy}$ is $m \times m$.

By simple mathematical manipulations using (2.4), it can then be shown that $\mathbf{H}(j\omega)$ relates the Power Spectral Density (PSD) matrices of input and output signals:

$$\mathbf{G}_{yy} = \overline{\mathbf{H}}\mathbf{G}_{xx}\mathbf{H}^T \tag{2.9}$$

The FRF can be denoted in partial fraction

$$H(j\omega) = \sum_{k=1}^{n} \left(\frac{R_k}{j\omega - \lambda_k} + \frac{\overline{R}_k}{j\omega - \overline{\lambda}_k} \right) \tag{2.10}$$

with the number of modes n. λ_k is the pole consisting of resonance frequency and damping value, and R_k is the residue consisting of mode shape vector ϕ_k and modal participation vector γ_k.

$$R_k = \phi_k \gamma_k^T \tag{2.11}$$

The presence of the second summand in (2.10) indicates that the poles λ_k, $\overline{\lambda}_k$ and corresponding residues R_k, $\overline{R}_k$ always appear in pairs.

After some mathematical manipulations (see [11]) and the assumptions of

- spatial and frequential white noise as input
- and the presence of light damping,

the PSD matrix of the measured response channels can be expressed as

$$\mathbf{G}_{yy}(j\omega) = \sum_{k=1}^{n^*} \left(\frac{d_k \phi_k \phi_k^T}{j\omega - \lambda_k} + \frac{\overline{d}_k \overline{\phi}_k \overline{\phi}_k^T}{j\omega - \overline{\lambda}_k} \right) \tag{2.12}$$

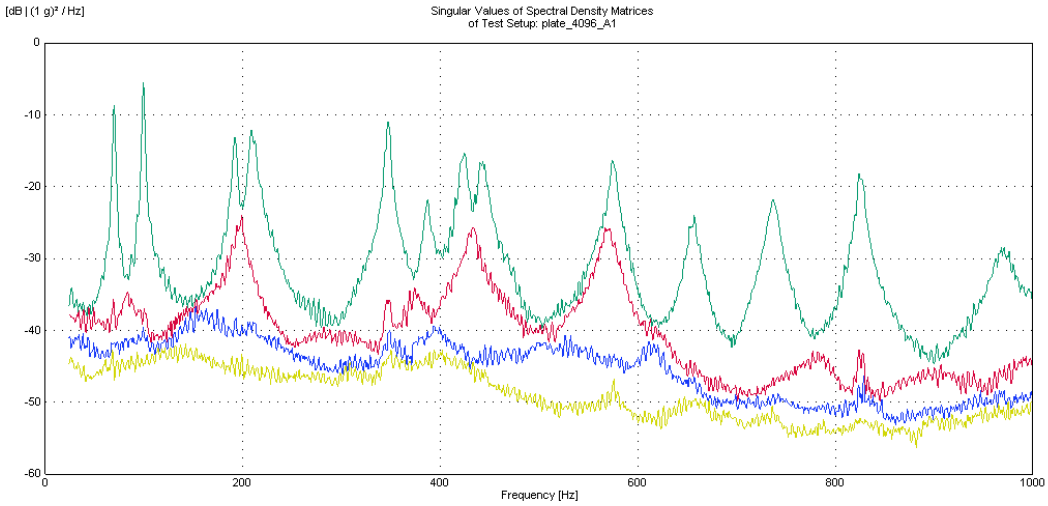

Figure 2.3: Plot of first four singular values for a test setup with 12 measurement channels. Just those few singular value curves are sufficient to identify structural modes by their peaks on the first and second singular value. Since the Singular Value Decomposition (SVD) algorithm orders the singular values, the lines do never cross each other. Instead, the representation of the influence of one mode jumps from the first singular value (green) to the second one (red) as soon as another mode dominates the frequency band. The contact of the red with the green curve at 200 Hz is an example for that.

where n^* denotes that only dominant modes at a certain frequency ω are relevant. d_k is a scalar constant depending on the modal participation factor and the unknown volume of the input noise. Since mode shapes in a modal model are generally unscaled, d_k is not of further interest in pure OMA.

With equation (2.12), a direct link between the measurement data $\mathbf{G}_{yy}$ and the modal parameters ϕ_k and λ_k is established. ϕ_k is the mode shape vector and λ_k is a complex value, which contains the natural frequency and the damping ratio. The next step is to extract these modal parameters from the measurement data.

In classical peak-picking methods for EMA and early OMA, resonance peaks are picked from the PSD Plots, where $j\omega - \lambda_k$ has a minimum. However, $\mathbf{G}_{yy}$ has a size of $m \times m$, where m is the number of measurement channels. Thus inspecting m^2 PSD plots for peaks can be tedious and is prone to errors, especially when there are close modes to detect.

This is why Brincker et al. introduced the use of a *Singular Value Decomposition* (SVD) of the PSD matrix:

$$\mathbf{G}_{yy}(j\omega_i) = [\mathbf{u}_{i1}\ \mathbf{u}_{i2}\ \dots\ \mathbf{u}_{im}] \begin{bmatrix} s_{i1} & & & \\ & s_{i2} & & \\ & & \ddots & \\ & & & s_{im} \end{bmatrix} \begin{bmatrix} \overline{\mathbf{v}}_{i1}^T \\ \overline{\mathbf{v}}_{i2}^T \\ \vdots \\ \overline{\mathbf{v}}_{im}^T \end{bmatrix} \tag{2.13}$$

$$= \mathbf{U}_i \mathbf{S}_i \overline{\mathbf{V}}_i^T \tag{2.14}$$

decomposing the PSD matrix of the measured response into a set of singular vectors $\mathbf{U}_i = [\mathbf{u}_{i1}\ \mathbf{u}_{i2}\ \dots\ \mathbf{u}_{im}]$, $\mathbf{V}_i = [\mathbf{v}_{i1}\ \mathbf{v}_{i2}\ \dots\ \mathbf{v}_{im}]$, and corresponding scalar singular values s_{ij} forming the diagonal matrix $\mathbf{S}_i$. For a mathematical description of the SVD, see e.g. [13, page 70].

$\mathbf{U}_i$ and $\mathbf{V}_i$ are unitary matrices, which is the complex equivalent to an orthogonal matrix with real vectors [13, p. 73]. In this special case, $\mathbf{U}_i$ and $\mathbf{V}_i$ are identical, because $\mathbf{G}_{yy}$ is normal.

The singular values in $\mathbf{S}_i$ are in ordered position. This means that

$$s_{i1} > s_{i2} > \cdots > s_{im}$$

SVD can be performed with efficient numerical algorithms so that even for a large amount of discrete frequencies ω_i, processing measurement data only takes a few seconds.

In case of resonance, only one or a few close modes contribute to the motion. Thus, there is only one term in eq. (2.12), which means that there is only one singular value (since they are sorted, the first one) dominating in the SVD and the corresponding singular vector is an estimate of the mode shape for that resonance frequency ω_k. Therefore, the first singular vector is a good approximation of the mode shape vector for that frequency:

$$\hat{\phi}_k = \mathbf{u}_{k1} \tag{2.15}$$

In case of two contributing modes, two singular values dominate and so on. With this in mind, only one plot of the first four or five singular values over frequency is sufficient to detect resonance peaks. Such a plot is shown in Figure 2.3. This is a big advantage compared to inspecting m^2 PSD curves, which would be a total of 144 plots in the case of a test setup like in Figure 2.3.

The feature named “FDD” in ARTeMIS Extractor makes use of this method. It can only detect resonance frequencies and corresponding mode shapes. Modal damping can not directly be derived from this.

2.2.2 Enhanced FDD

ARTeMIS Extractor provides a second module named *Enhanced Frequency Domain Decomposition (EFDD)* which is an improvement of the method described above [18, Section 4.1].

It uses the singular vector selected by basic FDD and compares it to neighboring vectors by calculating the *Modal Assurance Criterion (MAC)* [1].

$$\mathrm{MAC} = \frac{\left|\hat{\phi}_1 \bar{\hat{\phi}}_2^T\right|^2}{\left|\hat{\phi}_1\right|^2 \left|\hat{\phi}_2\right|^2} \tag{2.16}$$

This criterion indicates how closely two vectors are related. With a value of 1, the two vectors are linearly dependent. With a value of 0, they are orthogonal. This is not to be confused with the property called orthogonality of modal vectors, indicating that they diagonalize mass and stiffness matrices:

$$\phi_i^T \mathbf{M} \phi_j = \begin{cases} 0 & i \neq j, \\ M_k & i = j \end{cases} \tag{2.17}$$

The latter formula is used for proper sensor placement in the selection of important modes, which are essential for the characterization and improvement of SOFIA image stability (see Section 5.2). The objective of that process was to place the sensors in a way that the targeted modes show a good orthogonality to each other, which means they are also distinguishable from each other.

For the peak selection in EFDD on the other hand, the objective is quite the opposite. By using the MAC value as a threshold (0.8 is considered to be a reasonable value), the algorithm finds a frequency band around the selected peak, where the singular vectors are very similar to each other and thus represent the same mode shape.

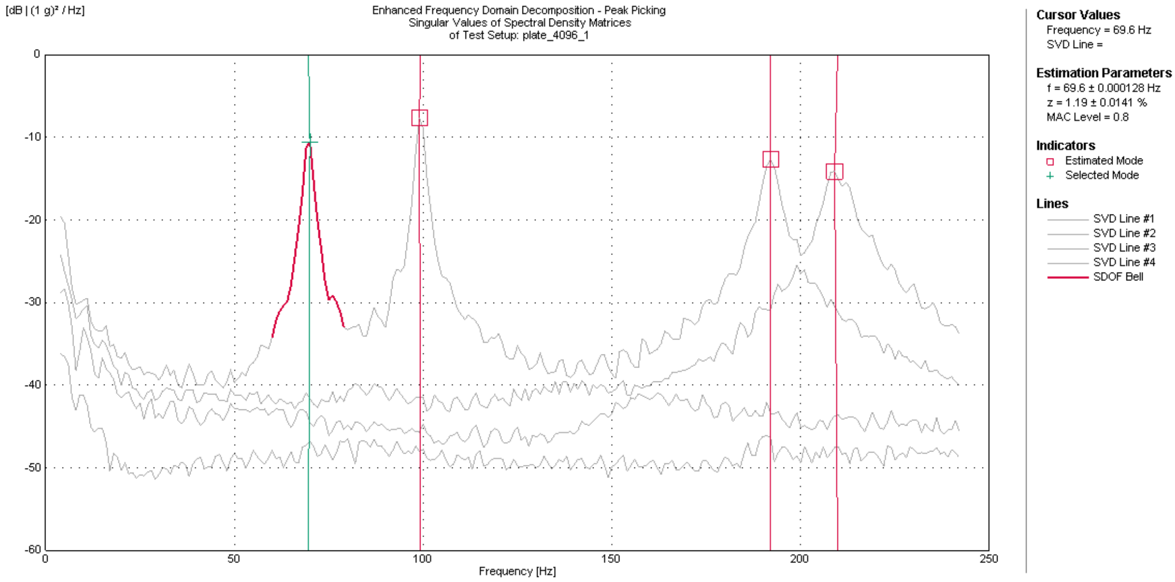

Figure 2.4: Frequency band of a selected peak for Enhanced Frequency Domain Decomposition (EFDD) mode estimation. The green line is the cursor, selecting the the leftmost peak on the singular value plot. The red highlighted line on the same peak represents the frequency range included as input for inverse Fourier transform. Three additional peaks are shown and marked by red rectangles. Those peaks have already been used for the estimation of modes, prior to the ongoing estimation of the leftmost peak.

This frequency band as shown in Figure 2.4 is used to average the singular vectors. Thus, not only one single calculation at a single frequency line determines the whole identification of modal parameters, but several lines contribute to it. Through that, the data is smoothed and less sensitive to noisy variations between frequency lines.

The averaging is performed using the singular value as weighting factor. Effectively it means, the closer a singular vector to the peak the more the vector contributes to the estimation of the mode shape.

Resonance frequency and damping ratio are estimated by performing a reverse Fourier transform of the selected frequency band. This so called correlation function can be considered as approximation of the spectral density function of a single-degree-of-freedom (SDOF) oscillator equivalent to the specific mode. Figure 2.5 illustrates the correlation function derived from the frequency band as selected in Figure 2.4, representing the free decay of an equivalent SDOF oscillator.

Plotting the extrema of the correlation function on a logarithmic scale such as in Figure 2.6, the curve should be a straight line in presence of viscous damping. Due to noise and non-linearities this is not true at the beginning and end of the correlation function. Because of that, a threshold for maximum and minimum correlation time is introduced. Inside that correlation time period, which is marked with a grey rectangle in Figure 2.5, a regression analysis is performed to the logarithmic extrema and the damping ratio is estimated by the logarithmic decrement.

Similarly, the natural frequency is estimated by a regression analysis on the straight line that counts the zero crossings as plotted in Figure 2.7. Because EFDD uses more than a single frequency line, the possible frequency resolution of estimated natural frequencies is higher than with the basic FDD. In the basic FDD method, one only selects the peak at a single frequency line and determines that frequency as the natural frequency. In EFDD, the determined frequency is influenced by several data points and the calculation yields a frequency value that can lie between the discrete frequency lines of the Fourier transform, thus increasing the resolution. Of course no

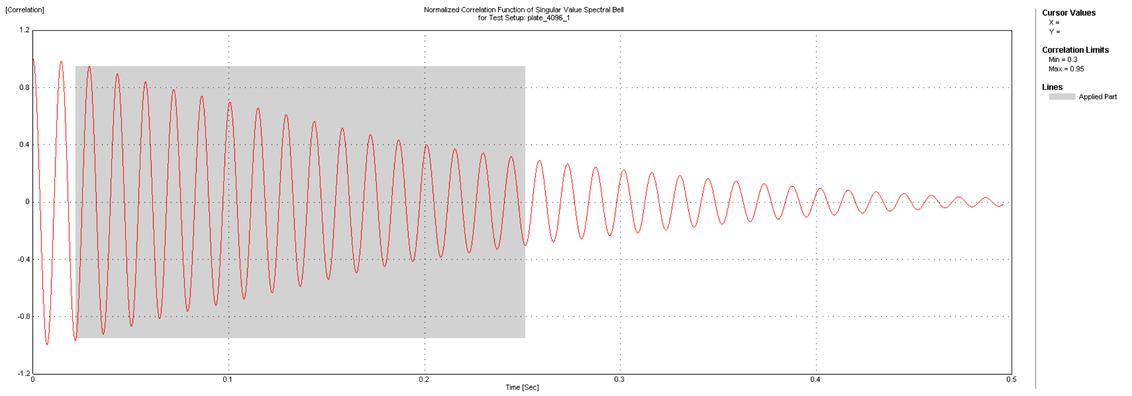

Figure 2.5: Correlation function derived from inverse Fourier transform of the selected frequency band. The grey area represents the duration of the time lag used for actual estimation of modal parameters. The beginning and end of the correlation function are discarded because they are dominated by non-linearity effects.

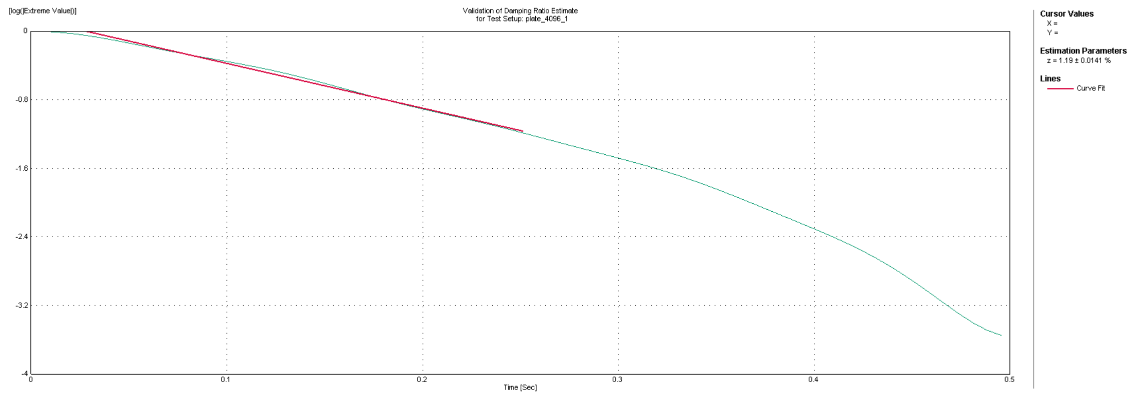

Figure 2.6: Plot of correlation function maxima in logarithmic scale for the estimation of the damping ratio of a mode. The red line is a logarithmic regression of the time lag selected by the grey rectangle in Figure 2.5. The slope of the line determines the estimated damping ratio.

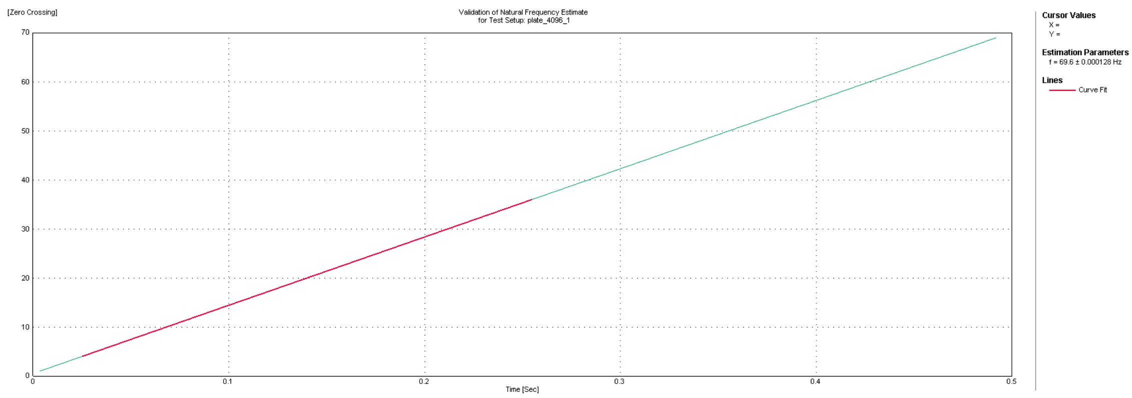

Figure 2.7: Number of zero crossings of the correlation function since time lag 0. Without the presence of significant variation, the curve is plotted as a straight line. The slope of the linear regression curve determines the natural frequency of the mode.

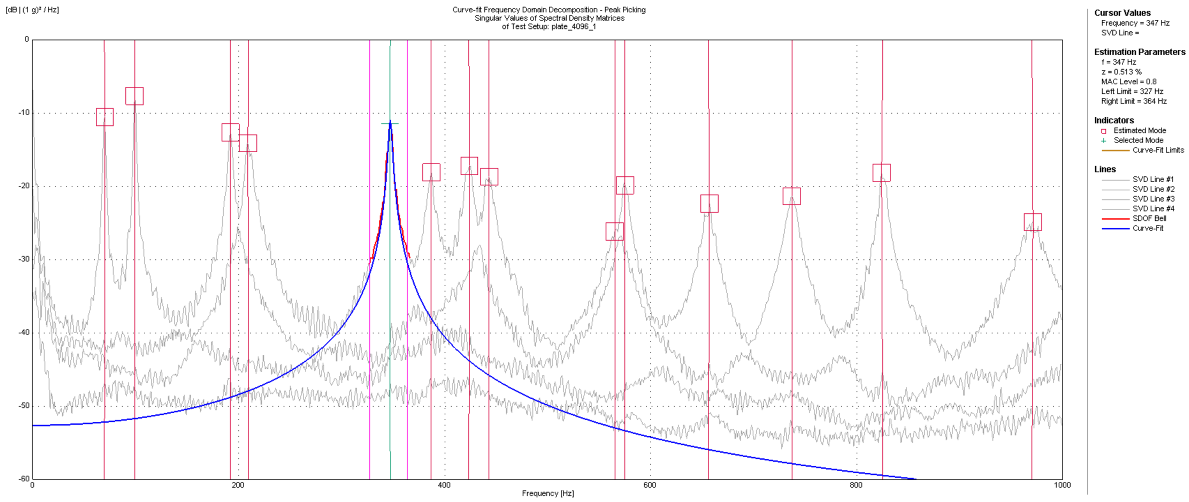

Figure 2.8: Estimation of a mode using the Curve-fit Frequency Domain Decomposition method. The peak of the first singular value at 347 Hz is selected and a spectral bell of a single-degree-of-freedom oscillator (blue) is fitted onto the selected frequency band (highlighted red portion of the singular value peak).

statement has been made so far about how accurate the identification is and how reasonable a declaration of the value to several digits after the decimal point would be.

2.2.3 Curve-fit FDD

Curve-fit Frequency Domain Decomposition (CFDD) is another enhancement to FDD available in ARTeMIS Extractor. It is described in detail by a paper of Jacobsen [19]. The main benefit is a more accurate estimation of the natural frequencies and damping ratios both in case of pure stochastic excitation and in the presence of deterministic excitation (i.e. harmonics).

Mode shape estimation works in the same way as described in EFDD above. Using the MAC value as threshold, a frequency band around a FDD selected peak is used to average singular vectors. As shown in Figure 2.8, natural frequency and damping ratio are estimated by curve-fitting the SDOF spectral density function (the “SDOF spectral bell”) in frequency domain. The approximation of a FRF of a SDOF oscillator can be expressed in fractional form as

$$H(f) = \frac{B_0 + B_1 e^{2\pi f T} + B_2 e^{4\pi f T}}{1 + A_1 e^{2\pi f T} + A_2 e^{4\pi f T}} \tag{2.18}$$

where T is the sampling interval and A_i and B_i are curve fitting parameters. Natural frequency and the damping ratio can then be extracted from the root of the denominator.

The fitting of the SDOF bell gives the analyst a straight-forward verification tool directly during the process. If the plot does not show a regular SDOF response function, starting at a constant value on the left (lower frequency) side and going towards zero on higher frequencies, then chances are high that some estimation parameters are not accurate.

By manually influencing the inclusion of the frequency band fringes – ARTeMIS provides some controls for this – one could be tempted to mitigate the effects of leakage by the Fourier transform. When a discrete Fourier transform is performed on a finite set of data samples, it appears that energy from a peak at a certain frequency ’leaks’ to neighboring frequencies, raising the energy level for those frequency lines [30]. This makes the frequency peak look wider than it actually is, yielding a damping ratio that is overestimated. By fitting a sharper SDOF bell to the resonance peak, the fit would counter-measure the overestimation of the damping ratio. On the other hand, a manual manipulation would bias the objectivity of the identification process in an uncontrollable matter. Who can tell how much sharper the SDOF should be? Nevertheless, it should be clear that a curve-fit which is wider than the resonance peak of the plotted SVD curve will yield a much overestimated damping ratio because the reality always lies closer to the narrow shape than to the wide one.

Thus, as it is true for every single estimation method, the modal parameters obtained by CFDD, should always be compared and validated against parameters which are obtained through additional methods, such as EFFD and the family of Stochastic Subspace Identification techniques (see Section 2.3).

2.2.4 Indicators used in Automated Estimation

The aim of a software dedicated to Operational Modal Analysi, such as ARTeMIS Extractor, is to provide a tool that supports the user in the identification process and take over as much workload as possible. Accordingly, the software introduces indicator functions, which, on the one hand, help the user to distinguish mode peaks from noise peaks and different mode peaks from each other, and, on the other hand, even tries to find these mode peaks automatically. The theory of these indicator functions is described in [10] and shall be summarized hereafter:

Modal Coherence Indicator

The modal coherence indicator function is defined as

$$d_1(f_0) = \overline{\mathbf{u}}_1^T(f)\mathbf{u}_1(f_0) \tag{2.19}$$

It denotes the correlation between the first singular vector at a selected frequency f_0 and a neighboring frequency f. If the modal coherence is close to unity, then the first singular value at the neighboring point correspond to the same modal coordinate as at f_0, and therefore the same mode is dominating. If it is close to 0, then the neighboring singular vectors are not correlated and therefore are not dominated by any mode but by noise instead.

Thus, $d_1(f_0)$ is providing a function over the whole frequency band, whether at f_0 there is either a dominating mode or mainly noise. ARTeMIS Extractor can plot this coherence function in the SVD plot as shown in Figure 2.9. A lot of blue from the top means low coherence and hence a lot of noise, whereas no blue means good coherence between neighboring frequency lines.

An automation algorithm then can use a threshold value Ω_1 (selectable by user input) to automatically discriminate modal peaks from noise peaks:

$$d_1 \geq \Omega_1 \tag{2.20}$$

The initial value of Ω_1 that is used by ARTeMIS as well as the gap of neighboring frequencies considered to calculate d_1 depend on the number of measurement channels. Additionally some averaging for several neighboring frequency lines is applied (no formula available as how exactly this is done in ARTeMIS).

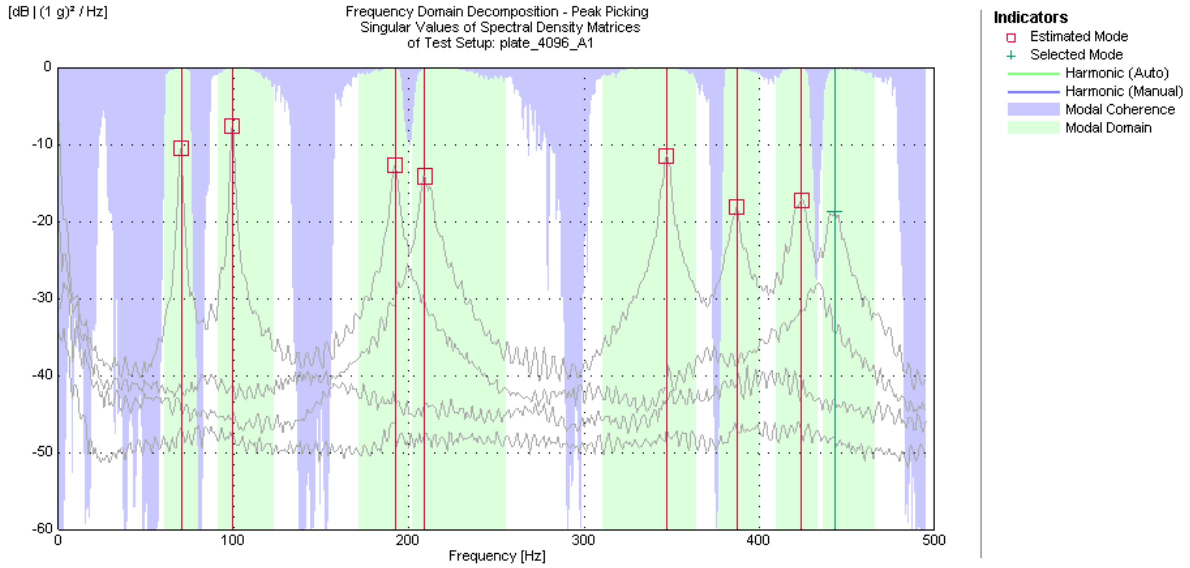

Figure 2.9: Singular value decomposition plot overlayed with plots of the modal coherence indicator (blue) and modal domains around a peak (green). See text for details.

Modal Domain Indicator

The formula for the modal domain indicator function looks very similar to the modal coherence function. But instead of being a function of the initial point given by f_0, it is a function of the frequency f of the considered neighboring points:

$$d_2(f) = \bar{\mathbf{u}}_1^T(f)\,\mathbf{u}_1(f_0) \tag{2.21}$$

Around a structural mode peak at f_0, the correlation should be high for a larger frequency range where that mode is dominating. By introducing a second threshold Ω_2, where

$$d_2 \geq \Omega_2 \tag{2.22}$$

a frequency range $[f_0 - \Delta f_1; f_0 + \Delta f_2]$ around that peak represents dominance of one mode. Thus, that range is called the *modal domain* and no second mode peak is considered for automatic mode selection inside that domain after the automatic peak selection has chosen the first one. In Figure 2.9, the modal domains of the distinct (and already selected) peaks are shown in green.

So, although the definitions of d_1 and d_2 almost look the same, the nature of the input parameters f and f_0 is different. While the input frequencies are close neighbors for the coherence indicator, the gap between the frequencies used for the domain indicator is a larger one. It goes from the peak to the edge of the modal domain.

2.3 Stochastic Subspace Identification

While FDD is a technique applied in the frequency domain, *Stochastic Subspace Identification (SSI)* is a method that works directly in time domain. Subspace identification techniques emerged from the field of system identification in system and control theory in the late 1980s. A comprehensive book [31] by van Overschee and De Moor in 1996 is considered to have triggered the break-through among system control engineers with respect to practical acceptance and application. Katayama [21] gives a detailed mathematical framework of subspace methods. Recently, the fields of civil and mechanical engineering have adopted SSI to include it into their special case of system identification [9, 5], which is the topic of this document.

While there exist subspace methods dealing either with deterministic input signals only, with stochastic input only and combined methods, this summary shall be limited to solely stochastic inputs as it is the case within the application of Stochastic Subspace Identification to Operational Modal Analysis. Just like in FDD, the input is not explicitly measured but assumed to consist of white noise. More specifically, it is assumed to be Gaussian white noise. The properties of Gaussian white noise are [24]:

- White noise has equal power at all frequencies, i.e. the PSD is constant for all frequencies. This property is used in FDD.
- *White* means that the signal is uncorrelated in time. In other words, if you know the value of the noise signal at specific time there is no way of using this knowledge for a prediction of the value at any other time. The flatness of the PSD is a direct effect of this property.
- *Gaussian* reflects the fact that at any given point in time the value of the signal follows a probability density function (PDF) with the shape of the normal distribution also known as Gaussian distribution[1].

2.3.1 Model Formulation

Since SSI has been developed in the field of statistics and control theory rather than in mechanical engineering, the nomenclature and notation of mathematics is different to the approach of FDD as described in Section 2.2. $\mathbf{x}(t)$ denotes the system state and $\mathbf{f}(t)$ is the (unknown) input as opposed to $\mathbf{x}(t)$ being the input in the previous section about FDD.

SSI uses state space formulation

$$\mathbf{x}(t) = \begin{bmatrix} \mathbf{y}(t) \\ \dot{\mathbf{y}}(t) \end{bmatrix} \tag{2.23}$$

transforming the classical system of second order equations (compare to Eq. (2.3))

$$\mathbf{M}\ddot{\mathbf{y}}(t) + \mathbf{D}\dot{\mathbf{y}}(t) + \mathbf{K}\mathbf{y}(t) = \mathbf{f}(t) \tag{2.24}$$

to a system of first order equations

$$\dot{\mathbf{x}}(t) = \mathbf{A}_c\mathbf{x}(t) + \mathbf{B}\mathbf{f}(t) \tag{2.25a}$$

$$\mathbf{y}(t) = \mathbf{C}\mathbf{x}(t) \tag{2.25b}$$

with the system matrices

$$\mathbf{A}_c = \begin{bmatrix} \mathbf{0} & \mathbf{I} \\ -\mathbf{M}^{-1}\mathbf{K} & -\mathbf{M}^{-1}\mathbf{D} \end{bmatrix} \tag{2.26a}$$

$$\mathbf{B} = \begin{bmatrix} \mathbf{0} \\ \mathbf{M}^{-1} \end{bmatrix} \tag{2.26b}$$

[1] see also Section 2.4

and the observation matrix $\mathbf{C}$.

The state space formulation explicitly distinguishes between inherent states of the system $\mathbf{x}(t)$ and the measured output of the system $\mathbf{y}(t)$ – a distinction which is not present in Eq. (2.24). The equations (2.23) and (2.26) are just one way to express the system in state space formulation. In fact there is an infinite number of possibilities to describe the system as long as the dimensions of the matrices fit the order of the system. They all create the same vector space. With a dimension of $n \times n$ for $\mathbf{A}$ and $n \times 1$ for the the state vectors $\mathbf{x}_i$, a number of $n/2$ modes can be described and identified to characterize the dynamics of the system. n is called the state space dimension. $\mathbf{C}$ is then the connection between the state space and the representation of the output vector which is determined by the choice of measurement instrumentation.

The objective of system identification techniques is to estimate the system matrix $\mathbf{A}$, from which the modal parameters can be calculated (see Section 2.3.8)[2].

The distinction between system states and measured system output allows for the consideration of noisy measurements through the term $\mathbf{v}(t)$. It is called the measurement noise. Also, the general input term $\mathbf{Bf}(t)$, which could consist of deterministic and stochastic excitation can in our case be replaced with a pure stochastic input vector $\mathbf{w}(t)$, also called the process noise. Both process noise and measurement noise are zero mean Gaussian white noise vectors.

$$\dot{\mathbf{x}}(t) = \mathbf{A}_c\mathbf{x}(t) + \mathbf{w}(t) \tag{2.27a}$$
$$\mathbf{y}(t) = \mathbf{C}\mathbf{x}(t) + \mathbf{v}(t) \tag{2.27b}$$

Since measurement data is obtained in discrete time samples, the system equations have to be denoted in discrete formulation, too:

$$\mathbf{x}_{t+1} = \mathbf{A}_d\mathbf{x}_t + \mathbf{w}_t \tag{2.28a}$$
$$\mathbf{y}_t = \mathbf{C}\mathbf{x}_t + \mathbf{v}_t \tag{2.28b}$$

$\mathbf{A}_d$ is the discrete system matrix and is not identical to the system matrix of the continuous model $\mathbf{A}_c$, but can be calculated from it and vice versa.

The idea of Stochastic System Identification is to estimate the system state sequence $\mathbf{x}_t$ from the measured response sequence $\mathbf{y}_t$ and then estimate the system matrices with a linear regression approach:

$$\begin{bmatrix} \hat{\mathbf{x}}_{i+1} & \hat{\mathbf{x}}_{i+2} & \dots & \hat{\mathbf{x}}_{i+j} \\ \mathbf{y}_i & \mathbf{y}_{i+1} & \dots & \mathbf{y}_{i+j-1} \end{bmatrix} = \begin{bmatrix} \mathbf{A}_d \\ \mathbf{C} \end{bmatrix} \begin{bmatrix} \hat{\mathbf{x}}_i & \hat{\mathbf{x}}_{i+1} & \dots & \hat{\mathbf{x}}_{i+j-1} \end{bmatrix} + \begin{bmatrix} \rho_w \\ \rho_v \end{bmatrix} \tag{2.29}$$

The hat on the system states $\hat{\mathbf{x}}_t$ denotes that these states are estimates rather than the actual system states. ρ_w and ρ_v are the residuals of the regression. These residuals are to be minimized during the regression analysis. They should become close to zero when a sufficiently large set of measurement samples and sequence of system states is available. Otherwise either $\mathbf{w}_t$ and $\mathbf{v}_t$ are not zero mean or $\mathbf{A}_d$ and $\mathbf{C}$ are not constant. That would indicate the experiment was poorly prepared or conducted, or the data quality was poor.

2.3.2 Kalman filter

Theory says that with the assumption of Gaussian white noise as input, which is fully described by its mean and covariance (see Section 2.3.4), the optimal algorithm to estimate (or "predict") the state sequence of a linear

[2] In the general application of system identification, there is not just interest for $\mathbf{A}$ but for all the other matrices describing the system, too. But since we are mainly interested in modal parameters, a way of just finding $\mathbf{A}$ would be sufficient in our case.

system is a Kalman filter [24, 31, 21]. The following equations describe the Kalman filter in form of the so called innovation state space system:

$$\hat{\mathbf{x}}_{t+1} = \mathbf{A}_d \hat{\mathbf{x}}_t + \mathbf{K_t} \mathbf{e}_t \tag{2.30a}$$

$$\mathbf{y}_t = \mathbf{C} \hat{\mathbf{x}}_t + \mathbf{e}_t \tag{2.30b}$$

where $\mathbf{K_t}$ is the non-steady state Kalman gain and $\mathbf{e}_t$ the innovation process. Now, if the system matrices $\mathbf{A}_d$ and $\mathbf{C}$ as well as the initial states of the process were known, the Kalman filter could explicitly be implemented in an algorithm – either as software running in a controller computer or even in an integrated circuit. The filter would yield optimal estimates of the state sequences and would involve a so called algebraic Ricatti equation in order to calculate the Kalman gain. This would all be done on the fly by incorporating the output signal $\mathbf{y}_t$ in each new step, while covariance information from the past is automatically included in the estimation process. This is the common way how a Kalman filter is applied in a controller framework, e.g. for controlling a system which is mainly disturbed by Gaussian white noise.

In the case of Stochastic Subspace Identification, however, the system matrices are not known. After all, the goal is to identify them. Hence, there cannot be an explicit implementation of the Kalman filter as introduced in the above formulation. Instead, SSI provides a method to obtain the estimated system state sequences – or Kalman states – directly from measured output signals through the means of geometric tools from linear algebra, which have equivalents in the stochastic framework.

2.3.3 Geometric Properties

This section deals with the fundamental geometric element of subspace identification methods which gives them their name. Every matrix $\mathbf{A}$ can be considered as a set of row vectors, which define the basis for a linear vector space. This vector space is also called the *row space*. The number of linear independent vectors determine the rank of $\mathbf{A}$ and the dimension of the row space. Let j be the number of columns of $\mathbf{A}$ and thus the number of elements in a row vector. The row space is then a subspace of the j-dimensional ambient space.

Orthogonal Projection

The following operator defines the orthogonal projection of the row space of matrix $\mathbf{A} \in \mathbb{R}^{p \times j}$ onto the row space of matrix $\mathbf{B} \in \mathbb{R}^{q \times j}$:

$$\mathbf{A}/\mathbf{B} := \mathbf{A}\mathbf{B}^T \left(\mathbf{B}\mathbf{B}^T\right)^+ \mathbf{B} \tag{2.31}$$

where $(\cdot)^+$ denotes a Moore-Penrose pseudo-inverse [21, p. 34].

Figure 2.10 illustrates the orthogonal projection in the simple case of a two-dimensional ambient space. Both $\mathbf{A}$ and $\mathbf{B}$ are matrices of size 1×2. So they consist of one single row vector and their row space is one-dimensional. The projection $\mathbf{A}/\mathbf{B}$ now projects the row vector of $\mathbf{A}$ onto the row space of $\mathbf{B}$. Both row spaces of $\mathbf{A}$ and $\mathbf{B}$ are one-dimensional subspaces of the ambient two-dimensional space.

Overschee and De Moor [31] also describe the projection onto the orthogonal complement of $\mathbf{B}$ and define an oblique projection. But since the stochastic subspace algorithms only involve the orthogonal projection, there is no need for introducing them here.

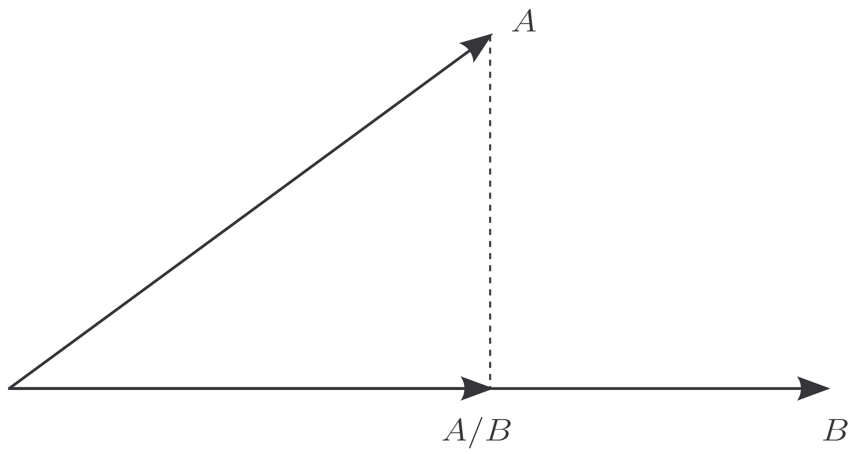

Figure 2.10: Orthogonal Projection of the row space of matrix A onto the row space of B. In this example, the row spaces of A and B have only one dimension while they lie in a two-dimensional ambient space.

In a stochastic context, the orthogonal projection is equivalent to the conditional expectation or conditional mean [7, p. 24].

$$\mathbf{A}/\mathbf{B} = \mathrm{E}[\mathbf{A}|\mathbf{B}] \tag{2.32}$$

The conditional expectation $\mathrm{E}[\mathbf{A}|\mathbf{B}]$ is the best possible (i.e. optimal) estimation of $\mathbf{A}$ when all the available information about $\mathbf{B}$ is included into the prediction.

Principal Angles and Directions

The principal angles between two subspaces are a generalization of the angle between two vectors. A recursive definition of principal angels and directions between $\mathbf{A} \in \mathbb{R}^{p\times j}$ and $\mathbf{B} \in \mathbb{R}^{q\times j}$ could be as follows: Find the two unit vectors out of the row space of $\mathbf{A}$ and $\mathbf{B}$, $\mathbf{a}_1$ and $\mathbf{b}_1$, which have a minimum angle between them. That angle is the first principal angle θ_1 and $\mathbf{a}_1$, $\mathbf{b}_1$ are the first principal directions. Next find the two unit vectors $\mathbf{a}_2 \perp \mathbf{a}_1$ and $\mathbf{b}_2 \perp \mathbf{b}_1$ with minimum angle between them. These are the second principal directions and principal angle. This procedure is continued until $\min(p,q)$ angles have been found.

Figure 2.11 shows the principal directions and angles of two intersecting planes. These planes are two-dimensional subspaces of the three dimensional ambient space. The first principal directions $\mathbf{a}_1$ and $\mathbf{b}_1$ lie in the intersection of the two planes. Accordingly, the first principal angle θ_1 is zero. The second principal angle θ_2 is the angle between the principal directions $\mathbf{a}_2$ and $\mathbf{b}_2$.

Principal angles and directions can also be calculated through the use of a singular value decomposition, for instance:

$$\left(\mathbf{A}\mathbf{A}^T\right)^{-1/2}\left(\mathbf{A}\mathbf{B}^T\right)\left(\mathbf{B}\mathbf{B}^T\right)^{-1/2} = \mathbf{U}\mathbf{S}\mathbf{V}^T \tag{2.33}$$

now, the principal directions and angles are:

$$\mathbf{a} = \mathbf{U}^T\left(\mathbf{A}\mathbf{A}^T\right)^{-1/2}\mathbf{A} \tag{2.34}$$

$$\mathbf{b} = \mathbf{V}^T\left(\mathbf{B}\mathbf{B}^T\right)^{-1/2}\mathbf{B} \tag{2.35}$$

$$\operatorname{diag}\left(\cos\theta_1, \cos\theta_2, \ldots, \cos\theta_{\min(p,q)}\right) = \mathbf{S} \tag{2.36}$$

The SVD approach to principal angles is used by the Canonical Variate Analysis algorithm (SSI-CVA, see page 29).

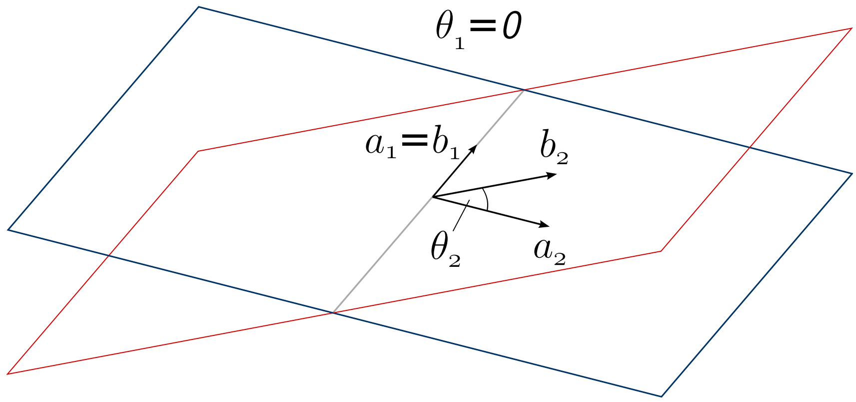

Figure 2.11: Principal angles for two two-dimensional subspaces in a three-dimensional ambient space. See text for details.

2.3.4 Covariance Matrices

Since $\mathbf{w}_t$ and $\mathbf{v}_t$ are considered to be zero-mean Gaussian white noise, they are fully described by their covariance matrices:

$$\mathrm{E}\left[\begin{bmatrix}\mathbf{w}_t \\ \mathbf{v}_t\end{bmatrix}\begin{bmatrix}\mathbf{w}_k \mathbf{v}_k\end{bmatrix}\right] = \begin{bmatrix}\mathbf{Q} & \mathbf{S} \\ \mathbf{S}^T & \mathbf{R}\end{bmatrix}\delta_{tk} \tag{2.37}$$

where $\mathbf{Q}$, $\mathbf{S}$ and $\mathbf{R}$ are the covariance matrices and δ_{tk} is the Kronecker delta.

$$\delta_{tk} = \begin{cases} 1 & t = k \\ 0 & t \neq k \end{cases} \tag{2.38}$$

The presence of $\mathbf{S}$ indicates that $\mathbf{v}_t$ and $\mathbf{w}_t$ could be correlated to each other. Nevertheless they are still Gaussian white noise, so that the covariance $\mathbf{S}$ between each other and the auto-covariance matrices $\mathbf{Q}$ and $\mathbf{R}$ are only non-zero for synchronous times, which is indicated through the Kronecker delta.

Similarly, the covariance matrices of input and output signals can be defined as follows:

$$\mathrm{E}\left[\mathbf{x}_t \mathbf{x}_t^T\right] := \mathbf{P} \tag{2.39}$$
$$\mathrm{E}\left[\mathbf{y}_{t+i} \mathbf{y}_t^T\right] := \Lambda_i \tag{2.40}$$
$$\mathrm{E}\left[\mathbf{x}_{t+1} \mathbf{y}_t^T\right] := \mathbf{G} \tag{2.41}$$

Strictly spoken, these covariances are defined as population covariances, or in other words over an infinite number of data points. However, if the number j of available data samples and corresponding system states is high enough, the covariance matrices can be approximated as sample covariances:

$$\mathbf{P} \approx \frac{1}{j-1} \begin{bmatrix} \mathbf{x}_0 & \mathbf{x}_1 & \dots & \mathbf{x}_{j-1} \end{bmatrix} \begin{bmatrix} \mathbf{x}_0 & \mathbf{x}_1 & \dots & \mathbf{x}_{j-1} \end{bmatrix}^T \tag{2.42}$$

$$\Lambda_i \approx \begin{cases} \frac{1}{j-i-1} \begin{bmatrix} \mathbf{y}_i & \dots & \mathbf{y}_{j-1} \end{bmatrix} \begin{bmatrix} \mathbf{y}_0 & \dots & \mathbf{y}_{j-i-1} \end{bmatrix}^T & , i \geq 0 \\ \frac{1}{j+i-1} \begin{bmatrix} \mathbf{y}_0 & \dots & \mathbf{y}_{j-1+i} \end{bmatrix} \begin{bmatrix} \mathbf{y}_{-i} & \dots & \mathbf{y}_{j-1} \end{bmatrix}^T & , i < 0 \end{cases} \tag{2.43}$$

$$\mathbf{G} \approx \frac{1}{j-2} \begin{bmatrix} \mathbf{x}_1 & \dots & \mathbf{x}_{j-1} \end{bmatrix} \begin{bmatrix} \mathbf{y}_0 & \dots & \mathbf{y}_{j-2} \end{bmatrix}^T \tag{2.44}$$

These equations become exact for $j \to \infty$. From this, it should be obvious that every experiment for system identification should obtain a sufficiently large set of measurement data.

The covariance matrices $\mathbf{Q}$, $\mathbf{S}$, $\mathbf{R}$ and $\mathbf{P}$ do not occur further in any of the equations given hereafter in order to explain the stochastic subspace techniques. Nevertheless it is important to note that these covariance matrices contain a lot of information about the system. Their knowledge would be essential for the explicit implementation of the Kalman filter as mentioned in Section 2.3.2 because they also occur in the Ricatti equation.

2.3.5 Controllability and Observability

The concept of observability and controllability is a very important aspect in modern control theory. Since it also affects the SSI algorithm, these terms need to be addressed here, too, although very rudimentary. Subspace methods make extensive use of the occurring matrices connected with these terms. Van Overschee and De Moor [31] address the terms mainly from this point of view, while Katayama [21] also gives fundamental mathematical definitions. For a more general introduction to the concept of controllability and observability, almost any introductory book about control theory or a specialized book with a general introduction part should be suitable, e.g. [29].

Controllability: *A system is controllable if for any initial state $\mathbf{x}_0$ and some final time k there exists a control that transfers the state to any desired value at time k [29, p. 38].*

Controllability depends on the system matrices $\mathbf{A}_d$ and $\mathbf{B}$. Thus, the statement that $(\mathbf{A}_d,\mathbf{B})$ is controllable is equivalent to the controllability of the system.

The controllability matrix $\mathcal{C}$ is defined as

$$\mathcal{C} = \begin{bmatrix} \mathbf{B} & \mathbf{A}_d\mathbf{B} & \cdots & \mathbf{A}_d^{n-1}\mathbf{B} \end{bmatrix} \tag{2.45}$$

$\operatorname{rank}(\mathcal{C}) = n$ is a necessary and sufficient condition for the controllability of $(\mathbf{A}_d,\mathbf{B})$.

There is no deterministic input matrix $\mathbf{B}$ in our stochastic model. Still, the introduction of $\mathcal{C}$ helps to understand the name of the *reversed extended stochastic controllability matrix* Δ_i

$$\Delta_i = \begin{bmatrix} \mathbf{A}_d^{i-1}\mathbf{G} & \mathbf{A}_d^{i-2}\mathbf{G} & \cdots & \mathbf{A}_d\mathbf{G} & \mathbf{G} \end{bmatrix} \tag{2.46}$$

In the stochastic case, controllability means that all dynamical modes of the system are excited by the process noise. This is important because modes that are not excited, can not be identified. Katayama [21] talks about reachability in conjunction with controllability.

Observability: *A system is observable if the initial state* $\mathbf{x}_0$ *can be completely recovered by n observations* $\begin{bmatrix}\mathbf{y}_0 & \mathbf{y}_1 & \dots & \mathbf{y}_{n-1}\end{bmatrix}$ *[21, p. 53].*

If certain dynamical modes of a system are not observable, they can obviously not be identified, even if they are excited. In the case of structural modal analysis, this is equivalent to a proper instrumentation of the structure in order to be able to identify modes and distinguish between different modes by meeting orthogonality requirements.

The observability matrix Γ is defined as

$$\Gamma = \begin{bmatrix} \mathbf{C} \\ \mathbf{CA}_d \\ \mathbf{CA}_d^2 \\ \vdots \\ \mathbf{CA}_d^{n-1} \end{bmatrix} \tag{2.47}$$

$\operatorname{rank}(\Gamma) = n$ is a necessary and sufficient condition for the observability of $(\mathbf{A}_d, \mathbf{C})$.

The *extended observability matrix* Γ_i is then

$$\Gamma_i = \begin{bmatrix} \mathbf{C} \\ \mathbf{CA}_d \\ \mathbf{CA}_d^2 \\ \vdots \\ \mathbf{CA}_d^{i-1} \end{bmatrix} \tag{2.48}$$

where i in Δ_i and Γ_i refers to the number of block rows in the halves of the block Hankel matrix (see Section 2.3.6)

2.3.6 The Estimation Algorithm

Suppose there was a experiment from which a sufficient large number of $N \to \infty$ measurement samples are available:

$$\mathbf{Y} = \begin{bmatrix}\mathbf{y}_0 & \mathbf{y}_1 & \cdots & \mathbf{y}_{N-1}\end{bmatrix} \tag{2.49}$$

These sample vectors can be used to form a so called *block Hankel matrix*

$$\mathbf{Y}_h = \left[\begin{array}{cccc} \mathbf{y}_0 & \mathbf{y}_1 & \cdots & \mathbf{y}_{j-1} \\ \mathbf{y}_1 & \mathbf{y}_2 & \cdots & \mathbf{y}_j \\ \vdots & \vdots & & \vdots \\ \mathbf{y}_{i-1} & \mathbf{y}_i & \cdots & \mathbf{y}_{i+j-2} \\ \hline \mathbf{y}_i & \mathbf{y}_{i+2} & \cdots & \mathbf{y}_{i+j-1} \\ \mathbf{y}_{i+1} & \mathbf{y}_{i+2} & \cdots & \mathbf{y}_{i+j} \\ \vdots & \vdots & & \vdots \\ \mathbf{y}_{2i-1} & \mathbf{y}_{2i} & \cdots & \mathbf{y}_{2i+j-2} \end{array}\right] = \left[\frac{\mathbf{Y}_{hp}}{\mathbf{Y}_{hf}}\right] \tag{2.50}$$

where $2i + j - 1 = N$. The name block Hankel matrix comes from the fact that the block anti-diagonals contain the same element of the measurement sequence.

$\mathbf{Y}_h$ can be separated into the "past" $\mathbf{Y}_{hp}$ and into the "future" $\mathbf{Y}_{hf}$. This definition is somewhat loose, since all of the measurement data was supposedly acquired in the past. Nevertheless, the terms are used in the literature and proved to be convenient in the explanations of concepts intuitively.

Similarly, the output covariance matrices as defined in equation (2.40) can be arranged in a block Toeplitz matrix:

$$\mathbf{L}_i = \begin{bmatrix} \Lambda_0 & \Lambda_{-1} & \Lambda_{-2} & \cdots & \Lambda_{1-i} \\ \Lambda_1 & \Lambda_0 & \Lambda_{-1} & \cdots & \Lambda_{2-i} \\ \Lambda_2 & \Lambda_1 & \Lambda_0 & \cdots & \Lambda_{3-i} \\ \vdots & \vdots & \vdots & \ddots & \vdots \\ \Lambda_{i-1} & \Lambda_{i-2} & \Lambda_{i-3} & \cdots & \Lambda_0 \end{bmatrix} \tag{2.51}$$

In a Toeplitz matrix, the elements on the diagonals are the same.

Using equation (2.43), the covariance Toeplitz matrix can be expressed either through the future or through the past:

$$\mathbf{L}_i = \frac{1}{j-1}\mathbf{Y}_{hp}\mathbf{Y}_{hp}^T = \frac{1}{j-1}\mathbf{Y}_{hf}\mathbf{Y}_{hf}^T \tag{2.52}$$

Now suppose that there is a non-steady state Kalman filter which starts at time q and uses i measurement samples until time $q+i-1$. The filter thus estimates the corresponding Kalman state at time $q+i$. It can be shown [31] that this Kalman state can be explicitly expressed as

$$\hat{\mathbf{x}}_{q+i} = \Delta_i \mathbf{L}_i^{-1} \begin{bmatrix} \mathbf{y}_q \\ \mathbf{y}_{q+1} \\ \vdots \\ \mathbf{y}_{q+i-1} \end{bmatrix} \tag{2.53}$$

By obtaining a sequence of j such Kalman filter state estimates $\hat{\mathbf{X}}_i = \begin{bmatrix} \hat{\mathbf{x}}_i & \hat{\mathbf{x}}_{i+1} & \dots & \hat{\mathbf{x}}_{i+j-1} \end{bmatrix}$, (2.53) expands to

$$\hat{\mathbf{X}}_i = \Delta_i \mathbf{L}_i^{-1} \begin{bmatrix} \mathbf{y}_0 & \mathbf{y}_1 & \dots & \mathbf{y}_{j-1} \\ \mathbf{y}_1 & \mathbf{y}_2 & \dots & \mathbf{y}_j \\ \vdots & \vdots & & \vdots \\ \mathbf{y}_{i-1} & \mathbf{y}_i & \dots & \mathbf{y}_{i+j-2} \end{bmatrix} \tag{2.54}$$

The matrix containing the output samples is identical to the "past" of the Block hankel matrix, $\mathbf{Y}_{hp}$. By including (2.52), the Kalman state sequence can now be written as

$$\hat{\mathbf{X}}_i = \Delta_i \left(\frac{1}{j-1}\mathbf{Y}_{hp}\mathbf{Y}_{hp}^T \right)^{-1} \mathbf{Y}_{hp} \tag{2.55}$$

On the other hand, the following equation holds [31]:

$$
\begin{aligned}
\mathbf{C}_i &= \frac{1}{j-1}\mathbf{Y}_{hf}\mathbf{Y}_{hp}^T \\
&= \begin{bmatrix} \Lambda_i & \Lambda_{i-1} & \dots & \Lambda_2 & \Lambda_1 \\ \Lambda_{i+1} & \Lambda_i & \dots & \Lambda_3 & \Lambda_2 \\ \Lambda_{i+2} & \Lambda_{i+1} & \dots & \Lambda_4 & \Lambda_3 \\ \vdots & \vdots & & \vdots & \vdots \\ \Lambda_{2i-1} & \Lambda_{2i-2} & \dots & \Lambda_{i+1} & \Lambda_i \end{bmatrix} \\
&= \begin{bmatrix} \mathbf{CA}_d^{i-1}\mathbf{G} & \mathbf{CA}_d^{i-2}\mathbf{G} & \dots & \mathbf{CA}_d\mathbf{G} & \mathbf{CG} \\ \mathbf{CA}_d^{i}\mathbf{G} & \mathbf{CA}_d^{i-1}\mathbf{G} & \dots & \mathbf{CA}_d^2\mathbf{G} & \mathbf{CA}_d\mathbf{G} \\ \mathbf{CA}_d^{i+1}\mathbf{G} & \mathbf{CA}_d^{i}\mathbf{G} & \dots & \mathbf{CA}_d^3\mathbf{G} & \mathbf{CA}_d^2\mathbf{G} \\ \vdots & \vdots & & \vdots & \vdots \\ \mathbf{CA}_d^{2i-2}\mathbf{G} & \mathbf{CA}_d^{2i-1}\mathbf{G} & \dots & \mathbf{CA}_d^{i}\mathbf{G} & \mathbf{CA}_d^{i-1}\mathbf{G} \end{bmatrix} \\
&= \Gamma_i\Delta_i
\end{aligned} \tag{2.56}
$$

Finally, a combination of (2.55) and (2.56) yields:

$$
\begin{aligned}
\Gamma_i\hat{\mathbf{X}}_i &= \Gamma_i\Delta_i\left(\frac{1}{j-1}\mathbf{Y}_{hp}\mathbf{Y}_{hp}^T\right)^{-1}\mathbf{Y}_{hp} && (2.57)\\
&= \mathbf{C}_i\left(\frac{1}{j-1}\mathbf{Y}_{hp}\mathbf{Y}_{hp}^T\right)^{-1}\mathbf{Y}_{hp} && (2.58)\\
&= \frac{1}{j-1}\mathbf{Y}_{hf}\mathbf{Y}_{hp}^T\left(\frac{1}{j-1}\mathbf{Y}_{hp}\mathbf{Y}_{hp}^T\right)^{-1}\mathbf{Y}_{hp} && (2.59)\\
&= \mathbf{Y}_{hf}\mathbf{Y}_{hp}^T\left(\mathbf{Y}_{hp}\mathbf{Y}_{hp}^T\right)^{-1}\mathbf{Y}_{hp} && (2.60)\\
&= \mathbf{Y}_{hf}/\mathbf{Y}_{hp} && (2.61)
\end{aligned}
$$

We now have a practical use of the orthogonal projection of the "future" onto the "past":

$$
O_i := \mathbf{Y}_{hf}/\mathbf{Y}_{hp} = \Gamma_i\hat{\mathbf{X}}_i \tag{2.62}
$$

The above equation shows that the combination of the extended observability matrix Γ_i and the Kalman states $\hat{\mathbf{X}}_i$ is directly calculated from measured data collected in the block Hankel matrix $\mathbf{Y}_h$. Because of this, the method described here is also called a "data driven" identification technique (*SSI-DATA*), whereas "covariance driven" techniques (*SSI-COV*) first compute the covariances Λ_i between the measured responses explicitly and estimate the system matrices from those [16]. That class of techniques, which is not used in *ARTeMIS*, shall not be discussed further in this document.

The next step is to extract the extended observability matrix Γ_i and the Kalman state sequence $\hat{\mathbf{X}}_i$ from the projection O_i. For this, a singular value decomposition is employed. Among the existing SSI algorithms there are actually differences in what serves as input for the decomposition. As shown in [31], all the three algorithms *Unweighted Principal Component (UPC)*, *Principal Component (PC)* and *Canonical Variate Analysis (CVA)*, which are also implemented in *ARTeMIS Extractor*, can be described with the use of two weight matrices $\mathbf{W}_1$ and $\mathbf{W}_2$ applied to O_i. Still, O_i is common to all three algorithms. Thus, it is also called the *common SSI input matrix*.

$$\begin{aligned}\mathbf{W}_1 O_i \mathbf{W}_2 &= \mathbf{W}_1 \Gamma_i \hat{\mathbf{X}}_i \mathbf{W}_2 \\ &= \begin{bmatrix}\mathbf{U}_1 & \mathbf{U}_2\end{bmatrix} \begin{bmatrix}\mathbf{S}_1 & \mathbf{0} \\ \mathbf{0} & \mathbf{0}\end{bmatrix} \begin{bmatrix}\mathbf{V}_1^T \\ \mathbf{V}_2^T\end{bmatrix} \\ &= \mathbf{U}_1 \mathbf{S}_1 \mathbf{V}_1^T\end{aligned} \tag{2.63}$$

Unweighted Principal Component: Although the SSI-UPC algorithm does not estimate Γ_i directly from O_i, it can be shown that the method is equivalent. The weight matrices are identity matrices (of appropriate sizes).

$$\mathbf{W}_1 = \mathbf{I} \tag{2.64a}$$
$$\mathbf{W}_2 = \mathbf{I} \tag{2.64b}$$

Principal Component: The SSI-PC algorithm is equivalent to applying the following weight matrices:

$$\mathbf{W}_1 = \mathbf{I} \tag{2.65a}$$
$$\mathbf{W}_2 = \mathbf{Y}_{hp}^T \mathbf{L}_i^{-1/2} \mathbf{Y}_{hp} \tag{2.65b}$$

Canonical Variate Analysis: SSI-CVA computes the principal angles and directions (see Section 2.3.3) between the row spaces of $\mathbf{Y}_{hp}$ and $\mathbf{Y}_{hf}$. Once again, this is equivalent to applying the weight matrices:

$$\mathbf{W}_1 = \mathbf{L}_i^{-1/2} \tag{2.66a}$$
$$\mathbf{W}_2 = \mathbf{I} \tag{2.66b}$$

Since the weight matrices are the only effective differences, the results of the algorithms should be very similar. The advantage of the CVA algorithm is the ability to estimate modes with a larger difference in energy level. This comes from the fact that CVA evaluates the principal directions of the row spaces rather than the length of the row vectors. On the other hand, according to [4], the algorithm demands a larger state space dimension in order to distinguish weakly excited modes when they are close to well-excited ones.

2.3.7 State Space Dimension and Stabilization Diagram

By the use of SVD (2.63), the extended observability matrix and the Kalman state sequence are now at hand:

$$\mathbf{W}_1 \Gamma_i \cdot \hat{\mathbf{X}}_i \mathbf{W}_2 = \mathbf{U}_1 \mathbf{S}_1^{\frac{1}{2}} \mathbf{T} \cdot \mathbf{T}^{-1} \mathbf{S}_1^{\frac{1}{2}} \mathbf{V}_1^T \tag{2.67a}$$
$$\Gamma_i = \mathbf{W}_1^{-1} \mathbf{U}_1 \mathbf{S}_1^{\frac{1}{2}} \mathbf{T} \tag{2.67b}$$
$$\hat{\mathbf{X}}_i = \mathbf{T}^{-1} \mathbf{S}_1^{\frac{1}{2}} \mathbf{V}_1^T \mathbf{W}_2^{-1} \tag{2.67c}$$

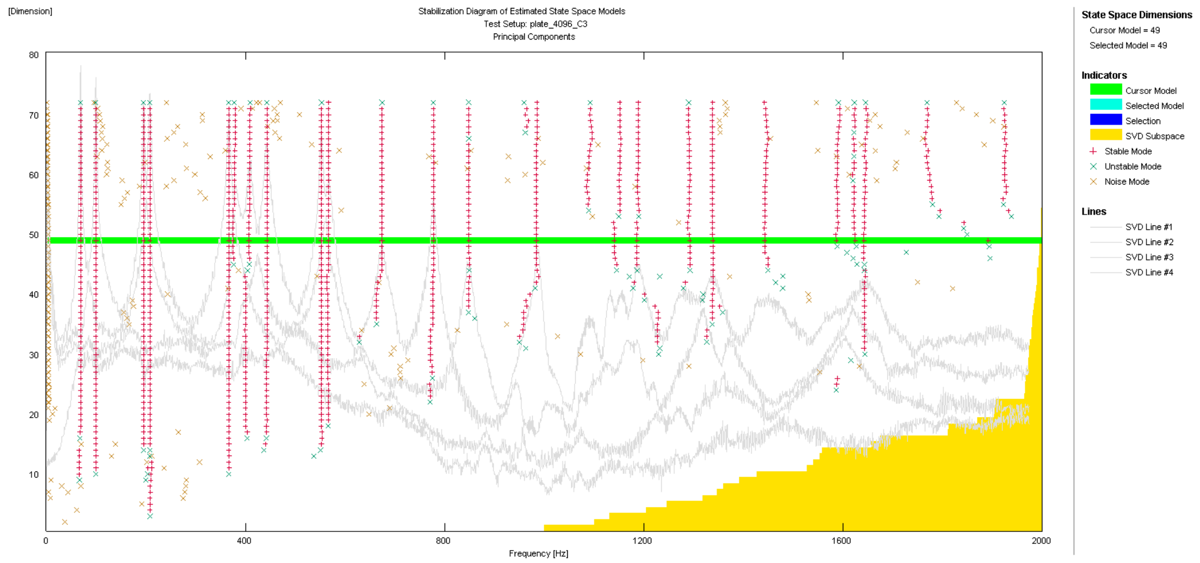

Figure 2.12: A stabilization diagram as implemented in ARTeMIS Extractor (see Chapter 3). See text for details.

As already mentioned in Section 2.3.1, the choice of the system matrices and system states is not unique. Their basis in the state space depends on the used algorithm. As a consequence of that, Γ_i and $\hat{\mathbf{X}}_i$ are not unique, either. This is reflected by the introduction of the non-singular $n \times n$ matrix $\mathbf{T}$ in Equation (2.63). By the use of different weighting matrices, a "different" extended observability matrix and Kalman state sequence is obtained, in the sense that they are represented in a different basis for the same state space. $\mathbf{T}$ is the similarity transform that would bring them into the same basis for all algorithms.

The selection of non-zero singular values $\mathbf{S}_1$ ensures that, although the size $2i$ of the block hankel matrix has been chosen arbitrarily, the actual state space dimension n is now determined and implied by the sizes of Γ_i and $\hat{\mathbf{X}}_i$. So the SVD crops the matrix dimensions to the relevant subspace onto which the system was projected by O_i.

In a perfect world, O_i would have a rank of n and $\mathbf{S}_1$ would consist of n singular values, reflecting the exact state space dimension. All subsequent singular values would be identical to zero. However, due to measurement noise and non-linearities, there is usually no distinguished cutoff. The choice of the number of singular values to be included into the estimation of Γ_i and $\hat{\mathbf{X}}_i$ is therefore somewhat arbitrary. If too few singular values are taken into account, the dimension of the estimated state space model is too small and not all modes can be recognized. If the dimension chosen is too large on the other hand, additional noise modes are introduced into the model, influencing the estimation of structural modes in a negative way.

To overcome this limitation, multiple mode estimates with increasing model dimension are obtained. The estimated modes are then being plotted on a stabilization diagram. Since the properties of the structure remain the same, structural modes should remain "stable", once a sufficiently high order has been reached but before too many noise modes influence the estimation too much. In contrast, noise modes should be different at any model order and therefore they do not stabilize onto a single frequency. Figure 2.12 shows the implementation of such a stabilization diagram. The order of the estimated model increases from the bottom to the top. While the first modes start to stabilize at a model order of approximately 20, most modes are estimated consistently starting around an order of 50. For higher model orders, more and more noise modes are included by the algorithm, which diminishes estimation quality again. So the model order of 49 is selected – indicated by the green bar – for further verification and to yield the parameters for the estimated modal model. The horizontal yellow bars on the right side of the diagram indicate the value of the smallest singular value in the corresponding model order. If the smallest singular value is significantly different from zero, then there are still modes left, which could not be estimated because the model order is too low. As soon as the singular values reach zero, then the full rank of the common SSI input matrix is represented by the corresponding model order. In the background of the diagram, the singular value decomposition of spectral densities is plotted like it is done for the methods of Frequency Domain Decomposition. These spectral densities have nothing to do with the actual SSI algorithm, but the plot is very convenient for the validation of estimated modes, because they stabilize at the peaks of the spectral densities, such as the frequency domain algorithms would detect them.

Since the size of the block hankel matrix $\mathbf{Y}_h$ determines the size of O_i, the maximum model order to estimate in the stabilization diagram is limited by the choice of the dimension for $\mathbf{Y}_h$. Example: If the block hankel matrix has a row dimension of $2i = 80$, then the maximum model order would be $n = 40$ and a maximum of 20 modes could be determined.

2.3.8 Modal Parameters from System Matrices

The system matrices can now be estimated, e.g., through the use of linear regression as proposed in (2.29); and modal parameters are found by eigenvalue decomposition:

$$\mathbf{A}_d = \Psi \begin{bmatrix} \mu_1 & & & \\ & \mu_2 & & \\ & & \ddots & \\ & & & \mu_n \end{bmatrix} \Psi^{-1} \tag{2.68}$$

$$\lambda_k = \frac{\ln \mu_k}{T} \tag{2.69}$$

$$\omega_k = |\lambda_k| \tag{2.70}$$

$$\zeta_k = \frac{\mathrm{Re}(\lambda_k)}{|\lambda_k|} \tag{2.71}$$

$$\Phi = \mathbf{C}\Psi \tag{2.72}$$

where

μ_k	discrete eigenvalues
Ψ	matrix of discrete time eigenvectors
T	sampling interval
λ_k	continuous time eigenvalues
ω_k	natural circular frequency
ζ_k	damping ratios
$\Phi = \begin{bmatrix} \phi_1 & \dots & \phi_n \end{bmatrix}$	matrix of continuous time eigenvectors

The complex eigenvalues occur as complex pairs and thus $n/2$ structural modes are identified. Since the eigenvalues of $\mathbf{A}_d$ don't depend on the basis of the state space in which the system matrix and the Kalman states have been obtained, it should be obvious now that although different algorithms with different weighting matrices yield different system matrices, the estimated modal parameters in the end are all the same. After all, those parameters are properties of the system and not properties of the specific method used.

2.4 Detecting Harmonics

As previously noted, the algorithms described above depend on the assumption that excitation forces consist of white noise. This can be considered true for many ambient processes which have stochastic nature. However, in mechanical structures there usually exist rotating and reciprocating devices such as engines, generators, turbines, fans, disk drives and so on, too. These devices excite the structure with harmonic loads and influence the response frequency spectrum significantly. Thus, algorithms are needed to detect and eliminate those influences. The approach described in this section works in the frequency domain. Hence, it is only applicable for the FDD algorithm but not for SSI. There is currently no specific solution available that would eliminate harmonic influences during the SSI estimation process. *Structural Vibration Solutions* advertises the SSI algorithms with the statement that harmonics would simply appear as additional modes during the identification process without influencing the estimation of structural modes. However, some experimental data as described in Section 4.6 indicates that dominant harmonics influence the detection of structural modes in a negative manner.

Automatic harmonic detection in ARTeMIS Extractor is based on kurtosis calculation [18] using the probability density function (PDF) $f(x)$. In statistics, the PDF denotes the distribution of a stochastic variable x over its value range. The kurtosis γ is used as an indicator how sharp or pointy the PDF of x is.

Like the mean μ of a population, also called the expected value $E[x]$ of the stochastic variable x, which can be expressed as the first moment of x,

$$\mu = E[x] = \int_{-\infty}^{+\infty} x f(x)\,\mathrm{d}x, \tag{2.73}$$

and the variance σ^2 as the second central moment of x,

$$\sigma^2 = E\left[(x-\mu)^2\right] = \int_{-\infty}^{+\infty} (x-\mu)^2 f(x)\,\mathrm{d}x, \tag{2.74}$$

the kurtosis is defined as the fourth central moment of the stochastic variable x normalized with respect to the standard deviation σ:

$$\gamma(x|\mu,\sigma) = \frac{E\left[(x-\mu)^4\right]}{\sigma^4} = \frac{\int_{-\infty}^{+\infty} (x-\mu)^4 f(x)\,\mathrm{d}x}{\sigma^4}. \tag{2.75}$$

Structural modes as response to stochastic input have a PDF distribution of Gaussian distributed bells. Harmonic excitations on the other hand produce a deterministic sinusoidal response at their excitation frequency throughout the measurement duration. The PDF of such a sinusoidal function is shown in Figure 2.13(b). The PDF of the sinusoidal function is much “pointier”. The kurtosis calculates to $\gamma = 1.5$. A Gaussian PDF, as shown in Figure 2.13(a), is wider and has a kurtosis of $\gamma = 3$.

In order to calculate the kurtosis, a narrow band-pass filter is applied around each frequency line and the PDF of measured accelerations in that frequency band is estimated. ARTeMIS Extractor calculates the value of the kurtosis for each estimated PDF and compares it to a user defined threshold value (default 3). All frequency lines below this threshold will be marked as harmonics. Subsequently, singular value peaks in those frequency bands are removed and replaced with a linear interpolation. A least squares regression based replacement algorithm has been introduced recently for CFDD, where extrapolation is made from both sides of the harmonic component. This has some advantages, especially when the harmonic component is very close to the peak of a structural mode. In that case, linear interpolation would cut off the peak yielding overestimation of the damping ratio.

The method has been introduced to supply a robust algorithm for automatic detection. Still, the analyst should check the data for himself and use his experience to be able to distinguish between structural modes and harmonic excitations:

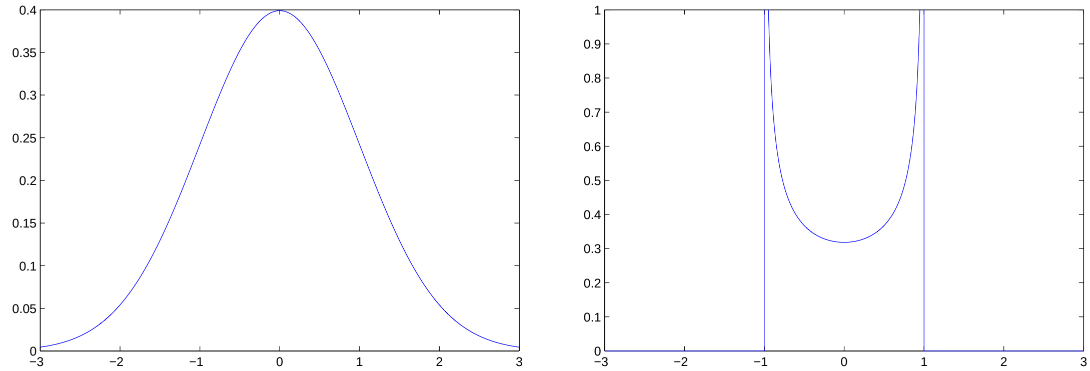

(a) Probability density function for stochastic excitation

(b) Probability density function for sinusoidal excitation

Figure 2.13: Difference in probability density functions for stochastic and harmonic excitations. The harmonic excitation yields a sinusoidal response which has a probability density with a kurtosis of $\gamma = 1.5$. The stochastic excitation is by the premise of the experimental method, Gaussian distributed white noise, and yields a Gaussian distributed response, which has a probability density with a kurtosis of $\gamma = 3$.

- A narrow peak in more than one singular value indicates a harmonic excitation in contrast to a peak of a structural mode in only one singular value. If a harmonic is present it excites all existing modes to the extend of their participation factor. Thus, all singular values show a peak at the frequency of the harmonic excitation.
- When being animated, an estimated structural mode shape should be shown as a “normal” mode. In a normal mode, all parts of the structure have a coherent phase angle so the mode shape vector can be expressed without imaginary components. The mode is animated with stationary nodal lines. On the other hand, if a peak in the frequency plot has been selected, which is due to harmonic excitation instead of a structural mode, it is likely that more than one structural mode participates at that frequency. This results in imaginary components or different phase angles of channels. Such a “complex” mode has non-stationary nodal lines in the animation and is not a distinguished structural mode with modal parameters.
- Very low calculated damping ratios may be due to a harmonic excitation constantly feeding the structure with power.

2.5 Projection Channels

When detecting harmonics, calculating the kurtosis for every frequency line for every channel can be very time consuming. Since there is much redundant information in a full-sized PSD-matrix $\mathbf{G}_{yy}$, including all measurement channels of a large test setup, it might not be necessary to include all measurement data into the calculation of harmonic detection. The use of projection channels reduces the amount of data by eliminating redundant information.

The same motivation holds for data used in the SSI algorithms. Using the right subset of measurement channels when calculating the common SSI input matrix, or the “projection”, O_i, reduces computation load while not too much information is lost due to the redundancy. The term projection channels probably originates from this algorithm although it is used with kurtosis calculation for harmonic detection as well.

Projection channels are simply a subset of measurement channels and are selected automatically by the software by evaluating the correlation coefficients between all measurement channels [19]. The correlation coefficient between two channels y_k and y_l is defined as

$$C_{kl} = \frac{E\left[y_k(t)y_l(t)\right]}{\sqrt{E\left[y_k(t)y_k(t)\right]E\left[y_l(t)y_l(t)\right]}} \tag{2.76}$$

using stochastic notation again, where E is the expectation operator. For a sufficient large set of N zero mean measurement samples the correlation coefficient becomes

$$C_{kl} = \frac{\sum_{i=1}^{N} y_k(t_i)y_l(t_i)}{\sqrt{\sum_{i=1}^{N} y_k^2(t_i)\sum_{i=1}^{N} y_l^2(t_i)}} \tag{2.77}$$

The selection of p channels is performed as follows:

- In a multi-test setup, select the reference channels as primary projection channels
- In a single-test setup, calculate the sum of all correlations of one channel to all other channels.

$$W_k = \sum_{l=1}^{m} |C_{kl}| \quad l \neq k, k = 1, \ldots, m \tag{2.78}$$

  The channel with the highest value of W_k has the highest correlation with all other channels and is presumed to bear the most information. This channel is selected as primary projection channel.
- Discard channels that have insignificant correlation with *any* other channel. It might be bad due to a faulty sensor.
- Subsequently, select the channel with the lowest correlation to the previously selected projection channels. It should introduce the most new information.
- Repeat the previous step until p channels have been selected.

The limitation of available data to the number of p projection channels yields a smaller PSD Matrix of the measured response $\mathbf{G}_{yy}$, which is not square anymore. It has m rows of all measurement channels but only p columns of selected projection channels. The singular value decomposition of this matrix still shows the first dominating singular values we are interested in. But the singular values of lower order, which should be simply a horizontal graph in the frequency plots, are not present anymore and thus don't have to be examined.

The number p of projection channels is a user provided parameter in ARTeMIS Extractor (see Chapter 3). It can be determined by the analyst by looking at the SVD plot of a full data set or at a data set with still a high number of p. All the singular value curves with small values that show no peak at all indicate redundant information. So the number of projection channels can be reduced by the number of such horizontal curves.

2.6 Conclusions

Although intended to serve the same objective of finding modal parameters of a structural system, the two identification techniques described above are very different in nature.

Frequency Domain Decomposition (FDD), including its enhanced versions *Enhanced Frequency Domain Decomposition (EFFD)* and *Curve-fit Frequency Domain Decomposition (CFDD)*, has a very straight forward approach providing the analyst with a good “feeling” about the measured data through visual inspection of singular value plots. Frequentially close modes can be detected by peaks in more than one singular value curves. In such a case, it can be difficult to extract modal parameters for all contributing modes although it is known there are some, as curve fitting in EFDD and CFDD can experience some difficulties selecting the correct curve. Also there is always the presence of the leakage effect of the Fourier transform, which yields overestimated damping ratios.

Stochastic Subspace Identifiaction (SSI) is a highly automated technique requiring very few user input. It is capable of detecting closely distributed modes and yielding modal parameters for all of them. Since it works in time domain, leakage is not an issue. The main disadvantage of the stochastic method is the less straight forward validation process. Also, due to the time domain nature of SSI, it is not capable of eliminating the negative influence of harmonic excitation components.

The best approach to validate data is to use as much different techniques as possible and compare the identified models with regard to frequency, damping and mode shapes. Thus, all available methods should be employed together, which will yield some confidence to have a good approximation of the real system.

3 The Operational Modal Analysis Software ARTeMIS Extractor and ARTeMIS Testor

The methods of Operational Modal Analysis (OMA) as described in Chapter 2 have been implemented in a number of commercially available software packages. The *ARTeMIS* suite by the Danish software company *Structural Vibration Solutions A/S (SVS)* is one of the leading software packages available on the market dedicated to perform OMA and has been acquired by the DSI for exactly that purpose. *ARTeMIS* is an acronym of *Ambient Response-Testing and Modal Identification Software* and consists of the two applications *ARTeMIS Extractor* and *ARTeMIS Testor*.

The author of this study thesis made first contact with the *ARTeMIS* suite and OMA software during March 2009, when the DSI invited Nis Møller from SVS to conduct a seminar about *ARTeMIS* and OMA. During the time period of research and experimental work for the thesis at hand, some bug fixing and development builds of the software suite have been released and distributed to the DSI. Some of these bug fixes and improvements have been made possible by DSI bug reports and feature requests – mainly introduced by the thesis author [15]. The major version number used during the research, especially during the analysis of the aluminium plate experiment as described in Chapter 4, was *2009*. Later on, *ARTeMIS Extractor 2010* has been introduced on the DSI computer installation.

The expertise acquired during the employment of the *ARTeMIS* suite also yielded a handbook [14], which includes Chapter 2 of this thesis about the theory of OMA and which tries to explain most of the controls and adjustable properties within the applications. That handbook might be subject to updates of future *ARTeMIS* versions, when new features are implemented and need to be addressed.

3.1 ARTeMIS Testor

ARTeMIS Testor is a tool intended to efficiently merge measurement data and geometry information. It is used to prepare and export the data to serve as input for the actual OMA analysis performed with *ARTeMIS Extractor* – see Section 3.2. The main features are organized by a set of items in the main task bar and include:

Geometry Editor A basic editor to generate a geometry model of the measured structure and specify sensor locations. It also includes functions to import that geometry from external files such as the *Universal File Format (UFF)* [26]. Figure 3.1 shows the Geometry Editor with the geometry of the aluminium plate from the experiment of Chapter 4.

Data Organizer Measurement data can be imported from various file formats like UFF, simple ASCII files, or a specialized SVS format. The Data Organizer includes them into a test setup tree and certain properties of the channels can be examined or modified. The assignment of measurement channels to sensor locations and measurement directions also takes place within the Data Organizer task item like it is shown in Figure 3.2.

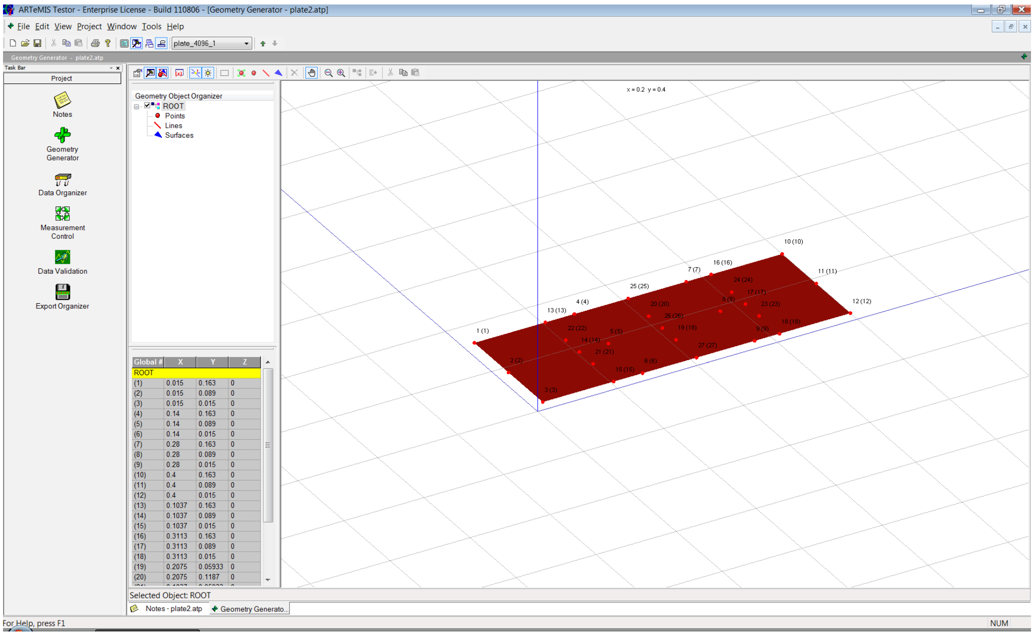

Figure 3.1: The Geometry Editor of ARTeMIS Testor. The screenshot shows the modeled geometry of a rectangular aluminium plate (see Chapter 4) with nodes (bright red dots), where accelerometer sensors are located.

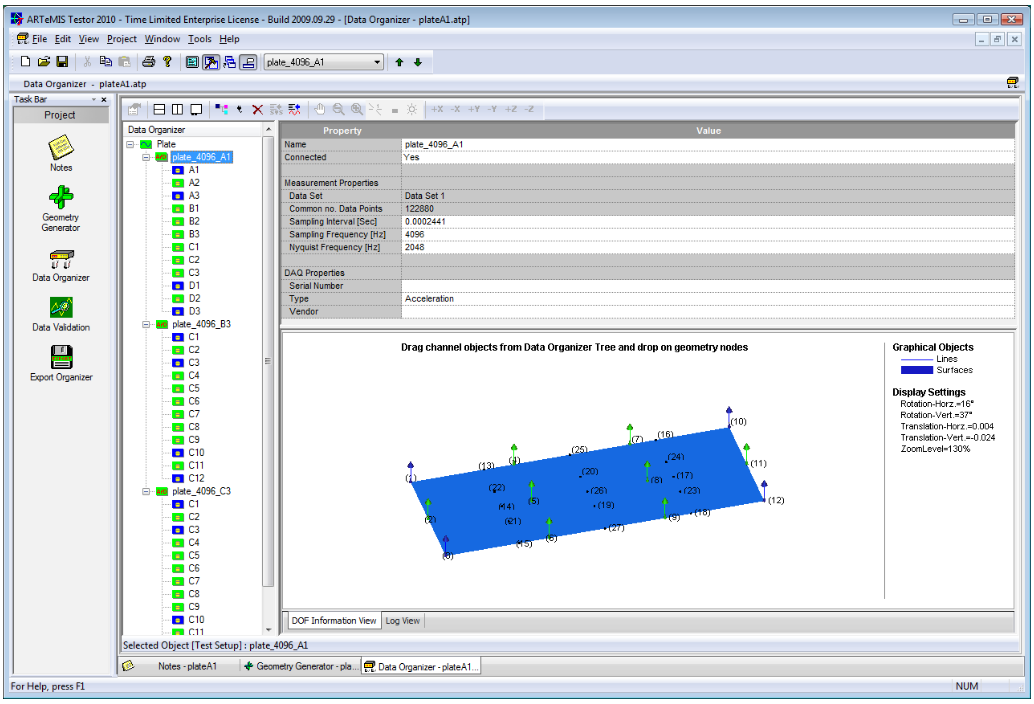

Figure 3.2: The Data Organizer of ARTeMIS Testor. Here the properties of the measurement channels are defined, including measurement direction and its location at a geometry node. The blue and green arrows represent such a measurement direction and sensor location either as reference channel or as a regular one.

Measurement Control The Measurement Control task item is able to directly acquire measurement data from specific data acquisition systems. Since the data acquisition systems of neither the one used during the aluminium plate experiment (see Section 4.2) nor those used within the SOFIA project are among the supported ones, this feature of *Testor* is not of further interest to the DSI or this study thesis.

Data Validation The measured channel signals can be examined in the time domain as well as with respect to their spectral components. A first glance at the imported data helps to evaluate whether the data is suitable for further analysis in *ARTeMIS Extractor*.

Export Organizer As soon as the measurement data and geometry information is fully prepared, this task item can be used to export the project into a suitable format that serves as input for *ARTeMIS Extractor*.

3.2 ARTeMIS Extractor

ARTeMIS Extractor is the primary application of the *ARTeMIS* software suite. The actual OMA of the provided measurement data takes place here. Suitable organized data either was prepared by *ARTeMIS Testor* (see Section 3.1) or by custom made tools such as described in Chapter 5. *Extractor* takes either SVS Project Files or a collection of files in Universal File Format as input.

The features of *ARTeMIS Extractor* are organized in a task bar similar to those in *Testor* and include:

Project Everything that has to do with signal processing and computing prior to the actual modal identification algorithms of Frequency Domain Decomposition (FDD) and Stochastic Subspace Identification (SSI):

- Examining geometry information and channel properties as previously defined by *Testor* or other tools.
- Processing signal data such as applying filters and adjusting the sampling rate.
- Specifying the use of projection channels (see Section 2.5).
- Applying methods to find harmonic excitation components (see Section 2.4).
- Plotting processed data in the frequency domain:
  - A Singular Value Decomposition as later used by FDD (see Section 2.2)
  - Magnitude plots of single channels and cross-spectra.
  - Phase angle plots between different channels.
  - Coherence plots between different channels.
  - Averages of all (cross- and auto-) spectra of all channels and averages of all auto-spectra of all channels.
  - Spectrogram of frequency components over time.
  - A plot of the harmonic indicator over frequency (see Section 2.4).
- Listing and organizing all identified modes, including their animation. This item does not fit into the premise given above but is nevertheless included into the “Project” task bar.

ODS *Operating Deflection Shapes (ODS)* show the overall vibration patterns of a structure either over a time segment or at a specific frequency. While the animation of such ODS is supported by *ARTeMIS Extractor*, the benefit of this particular feature for the SOFIA project is limited. For the SOFIA Telescope information of overall vibration is of interest especially when translated into image motion (see Section 5.4.1). But since *Extractor* can

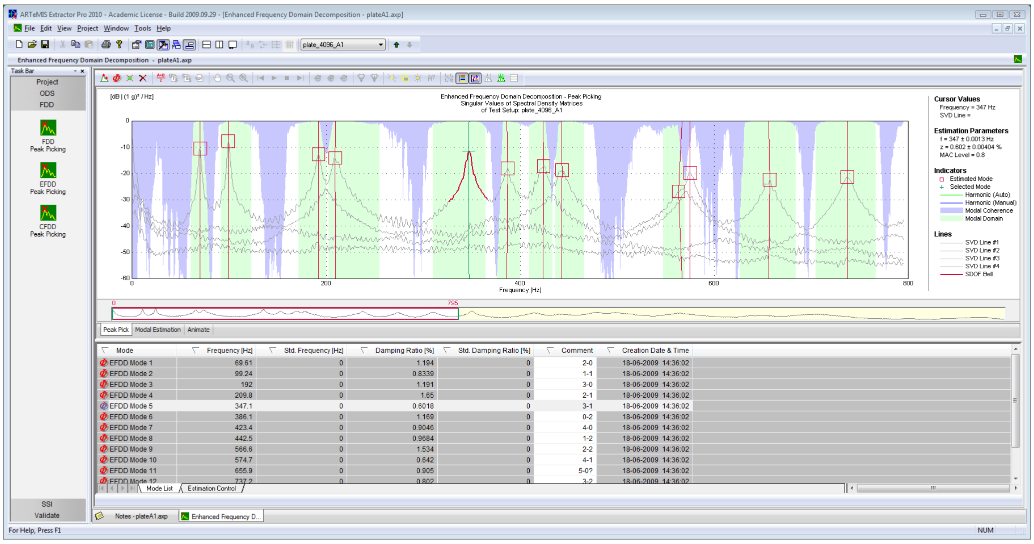

Figure 3.3: Enhanced Frequency Domain Decomposition peak picking editor of ARTeMIS Extractor. The modes are estimated by picking peaks in the singular value decomposition plot of spectral densities as described in Section 2.2. The lower part of the screenshot shows a list of already estimated structural modes.

only display the shape and amplitude values of the measured data but not process it further, there has not been any detailed investigation of the ODS feature during the work of this study thesis.

FDD In the Frequency Domain Decomposition task item, the three methods

- Basic FDD
- Enhanced FDD (EFDD)
- Curve-fit FDD (CFDD)

are implemented for the analysis of vibration data with the frequency domain methods as described in Section 2.2.

The graphical interface to all three methods are similar in nature. They include a peak picking editor (depicted in Figure 3.3), where the peaks of the SVD can be selected. Another tab provides parameters for the enhanced estimation in EFDD and CFDD. Identified modes can be animated in a 3-D view, where most of the mode shape illustrations in Chapter 4 and Appendix A, for example Figure 4.7, are taken from.

SSI The graphical interface for the Stochastic Subspace Identification method as summarized in Section 2.3 can be found in the SSI task item. In front of a SVD plot from the frequency domain estimation, a stabilization diagram for increasing model orders (see Section 2.3.7) is employed for the identification of structural modes. All three implemented SSI methods

- Unweighted Principal Component (SSI-UPC)
- Principal Component (SSI-PC)
- Canonical Variate Analysis (SSI-CVA)

share the same type of graphical interface as shown in Figure 3.4.

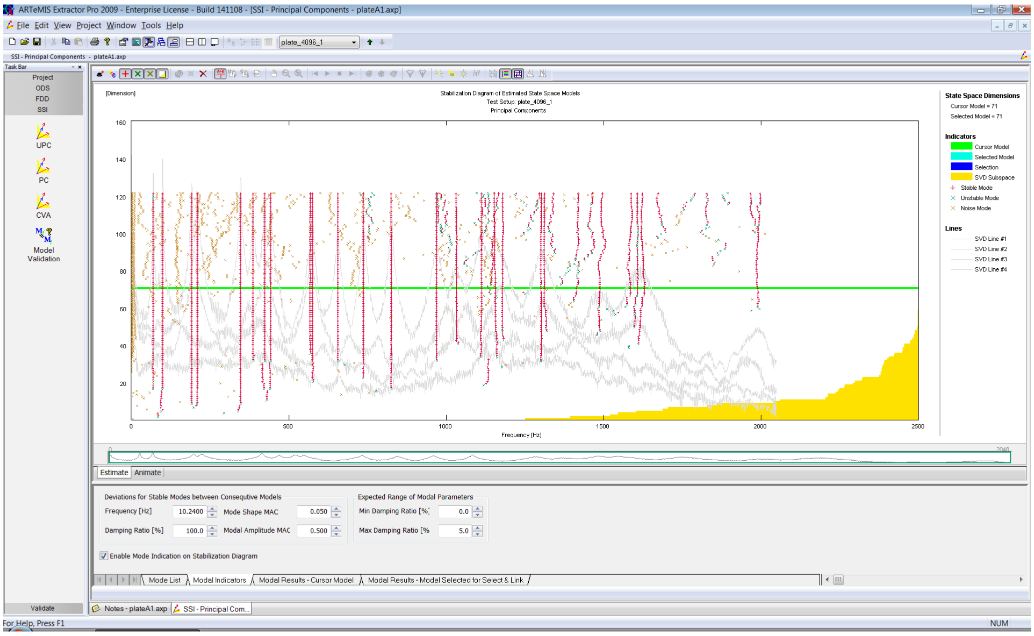

Figure 3.4: Stochastic Subspace Identification window of ARTeMIS Extractor. The screenshot shows the stabilization diagram as described in Section 2.3.7. The parameters of the estimation process can be adjusted with the controls shown on the lower tab of the screenshot.

Once a modal model is identified by the employment of one of the SSI algorithms, the quality and accuracy of that model can be explored by the SSI model validation feature. It provides overlays of the spectrum of measurement data with a synthesized spectrum from the identified modal model. Magnitude and phase angle of all auto- and cross-spectra can be compared to the synthetic version as well as prediction errors of magnitude and signal correlation.

Validate As mentioned in Section 2.6, the best way to validate data is to use as much different techniques of the two major method classes as possible and compare the identified models with regard to frequency, damping and mode shapes.

The Validate/Mode Comparison feature of ARTeMIS is intended to support exactly that process. Mode shapes of different identification sources can be animated in parallel or overlaid to each other. Also, the comparison of mode shapes using the *Modal Assurance Criterion (MAC)* (see Section 2.2.2 and [1]) is available by a 3-D bar graph of the MAC matrix as illustrated in Figure 3.5. A tabular representation of the MAC as well as numeric calculations such as phase angle differences are available, too.

Modes which are to be compared are not just limited to the identified ones within the current analysis project but can also be imported from other sources, e.g. from different analysis projects or suitably prepared mode data originating from FEM analysis.

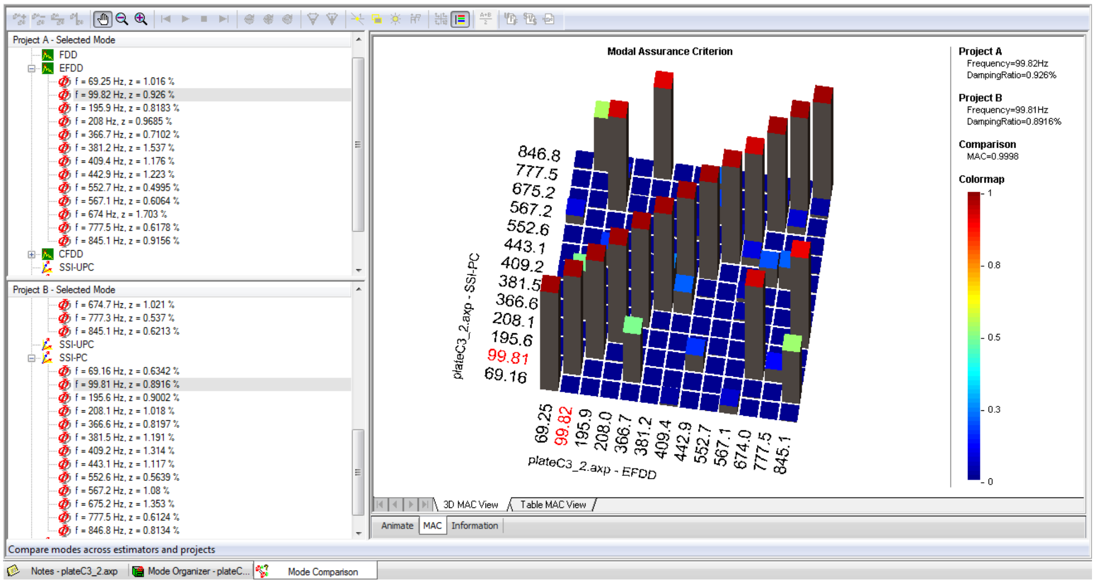

Figure 3.5: Three dimensional Modal Assurance Criterion matrix bar graph in the validation window of ARTeMIS Extractor. The red and outstanding values at the diagonal show that the two compared methods in the screenshot – Stochastic Subspace Identification with the Principal Components method and Enhanced Frequency Domain Decomposition – yielded the same mode shapes. No mode is missing or extra in either of the employed methods. Additional bars off the diagonal indicate that certain mode shapes look very similar with the given instrumentation set.

4 Preliminary Experiment: Aluminium Plate

For getting familiar with the employed software and identification techniques, a preliminary experiment has been set up. The simple geometry of a rectangular aluminium plate allows to compare estimation results to a priori knowledge of expected modal parameters such as mode shapes. Additionally, a numerical modal analysis with finite elements can be performed without much effort, and thus, the proper usage of the operational modal analysis technique is easy to verify. In contrast, if a complex structure such as the SOFIA Telescope Assembly had been the first object to be analyzed, confidence in the correct analyzing process would have been low.

4.1 Experimental Setup

The experiment consists of a rectangular plate made of aluminium which is equipped with a set of accelerometers. The dimensions of the plate are 415 mm × 178 mm with a thickness of 2.6 mm.

In order to obtain pure plate modes, the aluminium plate is suspended by rubber lines on two of its vertices. This isolates the plate modes from suspension modes due to the significant difference in stiffness. In terms of dynamic behavior the plate can be considered to be without any mounting or as “free”.

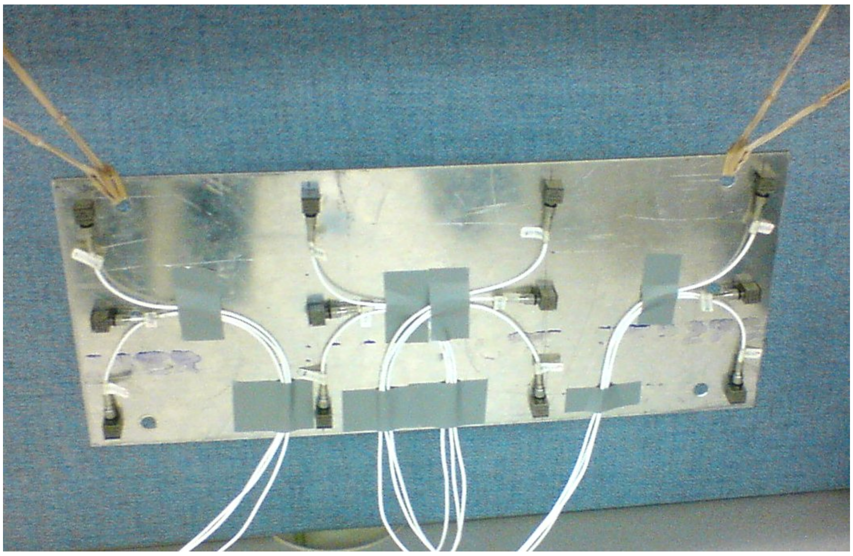

Figure 4.1: The measured structure of the experiment: A rectangular aluminium plate suspended with rubber lines. The pictures shows the plate with the so called instrumentation sensor setup "A". 12 accelerometers have been applied to the plate in a regular pattern. The sensor cables are fixed to the plate with adhesive tape.

In order to evaluate the multi test setup feature of the ARTeMIS software, three setups of sensor placements have been applied to the plate. While keeping 4 sensors at the corners of the plate as reference channels, the rest of the accelerometers were moved with the objective to obtain a better resolution of mode shapes when sensor locations from all test setups are merged into a combined analysis. Figure 4.1 shows a picture of the plate with the first

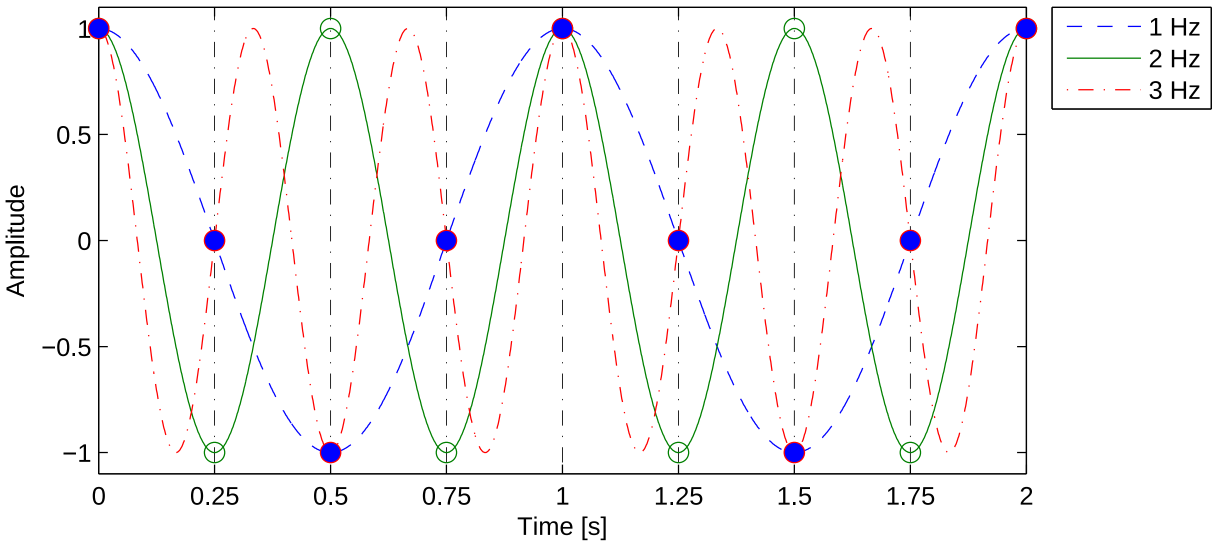

Figure 4.2: Illustration of aliasing. Three signals are sampled with a sampling frequency of 4 Hz. The circles represent the samples taken by the acquisition system at the sampling points. While the 1 and 2 Hz signal could be reconstructed later on, the 3 Hz signal is above the Nyquist frequency of 2 Hz. It yields the same samples as the 1 Hz signal and can therefore not be distinguished from the latter one.

sensor setup, named “Setup A”. For an illustration of setup layouts, see Section A.1. Setups A and B consists of 12 accelerometers, whereas Setup C uses 13 channels. The sensors were *Brüel& Kjær Deltatron 4507 B 005* accelerometers with a measurement range of ± 7 g and measured the “z”-Direction out of plane to obtain plate modes. Membrane modes with in-plane motion are not covered by the experimental setup.

4.2 Data Acquisition System

Measurements were taken by a data acquisition system (DAQ) built from hardware by National Instruments and using National Instruments’ LabVIEW software.

The sensors were connected to *NI PXI-4472B* device cards mounted into a *NI PXI 1045* chassis which was connected via fiber cable to a PCI card of an ordinary PC workstation running Windows 2000.

Programs in LabVIEW are called “virtual instruments” (VI). Such a virtual instrument has been programmed in order to configure the hardware, trigger data acquisition, process read data samples and export them into ASCII files in Universal File Format (UFF). The virtual instrument is partially based on a previous VI written by Ulrich Lampater, who used it in the work for his diploma thesis [22].

The DAQ employs some fixed signal processing filters which need to be addressed when taking measurements. The hardware does actually not sample input channels with the specified sample rate f_s but samples it with 128 times the specified sample rate. This is to prevent aliasing effects [25]. A sampled data set can only represent a limited bandwidth of the input signal. It can only distinguish signal components with a maximum frequency of $f_{Ny} = f_s/2$, called the Nyquist frequency. If the analog input signal contains frequency components higher than the Nyquist frequency, the sampler modulates those frequency components back into the base band from 0 Hz to $f_s/2$. This is called *aliasing*.

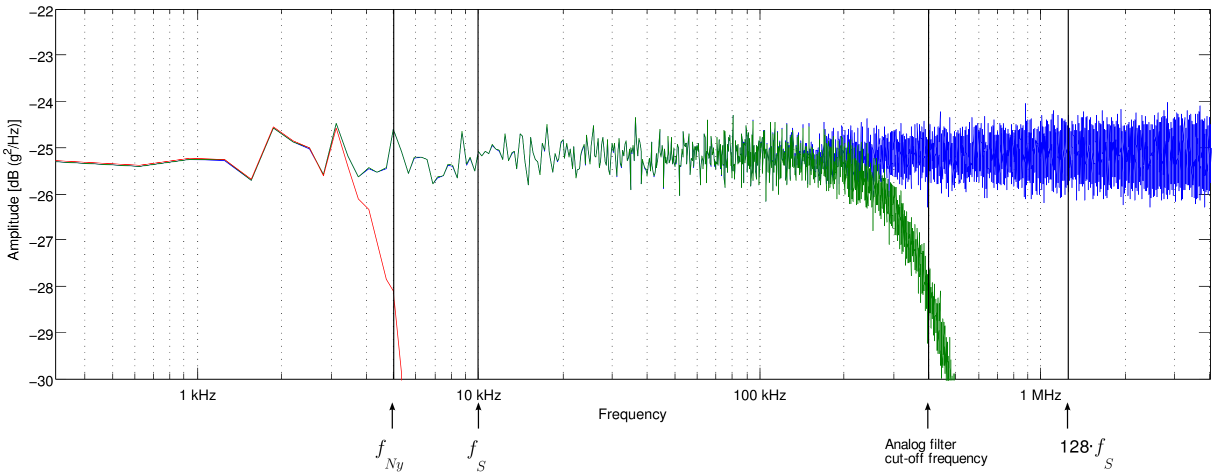

Figure 4.3: Anti-aliasing treatment for a wide banded noise signal (blue). First, an analog filter attenuates signal components above 400 kHz. The resulting signal (green) is again filtered by a digital filter that removes all spectral components above the desired Nyquist frequency (f_{Ny}, here 5 kHz) in order to prevent aliasing, yielding the red signal. Without the analog filter, the digital filter would not be able to remove a portion of the blue input signal around $128 \cdot f_s$. Note: This figure has been created by software tools for qualitative illustration purposes only. It does not reflect the quantitative attenuation and alias rejection of the employed hardware accurately.

Figure 4.2 shows three signals of 1 Hz, 2 Hz and 3 Hz, sampled with a sampling rate of $f_s = 4$ Hz. The Nyquist frequency is 2 Hz, so the green solid curve can still be recognized correctly, but the 3 Hz signal can not be distinguished from the 1 Hz signal. They share the same sampling points. In a real experiment, the measurement signal coming from the transducers usually does not consist of a clean sinusoid like in Figure 4.2 but has components over a wide range of the frequency spectrum. If the signal that arrives at the sampler would contain components that lie above the Nyquist frequency, then the energy of these components would be added to the signal components inside the Nyquist band causing severe distortions of the signal.

For “anti-aliasing”, the signal is oversampled by the DAQ hardware and analog and digital filters are directly applied in hardware before down-sampling the data to the desired sampling rate. Every channel has a built-in analog low-pass filter with a fixed cutoff frequency of 400 kHz. In the sampler, a digital filter removes all frequency components above the Nyquist frequency $f_s/2$, but it cannot remove components that lie within $f_s/2$ of multiples of the oversampling rate, because it cannot distinguish them from the base band due to the same reasons as aliasing occurs.

So the purpose of the analog filter before the sampler is that such components are not passed to the digital filter. Therefore, the oversampling rate has to be high enough so that the lowest frequency, which the digital filter can not filter out, is not within the passband of the analog filter. Since the cutoff frequency of the analog filter is fixed to 400 kHz, the minimum sampling rate would be:

$$128 f_s - \frac{f_s}{2} > 400\,\mathrm{kHz} \tag{4.1}$$

$$f_s > \frac{400\,\mathrm{kHz}}{127.5} \tag{4.2}$$

$$f_s > 3138\,\mathrm{Hz} \tag{4.3}$$

But since the applied analog filter has a rather slow roll-off, an additional safety margin should be added to the minimum rate.

Figure 4.3 shows a wide banded noise signal (blue) that is to be sampled with a sampling frequency of $f_s = 10\,\mathrm{kHz}$. The Nyquist frequency f_{Ny} is 5 kHz so all signal components above that should be removed before sampling. The green plot shows the signal after it has passed the analog low-pass filter. The energy of the signal at the oversampling frequency and multiples thereof is attenuated before the digital filter removes the remaining components. The red line is the remaining signal. Without the analog filter, the digital filter would not be able to remove a portion of the blue input signal around $128 \cdot f_s$.

4.3 Test procedure

For measurements of the aluminium plate vibration, a sampling rate of $f_s = 4096$ samples/s was used. The Nyquist frequency was 2048 Hz and well above the intended frequency range of 1000 Hz for modal parameter extraction. The duration of the measurements was 30 s. So a total of 122880 data points per channel has been acquired. As a rule of thumb, the lowest measured natural frequency should at least be represented in the data with 1000 cycles. With the lowest structural mode being around 70 Hz, this was achieved with more than twice the number of required cycles.

After starting data recording, the vibration of the plate was excited by random tapping with fingertips and the tip of a pen. While strictly speaking this was not white noise, it can be considered stochastic enough for OMA algorithm purposes. Several measurements per test setup were conducted in order to experiment with different tapping techniques and level of excitation. Due to the light weight of the plate, the excitation level was often too high yielding accelerations, which exceeded the nominal measurement range of the accelerometers for a very short time period at the beginning of the tapping impulses. By using the rubber end of a pencil, some energy from higher frequency bands was attenuated to overcome this overloading, but a comparison of resulting spectra showed no significant effect on overall signal qualities.

At the end of acquisition, the data was written to Universal File Format (UFF) text files and transferred to the analysis laptop where the ARTeMIS suite is installed.

4.4 Analysis of Data

Prior to importing actual measurement samples, the geometry of the plate along with sensor locations has been defined in ARTeMIS Testor. Several measurement files have been imported into the project and channels have been assigned to geometry nodes.

Merged data – geometry and measurement information – has been exported into binary files for further analyzing in ARTeMIS Extractor. Although it would have been possible to use the original UFF text data, Extractor turned out to be more stable while dealing with binary files. As a positive side-effect, the file sizes of binary files are smaller and the processing performance of the software is higher.

All available identification techniques in ARTeMIS Extractor have been employed to extract modal parameters in order to get familiar with the software and to evaluate application fields. The three test setups with different sensor locations have been analyzed in individual projects as well as in a multi-test setup project. The frequency resolution for the Fourier transform and – consequently for the Singular Value Decomposition (SVD) plots – was 1 Hz between the frequency lines.

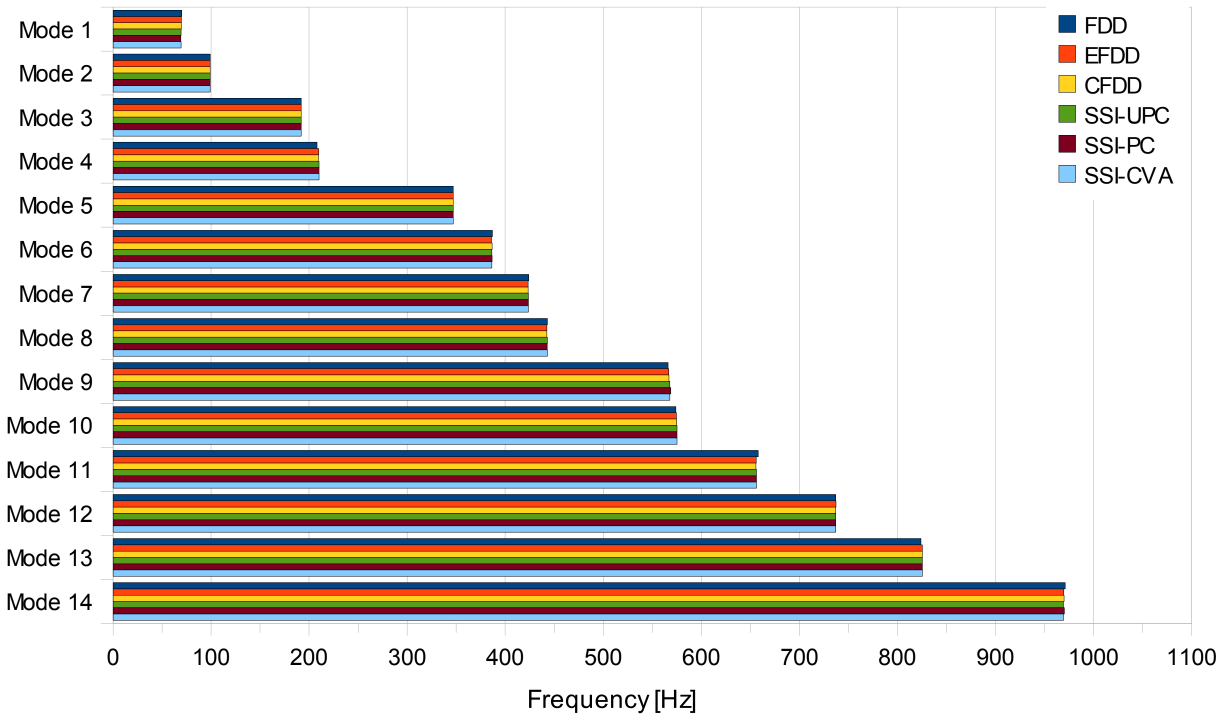

Figure 4.4: Identified frequencies for sensor setup A, comparing all available estimation methods in ARTeMIS Extractor. The variation of estimated frequencies among different techniques is very low.

4.4.1 Individual Sensor Setups

Setup layout, SVD plots, detailed tabular data of identified modal parameters and mode shape illustrations can be found in Appendix A. In each sensor setup, 14 to 15 modes have been identified inside the frequency band of 0 to 1000 Hz.

Natural frequencies Natural frequencies are recognized very consistently among the different techniques. Figure 4.4 illustrates the estimates for sensor setup A. The fact that the difference of bar lengths in that diagram can barely be detected shows that the standard deviation of the estimates is usually less than one Hertz. As the frequency resolution used for the Fourier transform is only 1 Hz, the variation of the estimates can be considered close to optimal.

Damping ratios The estimates of the damping ratios show a more significant variation. This does not come unexpectedly, as estimating damping parameters is the most difficult part of modal identification. The advantages and disadvantages of different techniques have the most significant effect onto this parameter: If the Enhanced Frequency Domain Decomposition (EFDD) technique cannot create a high quality correlation function out of the selected frequency band, curve fitting a logarithmic decay yields a low quality damping ratio. That was the case in several modes. Similarly, the Curve-fit FDD (CFDD) estimation algorithm had difficulties to fit a spectral bell for close modes and modes that are not well excited.

As Figure 4.5 illustrates, the damping ratios estimated by EFDD are typically higher than with the other techniques and the CFDD estimations are typically lighter. Leakage as mentioned in Section 2.2.3 is likely to play a role in this. While the EFDD algorithm has no countermeasure for the leakage effect and thus yields an overestimation, the CFDD curve fits seem to be too narrow and overcompensate the leakage effect.

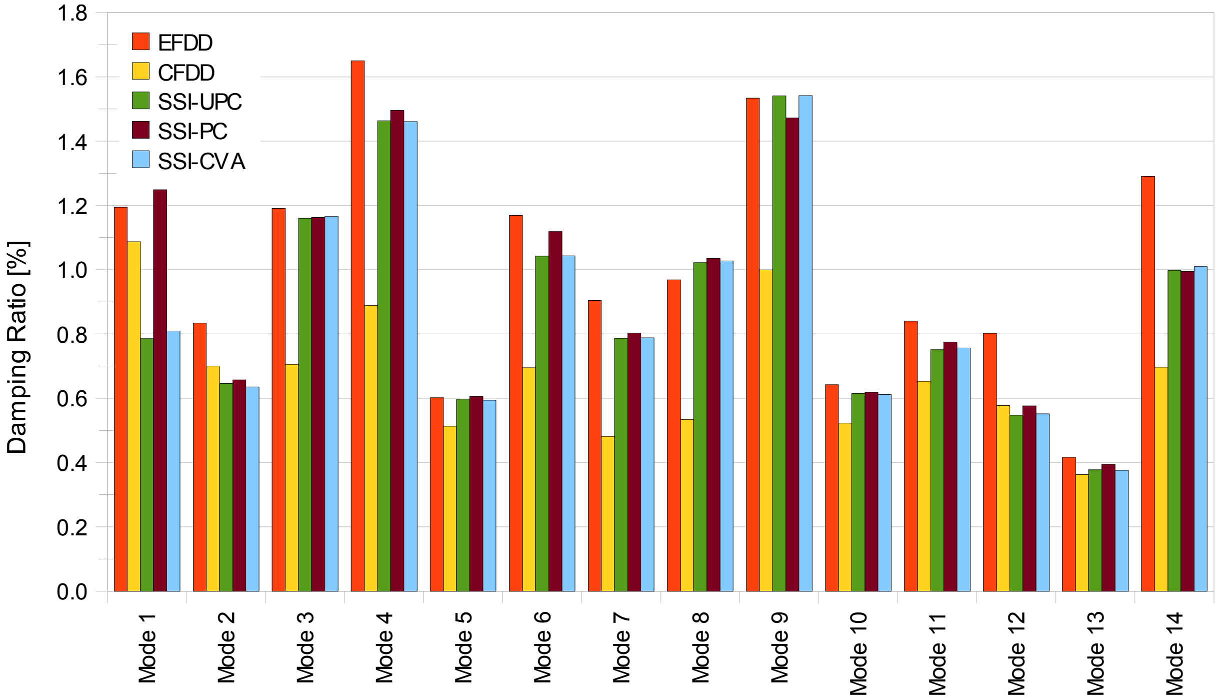

Figure 4.5: Identified damping ratios for sensor setup A. A tendency of overestimation of the Enhanced Frequency Domain Decomposition method can be recognized as well as the tendency of underestimation of damping ratios for the Curve-fit Frequency Domain Decomposition method.

Estimated damping ratios vary not only across the employed identification algorithms. They also vary significantly across different modes, and even for the same mode in different measurement setups. Theory would not predict that for an isotropic plate. Reasons for a divergence from theory presumably are that the sensors, connector lines, and the adhesive tape for fixation contribute significantly to the structural damping. These are positioned on plate locations that have high amplitudes for certain modes and low amplitudes for other modes, because they sit on or close to a modal line of the latter modes. Their influence on damping would vary from mode to mode. Similarly, when sensors, cables and adhesive tape are relocated for another instrumentation setup, the influence on damping for the same mode will change.

In a project where damping ratios are of immediate interest, e.g., for Finite Element (FE) model updating, a compromise among the different estimated parameters has to be found, taking into account which method worked best for a particular mode and which mode is significant for system performance. This example illustrates the importance of proper model validation and the need for user experience.

Mode shapes Although the presence of a large number of modes can be recognized, the identification of mode shapes is limited to to the spatial sensor placement resolution. While modes of lower order can be animated and recognized very well, the higher the order the less accurately the sensor motions can reflect the actual plate modes. In particular, the layout of setup A is limited to 3 nodal lines across the longer dimension and 2 nodal lines across the shorter dimension as maximum mode order. For example, Mode 10 at 575 Hz is a “4-1”-mode. In the multi-setup analysis as well as in the FEM analysis (see Section 4.4.2 and Section 4.5), Mode 10 has been identified to have 4 nodal lines across the longer dimension. An anlysis which takes just setup A into account however, displays Mode 10 as a mode with only 2 nodal lines across that dimension, just as the “2-1”-mode at 210 Hz (see Figure A.7(d) on page 85). This is also reflected in the high Modal Assurance Criterion (MAC) value when comparing these modes as shown in Figure 4.6.

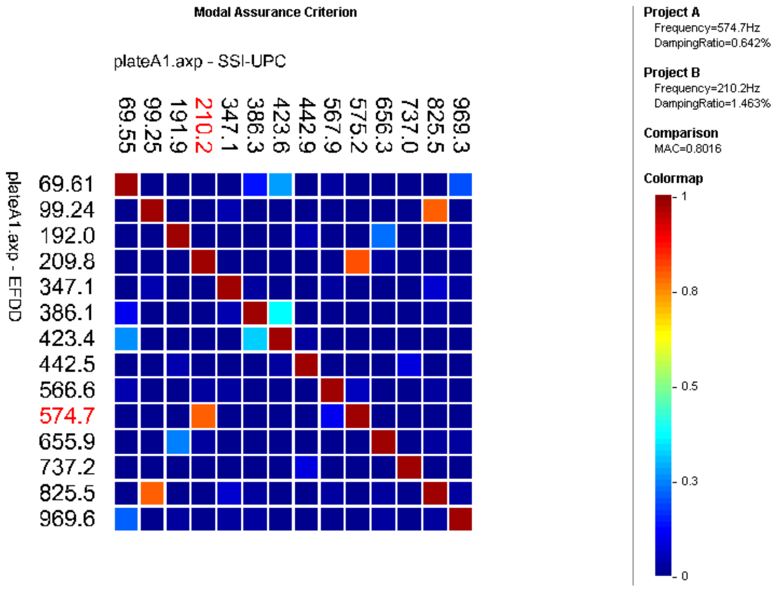

Figure 4.6: MAC matrix of mode shapes in Setup A estimated by the Enhanced Frequency Domain Decomposition method and the Stochastic Subspace Identification Unweighted Principal Components method. The red on the diagonal show that with both methods the same mode shapes were estimated. No mode is missing or extra in one of the employed methods. Additional high values off the diagonal show that certain mode shapes look very similar with the given instrumentation set, for example the shape of the mode at 210 Hz is barely distinguishable from the mode shape at 575 Hz.

One possibility to get the shapes of these higher order modes would be to use more sensors on the plate in order to get a better spatial resolution. Of course this is limited to the channel capacity of the data acquisition system and to the availability of sensor hardware. Additionally, the increased mass of the setup affects modal parameters.

4.4.2 Multi-Setup Analysis

Another possibility is to use the aforementioned multi-setup capability of the ARTeMIS software. By merging several different sensor layouts, the overall resolution is better than with single setups, but the total number of accelerometers remains the same, and there is no need for a bigger data acquisition system (although the DAQ system used in this particular case could handle up to 48 channels).

In the case of the aluminium plate with three test setups, the spatial resolution was indeed increased, and the "4-1"-mode as well as other higher order mode shapes can be illustrated quite well as shown in Figure 4.7. But another problem emerged: Due to the low mass of the small aluminium plate, the masses of sensors can not be neglected and affect the modal parameters significantly. While sensors were placed on nodal lines of a mode in one particular layout, they resided on heavily moving parts of the plate in another layout, thus increasing the modal mass of the mode significantly. This results in a shift of the natural frequency of that mode. Because the relocation of sensors affects individual modes differently, some modes even flipped their order frequency-wise. For example, the 9th mode in Setup A, the "2-2"-mode at 567 Hz, is the 10th mode in Setup B with a natural frequency of 599 Hz as well as in Setup C at 567 Hz, while the "4-1"-mode is number 10 in Setup A (575 Hz) but the 9th in Setup B (541 Hz) and Setup C (553 Hz). This behavior could be confirmed with a FEM analysis for all sensor layouts (see below).

For actual modal parameter identification, the multi-setup feature is thus limited to structures where accelerometer masses do not affect overall structure properties significantly. That would be the case for the SOFIA Telescope

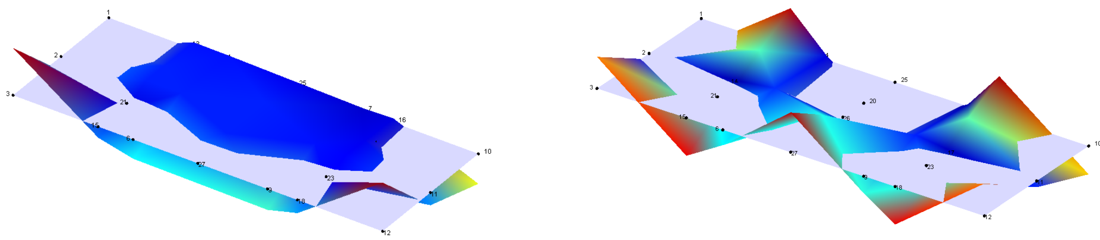

(a) Setup A

(b) Multi-Setup

Figure 4.7: Increase of spatial mode shape resolution of the “4-1”-mode with multi-setup analysis. Both pictures show the estimation of the same mode shape. While the instrumentation of sensor setup A cannot recognize the additional antinode on the centerline of the plate, a combination of several instrumentation setups reveals a better approximation of the actual mode shape.

Assembly because its overall mass exceeds the accelerometer masses by far. But since the sensor placement of the SOFIA in-flight accelerometer instrumentation is fixed, the multi-setup feature of ARTeMIS is not likely to be employed within the SOFIA project.

4.5 Comparison to FEM Analysis

For comparison, a numerical modal analysis with the Finite Element Method (FEM) has been performed. In a real project, this type of analysis is usually done before the experimental testing of real hardware. For structures which are more complex than a simple plate, one objective of a FEM analysis in the early stages of a project is to obtain basic knowledge about the dynamic behavior of the system. Based on that knowledge, the sensor locations for experimental instrumentation can be defined in such a way that the targeted modal vectors in the experiment meet the orthogonality requirements (as mentioned briefly in Section 2.2.2 with Equation (2.17)).

In case of the simple rectangular plate, the basic shapes of bending and torsional modes could already be anticipated without any FEM analysis before the experiment. The FEM analysis was performed after experimental testing and was done just for validation of the proper OMA algorithm and software use. In a real project, the comparison between FEM and experimental results is used for a validation of the the FE model and serves as basis for model updates.

The plate has been modeled using the graphical pre/postprocessing software *MSC Patran 2008* and *MSC Nastran 2007 R1* as actual FE solver back-end. The FE model consists of 1800 shell elements (QUAD4) and 12 respectively 13 concentrated mass elements (CONM2) representing the accelerometers. All three sensor setup layouts have been modeled and analyzed by placing the sensor masses in three different setups. Sensor cables and fixation tape have not been modeled as their contribution to the stiffness properties of the structure is considered to be negligible. The total mass of the model is 584 g.

Since the suspension by rubber lines in the experiment decouples plate modes from any suspension modes, the experiment can be considered to have free boundary conditions. Because of that, the FE model has been designed with free boundary conditions as well. This is called a free-free model. (The second “free” is due to the lack of load forces. In a numerical modal analysis no loading is applied to the model.)

The modal analysis solving sequence was configured to yield the first 20 eigenvalues of the system. Because of the free boundaries, thus the lack of any mounting, the first 6 eigenvalues formed the kinematic rigid body motions

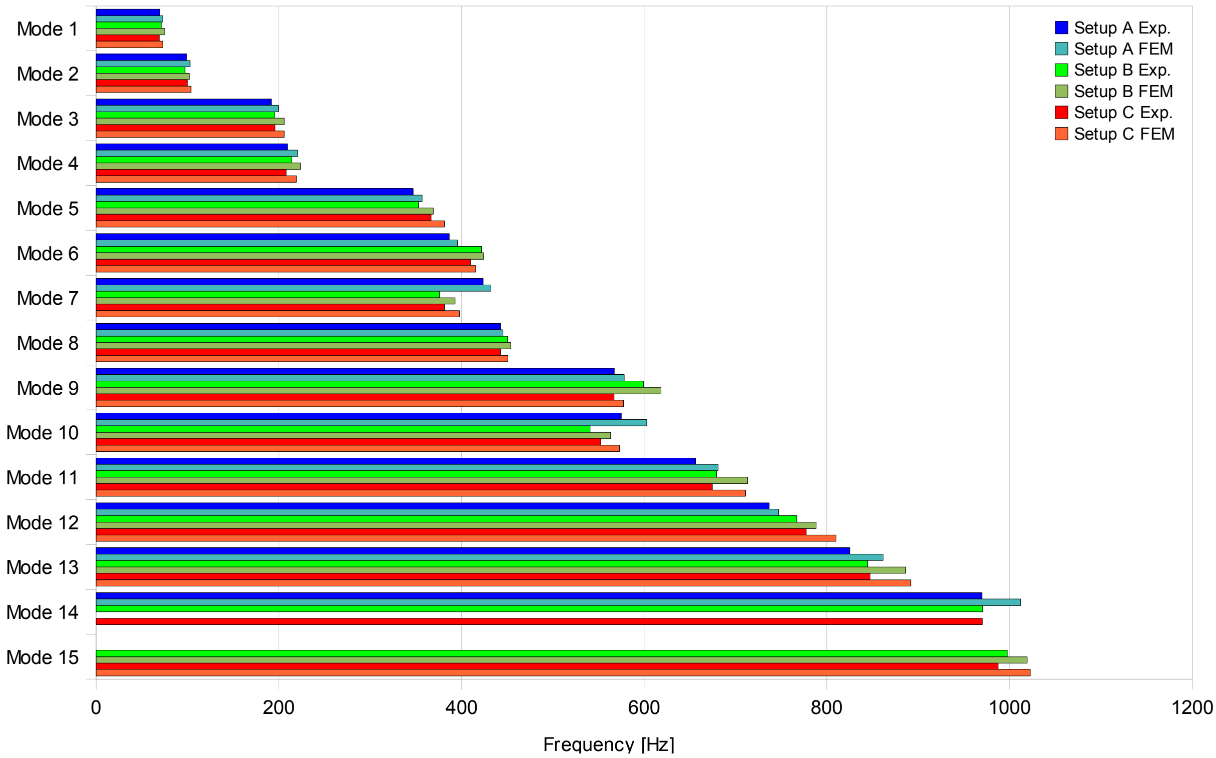

Figure 4.8: Comparison of experimental frequency estimates and Finite Element results. Besides showing a clear trend to slightly higher frequencies, the Finite Element calculations verify the results of the experiment. The variance of natural frequencies among the different test setups is also represented in the Finite Element results, even to the extend of shifted mode orders in the case of Mode 6 and 7 as well as for Mode 9 and 10. Since the Finite Element analysis just yielded 14 flexible modes and the 14th mode was the “6-0” in test setup A, but the “4-2” mode the test setups B an C, and because the “4-2” mode was not estimated as a mode below 1000 Hz in the experimental data for test setup A, the bars for these modes are not present in the diagram.

with a natural frequency of 0 Hz. The remaining 14 modes are the desired plate modes up to 1000 Hz. Tabular data of natural frequencies and mode shape illustrations can be found in Section A.4.

Depending on the sensor placement setup, the 20th eigenvalue yielded by the FE analysis is either mode 14, the “6-0” mode, or mode 15, the “4-2” mode. The respective other mode would be the 21st eigenvalue which was not calculated by the FE analysis. This is why there are values “missing” in Figure 4.8 and Section A.4.

A review of these modes as illustrated in Figure 4.8 shows that the experimental analysis identified all existing modes between 0 and 1000 Hz. Natural frequencies identified in OMA show a good correlation to those derived from the FEM analysis. For all calculated modes, the frequencies of the FEM modes are just a few Hz above the measured ones, indicating that either the FE model has too few mass or the stiffness of the model is too high.

The phenomenon of shifted modes due to different sensor placement could be verified with the FE analyzes for all three sensor layouts. The calculated frequency shifts are even more significant than measured. Trends and shifts of mode order are in line with experimental results.

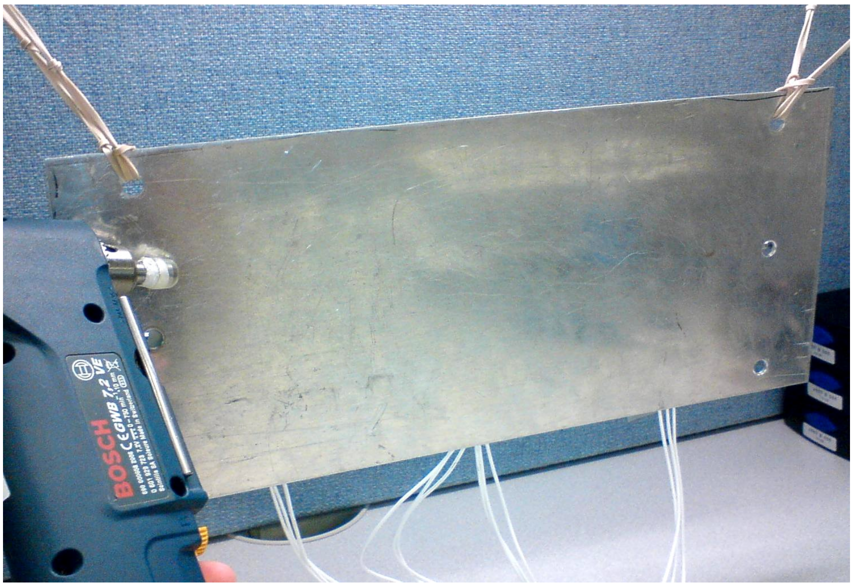

Figure 4.9: Harmonic excitation of the aluminium plate with an electric screwdriver. Sensors are on the back side for this experiment.

4.6 Harmonic Excitation

The experiment described up to this point was excited by quasi-stochastic finger and pen tip tapping. In a second step, the experiment was enhanced to address the detection and handling of harmonic excitation (see also Section 2.4). Various approaches have been applied, yielding different aspects of the desired data basis characteristics.

4.6.1 Electric Screwdriver

The first approach to simulate harmonic excitation employed an electric screwdriver with a nominal rotation of 750 revolutions per minute, which has been brought into contact with the plate as shown in Figure 4.9. Two different tips have been mounted into the chuck:

- A steel pin coated with a rubber cap
- The handle of a small manual screwdriver coated with adhesive tape

The coatings are needed to attenuate the excitation because otherwise excitation levels would exceed the measurement range of 7 g of the accelerometers. Additionally, stochastic loading by tapping with fingers has been applied to achieve good excitation of all structural modes.

Due to the nominal rotation of $750\,\mathrm{min}^{-1}$, peaks at harmonic excitation of 12.5 Hz and multiples of it are expected. Because of the low frequency of the harmonics the analyzed frequency range has been limited to 250 Hz and the frequency resolution of the Fourier transform has been set high (1024 frequency lines) to be able to resolve the narrow harmonic peaks. As shown in Figure 4.10 the narrow Fourier transform windows result in a somewhat noisy plot, but data quality is high enough to recognize the four wide peaks of the structural modes below 250 Hz as well as the narrow harmonic peaks on all displayed singular values.

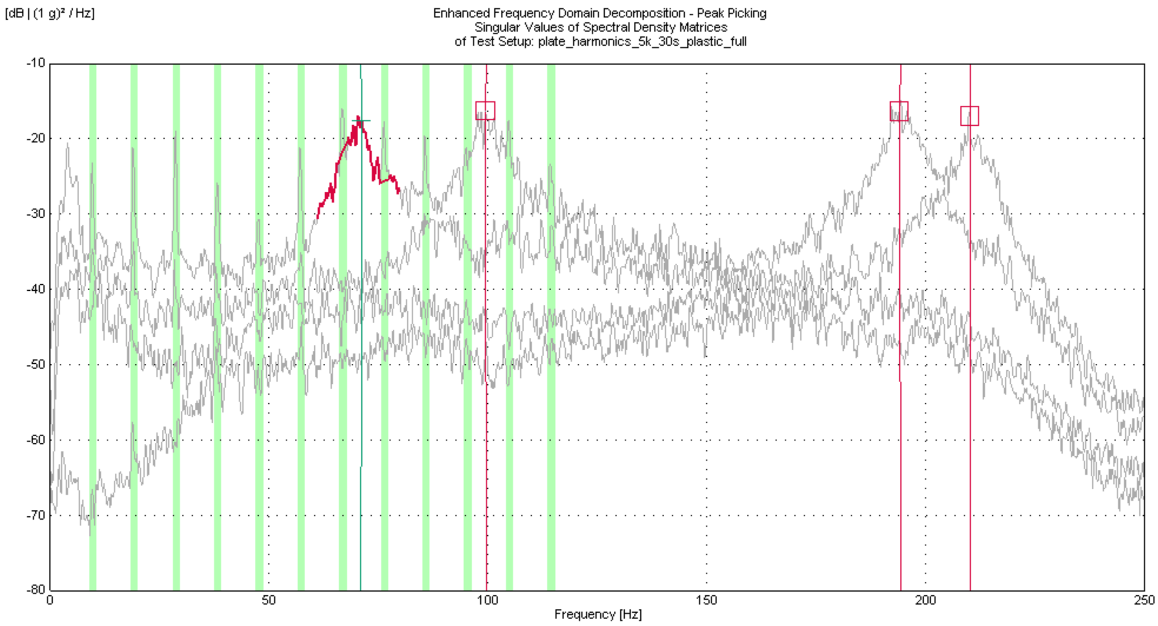

Figure 4.10: Singular value decomposition plot of spectral densities obtained through excitation with the electric screwdriver with rubber tip. The first 12 harmonics show significant peaks on the first singular values and are marked by green areas. The estimation algorithm for the Enhanced Frequency Domain Decomposition methods ignores these marked frequency bands and interpolates the singular values before calculating the correlation function.

The lowest harmonic peak is at 9.5 Hz, indicating that the electric screwdriver rotated slower than its nominal specification. The higher the order of the harmonics, the less its influence on overall response. Thus, only the first twelve harmonics have been marked manually. Automated harmonic detection as described in Section 2.4 did not detect all peaks, supposedly because of the high noise level. Figure 4.10 also shows how the EFDD algorithm interpolates linearly between the limits of a marked harmonic peak.

The estimated damping ratios for measurements with the rubber coated steel pin are significantly higher than those identified by the experiments with pure stochastic excitation or with the manual screwdriver handle and tape. This may be due to the continuous contact of the plate with the (moving) rubber surface of the pin tip, but no further investigation has been performed regarding this issue.

4.6.2 Heat Gun

Since the screwdriver approach yielded a very dense occurrence of harmonic peaks at low frequencies, where structural modes are even affected by more than one harmonic, a second approach with a heat gun was employed in order to get harmonics starting at a higher frequency. The idea was to simulate some sort of acoustic or aerodynamic excitation.

The heat gun was trialed as a source of harmonic, acoustic and aerodynamic loads in three different ways:

- Directing the air flow directly towards the plate
- Using the air flow to create a tone by blowing over an open bottle acting as a flute.
- Physical contact of the heat gun nozzle with the plate

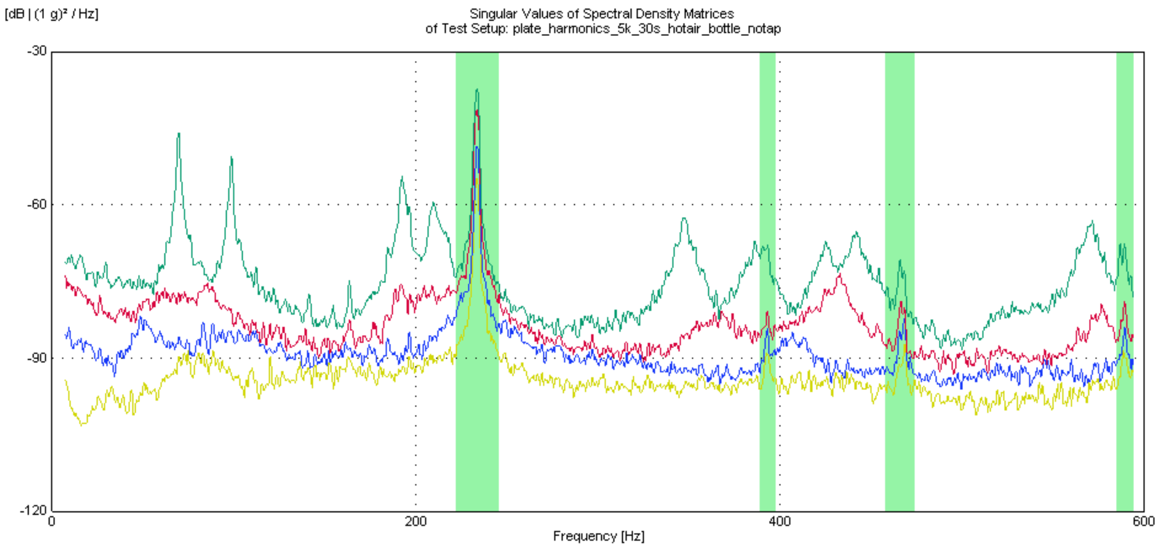

Figure 4.11: Singular value decomposition of spectral densities obtained through excitation by a heat gun blowing over a bottle. There is a dominating harmonic at 233 Hz, affecting all singular value curves.

The heat selection control was always in the coolest position, labeled 120 °F, so temperature issues would not be a threat to sensor equipment. The tone created by the "bottle flute" could be tuned by varying the water level inside the bottle. As one can imagine, the excitation level of the airflow cases with and without extra bottle tone was relatively low (below 1 g total acceleration). Although the harmonic components are very dominant within the weak response signals in these cases, the structural modes are excited and still can be identified.

Figure 4.11 shows the SVD plot of the experiment with the bottle as excitation device. At 233 Hz, all plotted singular values have a strong peak, indicating that excitation at that frequency was much higher than on the rest of the spectrum.

By additional quasi-stochastic tapping, the domination of the harmonic vanished almost completely as indicated in Figure 4.12. In that case, the harmonic peak on the first singular value is so weak, the linear interpolation employed by the EFDD algorithm yields even higher singular values for weighting the mode shape estimation. That is because the linear secant produced by interpolation is actually higher than the curve of the SDOF bell including the small harmonic peak. In such a case it would be better not to mark the harmonic, because the weighting bias is not so severe with the harmonic than with the overzealous interpolation.

4.6.3 Lessons Learned

At least in the conducted experiments, the automatic harmonic detection did not work as well as advertised. The best way to exclude harmonic peaks from FDD estimation algorithms was to mark them manually by recognizing their narrow shape and occurrence in all displayed SVD curves. This is only possible in conjunction with the "Fast check" option of ARTeMIS Extractor. "Extended kurtosis check" does not allow manual manipulation afterwards.

The experiments with dominating frequency peaks due to harmonic excitation revealed a major disadvantage of the Stochastic Subspace Identification algorithms. In FDD, harmonic peaks can be marked and eliminated by interpolation of singular values, so that information in those frequency bands is still available for mode shape identification. SSI however works in time domain and no algorithm is available to eliminate the influence of

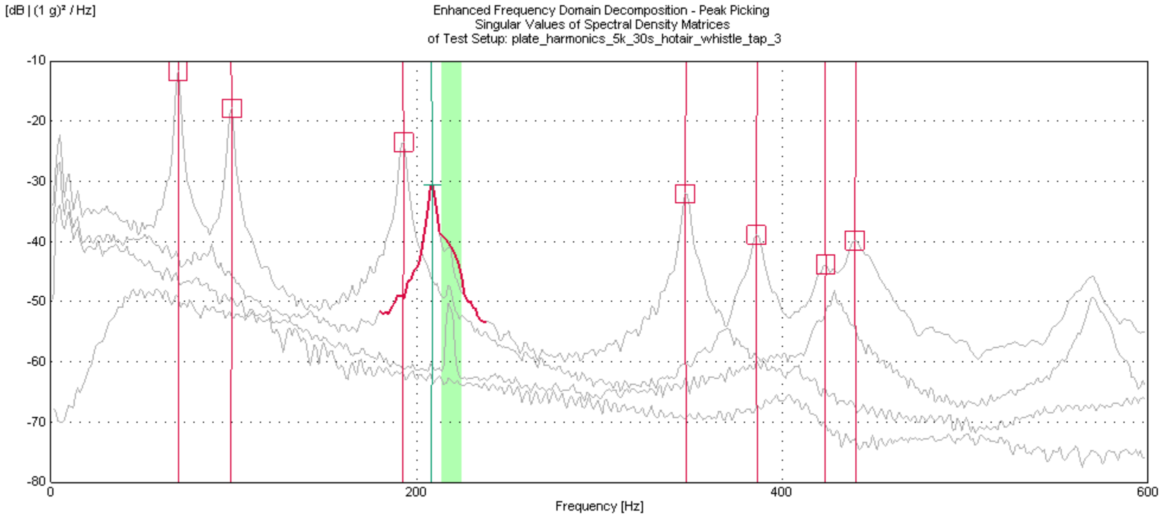

Figure 4.12: Singular value decomposition of spectral densities obtained through excitation by a heat gun blowing over a bottle and additional stochastic load through finger tipping. The domination of the harmonic at 233 Hz compared to Figure 4.11 is diminished to the extend that the harmonic elimination algorithm through linear interpolation is counter productive. Due to the logarithmic scale, the linear secant is plotted as a concave curve. That curve lies significantly over the actual spectral bell produced by the structural mode.

harmonic components. Instead, the estimated SSI model has to fit data that includes the harmonics to the expense of structural modes.

Figure 4.13 illustrates the problem containing two auto PSD plots of the same channel obtained from the "bottle flute"-experiment. In Figure 4.13(a), the SSI algorithm created 3 close modes for fitting the dominant harmonic at 233 Hz. This started with a state space dimension long before introducing modes to fit weaker structural modes when increasing the state space dimension in the stabilization diagram. In Figure 4.13(b) that harmonic was filtered away by a narrow band-stop filter. Now, the SSI algorithm estimated structural modes sufficiently with a much lower state space dimension. However, the band-stop filter approach is only suitable when the harmonic frequency is not in the direct vicinity of a structural mode, because the filter would attenuate also that mode and information about it would be lost.

4.7 Conclusions

The preparation, execution and analysis of the aluminium plate experiment was of great benefit for the understanding of experimental methods in vibration analysis, particularly the OMA method. Although there might be no further scientific interest in the modal properties of a simple aluminium plate, the experiment served as pre-cursor to the actual analyses of SOFIA instrumentation data during flights and preparatory test campaigns.

Among general familiarization with the ARTeMIS software, the analysis of the aluminium plate experiment brought attention to some important aspects, when it comes to applying the software and its different algorithms such as:

- The estimation of damping ratios is biased depending on the version of the FDD algorithm – see Section 4.4.1.
- Some limitations of the SSI algorithm with dominant harmonics became apparent – see Section 4.6.3.

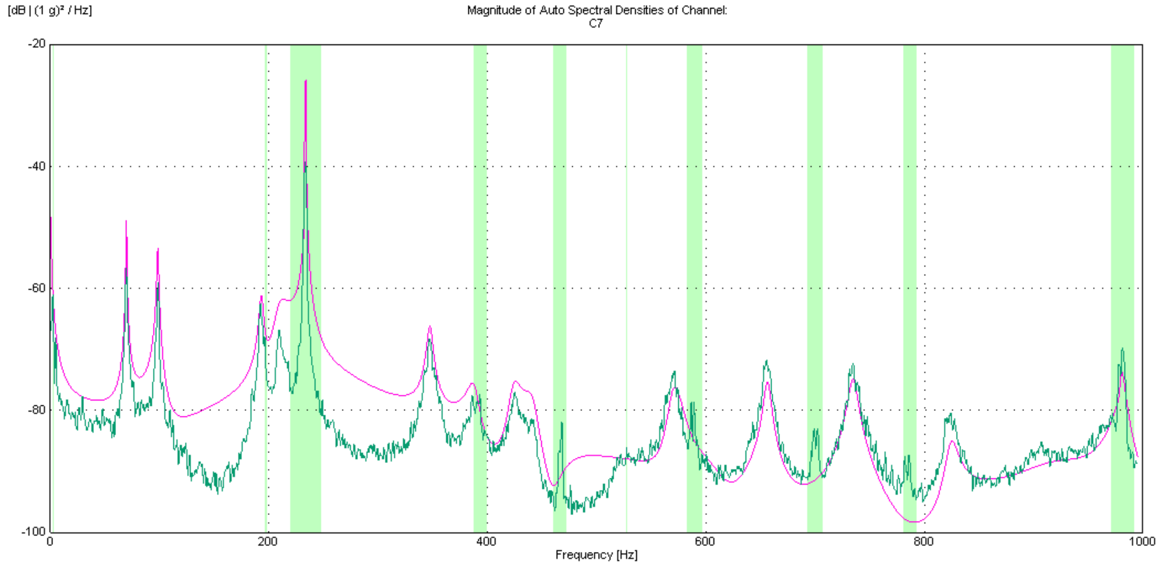

(a) Power spectral density of a measured accelerometer channel (green) and synthesized power spectral density for the same channel (magenta) obtained by an estimated model through Stochastic Subspace Identification. The harmonic at 233 Hz biases the estimation algorithm, so that the rest of the signal is not approximated accurately.

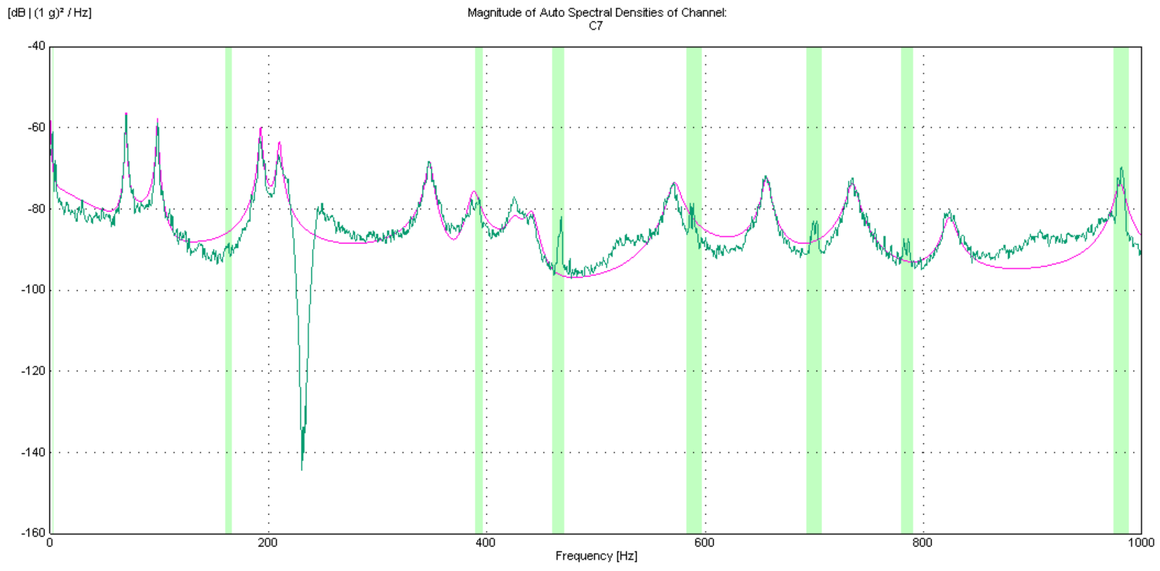

(b) After eliminating the dominating harmonic at 233 Hz through the use of a band-stop filter, the approximation of the measured signal by the model is improved significantly.

Figure 4.13: Influence of a dominating harmonic on the estimated model accuracy.

- Bugs and shortcomings of ARTeMIS Extractor were detected and some of them were solved by Structural Vibration Solutions in cooperation with the author and the DSI – see Chapter 3.

Additionally, even though the experimental setup was rather simple, the importance of many aspects of data acquisition and signal processing became apparent. Knowledge about such things as the Nyquist-Shannon sampling theorem, aliasing and its prevention, and signal filtering is crucial for every experiment involving sensor measurements. Thus, the aluminium plate experiment definitely was worth the effort spent.

5 SOFIA Test Data

5.1 Flight and Testing Schedule, Objective of OMA applied to SOFIA

The initial goal pursued for the work of this study thesis was to apply the methods of Operational Modal Analysis (OMA) to SOFIA flight test data, which would be obtained during test flights. At the time, when the initial scope of the thesis work was planned and negotiated, the SOFIA project schedule still contained plans for the first open door flights to happen in March 2009. However, delays in the program schedule caused the open door flights to be postponed in a way that analyzing open door flight data slipped beyond the available time frame for this study thesis.

Thus the focus of this study thesis had to be shifted towards theoretical aspects, as described in Chapter 2. Also, extended effort has been put into the aluminium plate experiment as presented in Chapter 4. Nevertheless, some preparatory work towards a future operational modal analysis of the SOFIA Telescope Assembly (TA) still was accomplished without having access to in-flight measurement data.

Since the SOFIA project is in a rather advanced state of development, the information available about the dynamic properties of the TA structure is already quite extensive. This information was obtained during the design process by the means of analytical methods such as the Finite Element Method (FEM), and later on during development for example by the Modal Survey Test (MST) [3] as already mentioned in the introduction (Chapter 1). The objective of an operational modal analysis of SOFIA during flight conditions will be to refine this previously obtained knowledge, especially under the significantly diverging environment compared to ground-based test campaigns such as the MST.

5.2 Instrumentation and Modal Ranking

A complex structure like the SOFIA TA has a significant number of modes within a certain frequency range. In other words, the SOFIA TA is modally dense. It has more than 100 modes with natural frequencies under 100 Hz. Although the MST allowed for the use of several hundred sensor channels, even within that campaign the sensors had to be positioned at strategically well defined locations in order to be able to observe and identify modes [1] that have been classified as important, based on prior FEM analyzes. For flight test campaigns, the situation is even more critical. The bandwidth for TA vibration data that can be recorded during a mission is limited and must be shared with other data sensors, which are monitoring other systems of the telescope as well as the aircraft.

Because of that, the number of available sensor channels during the operational test phase is limited. Accordingly, the modes that are still to be identified had to be chosen from a prioritized list. The positioning of sensor locations and directions had to be specified in order to meet the orthogonality requirements to be able to identify those selected modes during the modal analysis.

Since one of the major objectives for obtaining modal information is to improve the pointing stability and image quality of the SOFIA Telescope, the measure to evaluate the importance of a mode is its influence on image jitter.

[1] also compare to the concept of observability as introduced in Section 2.3.5

Thus, a ranking of modes based on that measure has been developed [23]. Based on that ranking, an instrumentation set has been specified, which meets the limited bandwidth requirement and still enables a discrimination of the targeted modes. This instrumentation consists of three sets of acceleration sensors employed within the cavity:

- Optical path aensors
- Structural monitoring sensors
- Real-time monitoring sensors

5.2.1 Optical Path Sensors

The first set of sensors are accelerometers measuring the motion of optical path components of the telescope, such as the mirrors and sensors in the focal plane. These sensors are *Brüel&Kjær DeltaTron Accelerometer Type 4507 B 005*, the same type as those used in the aluminium plate experiment of Chapter 4. They have a nominal measuring range of $\pm 7\,\mathrm{g}$ and there are special temperature calibration curves available, which take the varying temperature of the cavity environment into account. These calibration curves have been calculated from measurement data obtained during a calibration test procedure at the NASA Ames Research Center in November 2008. An example of such a calibration curve is plotted in Figure 5.1.

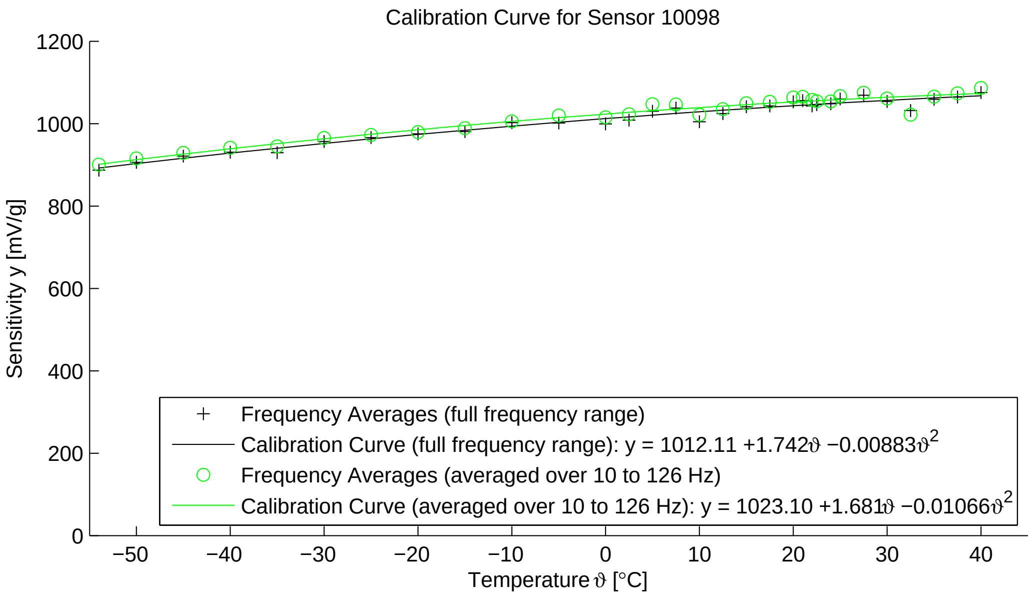

Figure 5.1: Calibration Curves of Optical Path Sensor AC1 (primary mirror)

A listing of sensor names, their location on the TA and the assignment to a SOFIA data stream (see Section 5.3.2) can be found in Table 5.1.

5.2.2 Structural Monitoring Sensors

The second set of vibration sensors are accelerometers of type *Endevco 7290D-10* and are mounted at specific locations over the telescope structure. These sensors have a nominal measuring range of $\pm 10\,\mathrm{g}$ and are DC coupled, which means they also measure the static component of the current acceleration, such as the gravitational force.

Table 5.1: Optical path accelerometers. See Section 5.2.1 for details

Sensor No.	Sensor ID	Position	Serial No.	Stream	Sample Rate [Hz]
AC1	AC8655	M1 backside fore	10098	5	1000
AC2	AC8657	M1 backside right	10097	5	1000
AC3	AC8659	M1 backside left	10149	5	1000
AC4	AC8661	M1 center v direction	10095	5	1000
AC5	AC8662	M1 center u direction	10096	5	1000
AC6	AC8666	SMM side fore	2154443	5	1000
AC7	AC8667	SMM side right	2154444	5	1000
AC8	AC8668	SMM side left	10079	5	1000
AC9	AC8669	SMM top v direction	2154445	5	1000
AC10	AC8670	SMM top u direction	2154446	5	1000
AC11	AC8663	Dichroic M3 aft	10092	5	1000
AC12	AC8664	Dichroic M3 right	10093	5	1000
AC13	AC8665	Dichroic M3 left	10094	5	1000
AC14y	AC8671	Focal Plane (Cabin)	10151	4	1000
AC14z	AC8672	Focal Plane (Cabin)	10152	4	1000

The set of structural monitoring accelerometers is listed in Table 5.2. The sensors listed in the table with a serial number starting with the letter A belong actually to the real-time monitoring sensor set (see below).

5.2.3 Real-Time Monitoring Accelerometers

Most of the sensors of the two instrumentation sets described above are recorded during flight missions and can be analyzed at the earliest one day after the completion of mission. In contrast, data from a limited set of sensor channels is transferred in real-time to the mission control room at the NASA Dryden Flight Research Center. This data is monitored by an engineer in the control room during the whole mission in order to evaluate the proper operation and structural integrity of the telescope.

Since the real-time monitoring sensors have a different purpose compared to the sensor sets described above, they need a different measurement range. Vibration levels during operation are expected to be rather low, und thus the sensors for the optical path and structural monitoring have a measurement range of ± 10 g. This range is intended to enable an adequate quantization resolution of the vibration levels expected during operational missions. However, the maximum allowed vibration level to retain structural integrity of the aircraft and the Telescope Assembly exceeds 10 g on some parts of the TA. Thus, in order to be able to monitor the full range of allowable vibration levels during a test mission, the real-time monitoring instrumentation set is equipped with *Endevco 7290D-100* accelerometers. These sensors have a measuring range of ± 100 g, and are located right next to the optical path accelerometers and at additional structurally important positions. A list of the sensor channels is presented in Table 5.3.

After the envelope expansion flights, where the aircraft will be successively brought into higher altitudes and at faster airspeeds in order to test and certify full operational airworthiness, the real-time monitoring accelerometers will be removed again. Those sensors which are placed at locations not already covered by the optical path accelerometers will be replaced by 10 g sensors, so that the structural monitoring sensor set (see above) remains complete, in order to retain the observability of the targeted structural modes for modal identifiaction purposes.

Table 5.2: Structural monitoring accelerometers. See Section 5.2.2 for details

Sensor No.	Sensor ID	Position	Serial No.	Stream	Sample Rate [Hz]
AC15x	AC8673	Headring aft Spider I/F	29969	5	500
AC15z	AC8674	Headring aft Spider I/F	29985	5	500
AC16	AC8675	Headring right Spider I/F	30017	5	500
AC17	AC8676	Headring left Spider I/F	30039	5	500
AC18	AC8677	Headring right aft corner	30052	5	500
AC19	AC8678	Headring left aft corner	30053	5	500
AC20	AC8683	Aft Spider center	A026704	4	1000
AC21	AC8679	Right Spider center	A026686	4	1000
AC22	AC8681	Left Spider center	A026691	4	1000
AC23x	AC8685	PMA Baffle Plate I/F	30208	5	1000
AC23y	AC8686	PMA Baffle Plate I/F	30209	5	1000
AC23z	AC8687	PMA Baffle Plate I/F	A015357	4	1000
AC24	AC8689	PMA right aft corner	30210	5	1000
AC25	AC8698	PMA left aft corner	30092	5	500
AC26y	AC8699	PMA fore center	30206	5	500
AC26z	AC8700	PMA fore center	30207	5	500
AC27	AC8701	Tertiary Tower u direction	A015349	4	1000
AC28	AC8703	Tertiary Tower v direction	A015353	4	1000
AC29	AC8954	Balancer top right	30074	4	500
AC30	AC8955	Balancer top left	30085	4	500

Table 5.3: Real-time monitoring accelerometers. See Section 5.2.3 for details. AC42 through AC44 are reserved for the Sun Cover, which was not mounted yet and therefore not equipped with sensors at the time of the completion of this list.

Sensor No.	Sensor ID	Position	Serial No.	Stream	Sample Rate [Hz]
AC31	AC8953	Baffle Plate 2h looking fwd.	A026677	4	1000
AC32	AC8656	M1 backside fore	A015221	4	1000
AC33	AC8658	M1 backside right	A015240	4	1000
AC34	AC8660	M1 backside left	A015330	4	1000
AC35	AC8687	PMA Baffle Plate I/F	A015357	4	1000
AC36	AC8952	PMA starboard	A015343	4	1000
AC37	AC8679	Right Spider center	A026686	4	1000
AC38	AC8681	Left Spider center	A026691	4	1000
AC39	AC8683	Aft Spider center	A026704	4	1000
AC40	AC8701	Tertiary Tower u direction	A015349	4	1000
AC41	AC8703	Tertiary Tower v direction	A015353	4	1000
AC42	AC8956	Sun Cover		4	1000
AC43	AC8957	Sun Cover		4	1000
AC44	AC8958	Sun Cover		4	1000

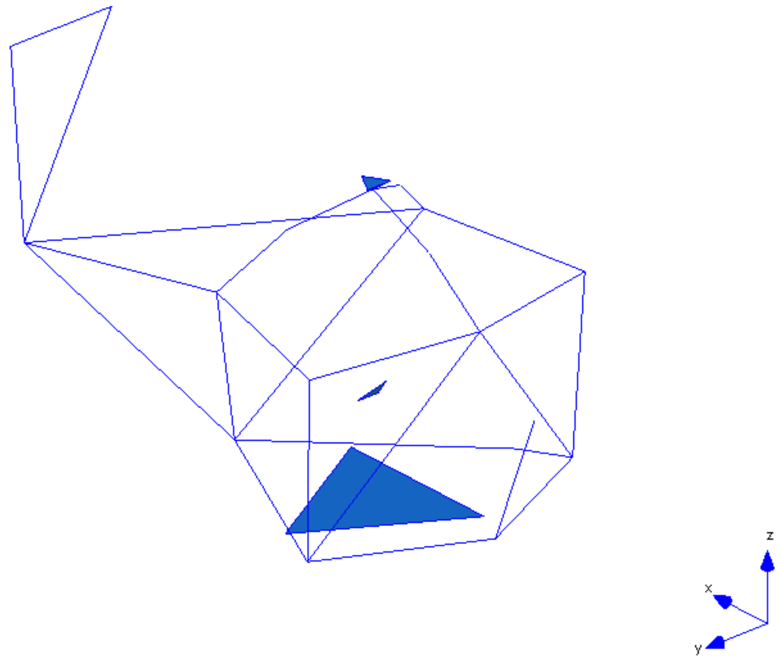

Figure 5.2: Geometrical representation of the SOFIA Telescope Assembly within ARTeMIS Extractor. The nodes of the model represent flight instrumentation sensor locations, which have been connected in order to resemble the metering structure. The sensor nodes on the primary, secondary and tertiary mirror serve as vertices for triangular surfaces representing the mirrors.

5.3 Data Acquisition

5.3.1 Geometry Import

In order to be able to animate mode shapes within *ARTeMIS Extractor*, the geometrical information of the instrumentation set as given in Section 5.2 needed to be specified in a format that is suitable as input for that software. This geometrical information includes the positions of the accelerometers on the TA structure as well as their direction of measurement.

Figure 5.2 is a screenshot of the undeformed TA geometry as rendered within *ARTeMIS Extractor*. The sensor locations, which are the nodes of the model, have been connected by lines, intended to represent the structure of the TA. The accelerometer nodes measuring the motion of the three optical mirrors form the vertices of triangular surfaces, which represent the mirrors.

The accelerometers only measure one direction per sensor. The identified mode shape can only reflect the component of a deflection of a node in which direction the sensor measures. In order to animate the three-dimensional motion of a mode, e.g., the rocking of the mirrors, the measurement of multiple sensors has to be combined. For example, the measured lateral motion, the x- and y-direction, by two sensors located on the backside of a mirror, is applied to all three nodes of that mirror which form the vertices of the triangular surfaces. At each of these nodes there is another sensor measuring the motion in z-direction. In the mode shape animations, this effects in a 3-dimensional motion of the triangular surfaces representing the mirrors. The task of combining multiple sensor signals is accomplished by user defined equations, governing the motion of a node depending on the measurement values of sensor channels other than the one already assigned to a node.

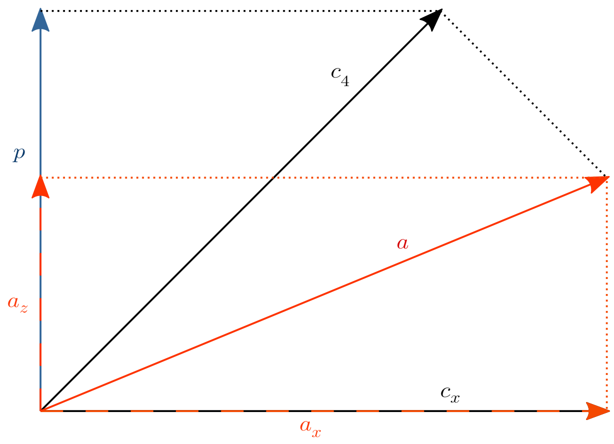

Figure 5.3: Illustration of transformation equations for tertiary mirror instrumentation. See text for details.

Suppose the three nodes which form the vertices of the triangular surface representing a mirror are named n_1, n_2 and n_3. The acceleration of those nodes in z-direction is measured by the sensor channels c_1, c_2 and c_3 respectively. Additionally, the sensor channels c_x and c_y measure the x- and y-direction of the mirror. The 3-dimensional motion of the three mirror nodes can now be described as follows:

$$\begin{bmatrix} a_x & a_y & a_z \end{bmatrix}_{n_1}^T = \begin{bmatrix} c_x & c_y & c_1 \end{bmatrix}^T \tag{5.1}$$
$$\begin{bmatrix} a_x & a_y & a_z \end{bmatrix}_{n_2}^T = \begin{bmatrix} c_x & c_y & c_2 \end{bmatrix}^T \tag{5.2}$$
$$\begin{bmatrix} a_x & a_y & a_z \end{bmatrix}_{n_3}^T = \begin{bmatrix} c_x & c_y & c_3 \end{bmatrix}^T \tag{5.3}$$

Similarly, such user defined equations have been used to implement a transformation of measurement coordinates for the sensors located at the tertiary mirror tower. Since the tertiary mirrors are tilted by 45° in order to deflect the optical beam into the Nasmyth tube, the out of plane sensors measure the acceleration in that 45° direction. The lateral motion of the tertiary mirror tower, however, is measured along the global x- and y-axis (U and V in the official *Telescope Assembly Reference Frame (TARF)*[2]). Thus, in order to animate the motion of a node n_4 of the tertiary mirror, the equation governing that motion is a bit more complicated:

$$\begin{bmatrix} a_x \\ a_y \\ a_z \end{bmatrix}_{n_4} = \begin{bmatrix} 1 & 0 & 0 \\ 0 & 1 & 0 \\ -1 & 0 & \sqrt{2} \end{bmatrix} \begin{bmatrix} c_x \\ c_y \\ c_4 \end{bmatrix} \tag{5.4}$$

where c_4 is the channel measuring the tertiary mirror out-of-plane acceleration at that node and c_x and c_y measure the lateral motion. In the equation as found in the SVS configuration file the coefficient before the node corresponding to c_4 is 2 instead of $\sqrt{2}$, because the parameter p used as input for the equation is actually the global z component of the channel c_4, i.e. $p = \frac{c_4}{\sqrt{2}}$ and $a_z = 2p - c_x = \sqrt{2}c_4 - c_x$. Figure 5.3 illustrates the transformation. The resulting vector is given in global coordinates.

All of the instrumentation and setup information has been collected in MATLAB data files. A graphical tool, the *CSV to SVS Conversion Tool* has been developed, which incorporates these setup files and exports the information to SVS configuration files along with measurement data (see below).

[2] for a detailed definition of coordinate systems and reference frames, see [17]

5.3.2 Access to Measurement Data and Format Conversion

The set of accelerometer sensor channels as described in Section 5.2 is recorded by the aircraft's *Advanced Flight Test Instrumentation System (AFTIS)*. The responsibility for operation and setup of the instrumentation system lies within the NASA team. Thus, the DSI depends on NASA to calibrate and get access to recorded data. Unfortunately, during the time period when this study thesis was prepared the calibration of TA accelerometers was not fully completed.

The instrumentation of SOFIA is organized in several data streams. Streams 1 through 4 are not only recorded, but also transmitted to the Mission Control Room at NASA Dryden during a mission. The real time sensor set introduced in Section 5.2.3 for instance is part of stream 4. Stream 5 contains all data which is recorded but not transmitted in real time, such as the optical path and structural monitoring accelerometers.

Before recorded measurement data is available in the appropriate format to be able to perform an operational modal analysis by ARTeMIS Extractor, it has to go through several processing and conversion steps (compare Figure 5.4). For a more general description of data processing, including the telescope's housekeeping data, see [12].

Acquisition of data from the aircraft

The recorded data from the aircraft's instrumentation system is copied onto an external hard drive and transferred to NASA Dryden. Depending on the duration of the mission, the total amount of data can exceed several hundred gigabytes. At NASA Dryden, the data archives are processed into so called CMP4 ("Compressed 4") files. These files contain the measurement data in a compressed binary format, separated into individual streams and sampling rates.

The conversion of the measured sensor signal voltage into physical units, such as acceleration in g for accelerometers, takes place during this processing step. The NASA instrumentation team provides a calibration configuration, a so called CIMS file, which contains the information for the conversion process to calculate the physical units.

After passing NASA verification and clearance procedures, the converted CMP4 data is ready to be distributed to the DSI. This is done by the use of external hard drives again.

Conversion of data into a readable format and time frame selection

There are multiple motivations for the next step of format conversion:

1. The CMP4 data cannot by directly interpreted by any of the analysis tools available at the DSI (e.g. MATLAB and ARTeMIS)
2. The CMP4 files generally cover the whole duration of the mission and thus have rather large file sizes. Especially for OMA the analyzed time period is usually shorter when examining the vibration during certain test points which last only a few minutes or even seconds.
3. A CMP4 file usually contains all the channels of a stream. For specialized analyzes such as OMA, only a subset of the available sensor channels is interesting.

To extract desired data chunks from the CMP4 files, a small software tool provided by NASA, the so called *File Conversion Utility (FCU)*, is employed. The FCU creates *comma-separated values (CSV)* text files, which contain the time stamp of a data sample and numeric data of the channels. The graphical interface of the FCU allows to select a constrained time frame to be exported into the CSV files as well as to select a subset of desired channels to be written. Figure 5.5 shows a screenshot of the FCU.

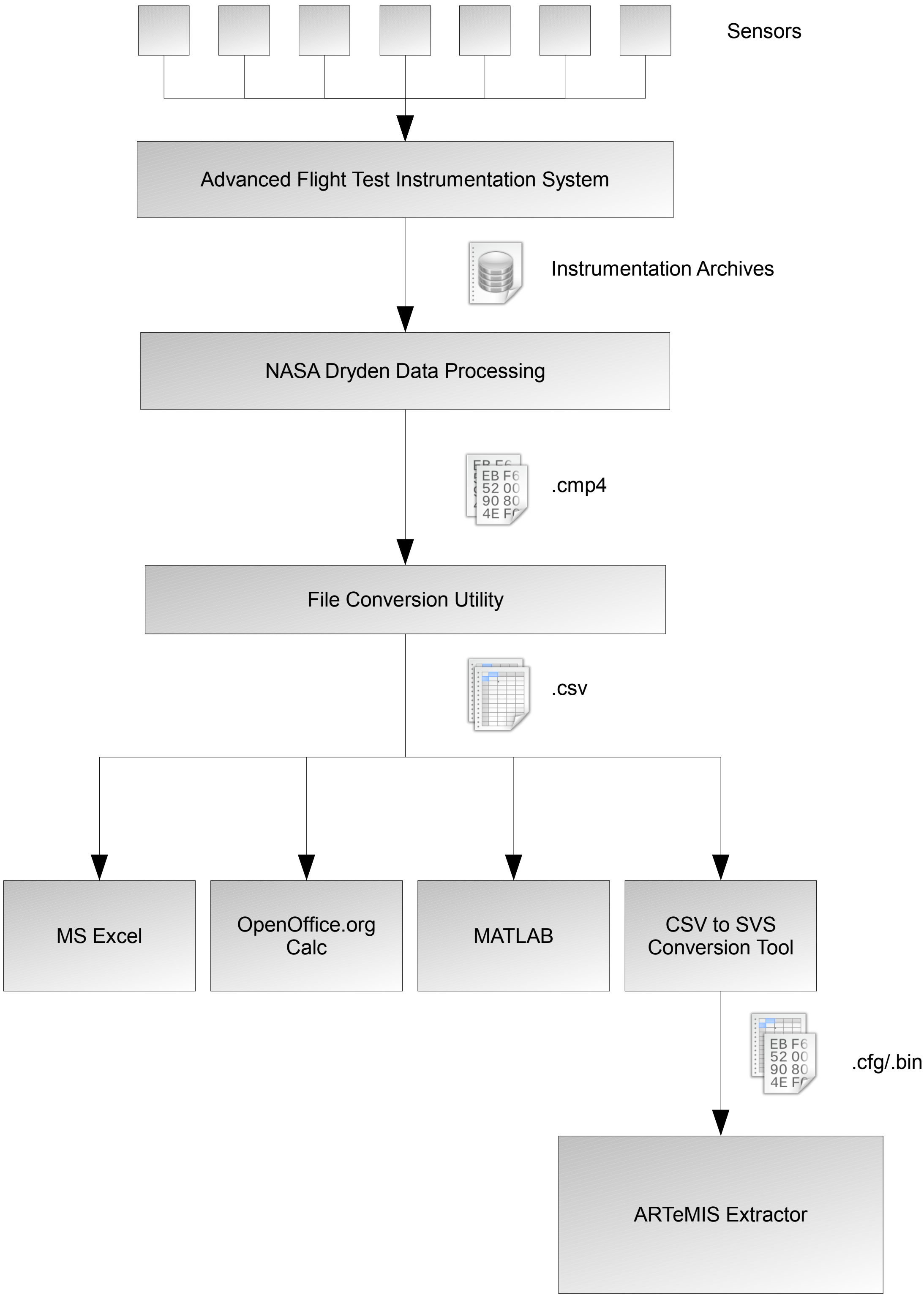

Figure 5.4: Data flow for an operational modal analysis of SOFIA Telescope Assembly vibration measurements.

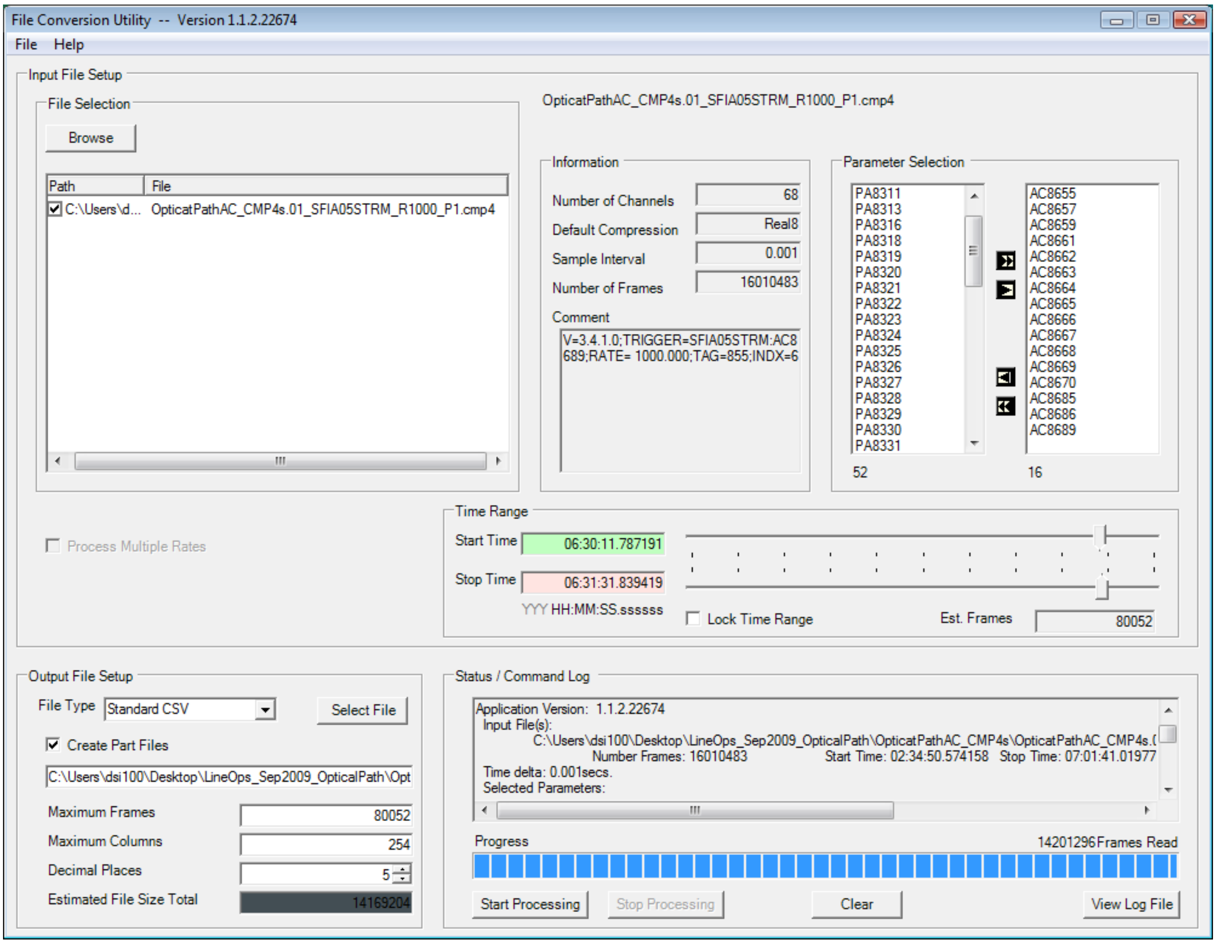

Figure 5.5: The *File Conversion Utility* reads compressed data files (CMP4) containing measurements for a complete mission and exports a selected time range with sensor data of a selected subset into comma-separated values (CSV) text files.

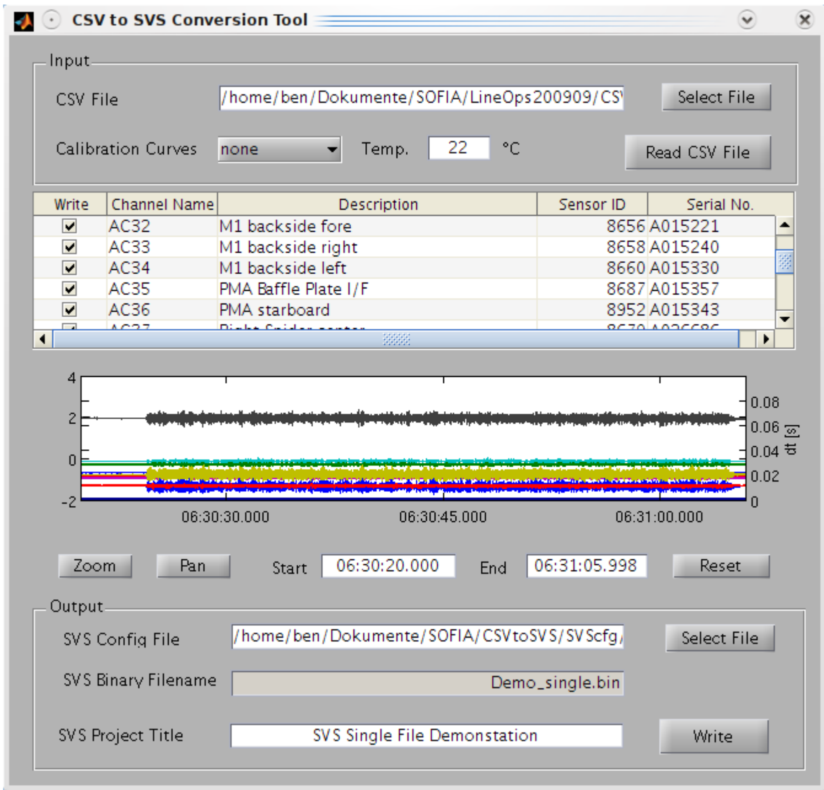

Figure 5.6: The *CSV to SVS Conversion Tool* reads comma separated text files, maps the data channel numbers to sensor locations and displays the contained measurement data. The user can select and examine a smaller portion of the measured signal. The selected time frame and subset of sensor channels is then written into SVS measurement project files, which can be read by ARTeMIS Extractor. This screenshot shows the single file version of the *CSV to SVS Conversion Tool*.

CSV files can be processed by a large amount of software tools. Spreadsheet calculation programs such as MS Excel or OpenOffice.org Calc for instance can import CSV files into spreadsheet tables and simple data analysis can be performed within those programs. Most versions have a limitation on the number of lines per table. The FCU has an option to split large CSV files in order to meet that constraint of e.g. 65,000 lines per table. CSV text files can also be imported into MATLAB. In this case there is no limitation on sample frames so that larger CSV files can be processed.

Preparation for Operational Modal Analysis: The CSV to SVS Conversion Tool

For the specific purpose of analyzing SOFIA vibration data with *ARTeMIS Extractor*, a graphical tool has been developed which converts CSV files created by the FCU into a SVS measurement project. The design and develop-opent of this *CSV to SVS Conversion Tool* has been a part of the work for this study thesis. It is implemented as a set of MATLAB scripts which provide a graphical interface where input and output parameters can be specified.

Figure 5.6 contains a screenshot of the *CSV to SVS Conversion Tool* in the single CSV file version. This version is fully functional, but is limited to import a single CSV file. All present channels in the CSV that belong to the TA accelerometer instrumentation are automatically detected and assigned to their sensor setup. The graphical tool allows to select and de-select the sensor channels which are to be exported into the SVS measurement project. The channel signals are plotted into a chart where one can zoom in or move the displayed time frame with the panning

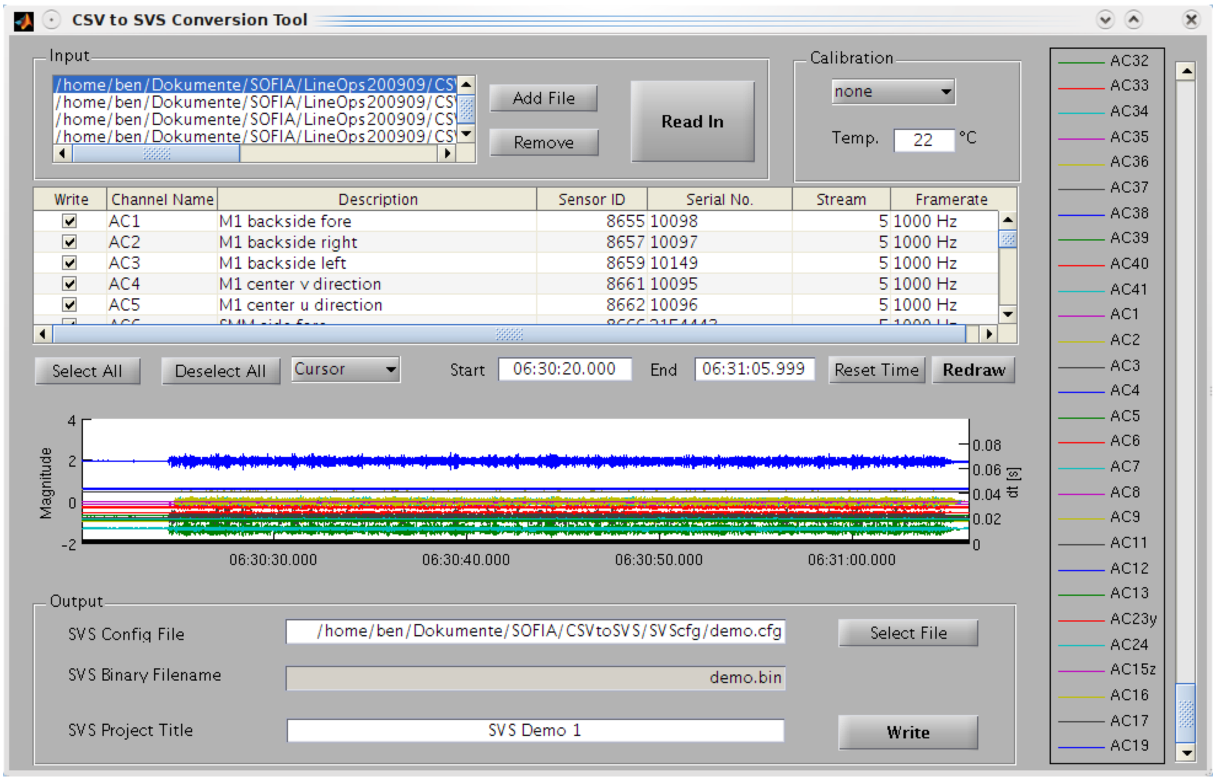

Figure 5.7: The multi file version of the *CSV to SVS Conversion Tool* is an enhancement of the single file version. It can read several comma-separated-value files at the same time and display their signal content together. The merging of different data sources into one output file requires the downsampling and possibly resampling of data, which has not been implemented yet.

tool. The limits of the chart are then used as the starting point and the end of the time frame that is exported into the SVS measurement project.

The tool includes the geometrical information as introduced in Section 5.3.1, and writes it into the corresponding sections of the SVS configuration file so that it is available for ARTeMIS Extractor.

Since the TA instrumentation accelerometers are assigned to two individual data streams and are recorded with two different sampling rates (compare Table 5.1 to Table 5.2 and Table 5.3), it turned out that there exists more than one CSV file for a single time range. Also, the data needs an additional processing step before it can be exported as homogeneous data into an SVS measurement project. The data channels sampled with 1000 Hz need to be downsampled to 500 Hz to match the channels of the lower rate.

For this purpose, a multi file version of the *CSV to SVS Conversion Tool* is required. The multi file version of the *CSV to SVS Conversion Tool* is intended to be capable of importing multiple CSV files and merging the channels contained in those files into a single data set. Figure 5.7 shows a screenshot of the multi-file version in development. It can read several CSV files with different sampling rates and display the contained measurement data as time series in a combined chart.

However, the development of the multi-file version of the *CSV to SVS Conversion Tool* could not be fully completed during the work for this study thesis. The complexity of the process of merging the sampling data into a homogenous set of samples depends on the synchronization properties of the provided data. The test data that was available for testing during the creation of the *CSV to SVS Conversion Tool* was not fully synchronized. The time stamps of the samples contained in channel 4 had a time lag to those in channel 5. The available data originated from the Line

Operations in September 2009 (see Section 5.4), during which the SOFIA time synchronization system IRIG-B was not available. Whether SOFIA stream data samples will be synchronized between individual streams during future test campaigns, could not be verified. Therefore, it is possible that the *CSV to SVS Conversion* tool might need a function which resamples one stream in order to be able to export all available sensor channels of the TA into a single SVS measurement project in order to perform an overall operational modal analysis for the whole TA geometry. Both the downsampling and resampling function have not been implemented yet, but will be developed as soon as mission data is available which can be evaluated with respect to its synchronization properties.

5.4 Conducted Data Analysis: Image Jitter with FDC Measurements

5.4.1 Available Data Set

In September 2009, a Line Operations (Line Ops) test campaign was conducted. The aircraft was pulled out of the hangar and the telescope system was used to look at the sky during nighttime. One of the main objectives of these Line Ops was to checkout a fast camera, the Fast Diagnostic Camera (FDC), which was mounted in the place of the Focal Plane Imager (FPI) [27]. The FDC can record an image as it appears in the focal plane as fast as 400 times per second. One experiment during the Line Ops was to use the FDC to measure image jitter while the telescope was being excited by the Fine Drive pointing control actuator.

The initial goal was to correlate the direct image jitter measurement from the FDC to accelerometer data, especially from the optical path. The NASA instrumentation team had been requested to run the instrumentation recording system in order to obtain the TA acceleration data. Unfortunately, since the calibration of TA accelerometers had not been fully completed at the time of the Line Ops, the quality of the obtained accelerometer data was not sufficient to perform an OMA or to be able to correlate TA vibration to measured image jitter. Thus, the analysis of the image jitter experiment had to be limited to the FDC measurements only.

In accordance with the premises of operational modal analysis, the excitation of the telescope structure by the Fine Drive actuators was Gaussian white noise. There were test runs with excitation of single axes, but the data presented below was obtained during combined excitation around all three actuator axes: Elevation, Cross-Elevation and Line of Sight.

5.4.2 Results

Figure 5.8 shows power spectral densities of the measured image jitter in the V and W Axis of the Telescope Assembly Reference Frame. There is a large amount of energy on the lower frequency band below 20 Hz, which originates in rigid body motion and has to be dealt with by the pointing controller using primarily the TA's gyroscopes. Additionally, peaks can clearly be identified in the higher frequency range. These peaks are an effect of structural vibration modes of the TA. They contribute to the overall pointing stability and image quality.

The quantitative pointing stability and image quality is measured in the root mean square (RMS) of the image deviation of the desired pointing direction over time. According to Parseval's theorem [28], the root mean square over time, which reflects the total energy of the signal, is equivalent to to the integral over frequency of the power spectral density of the signal. Figure 5.9 shows cumulative RMS plots of the image jitter in both axes. The steps within the curves illustrate, how much a mode contributes to the overall image jitter RMS. Note that the y-axis of the charts doesn't start at 0 arcseconds. The component of the image jitter originating in rigid body motion is not within the range of the plots, only the flexible vibration component is shown.

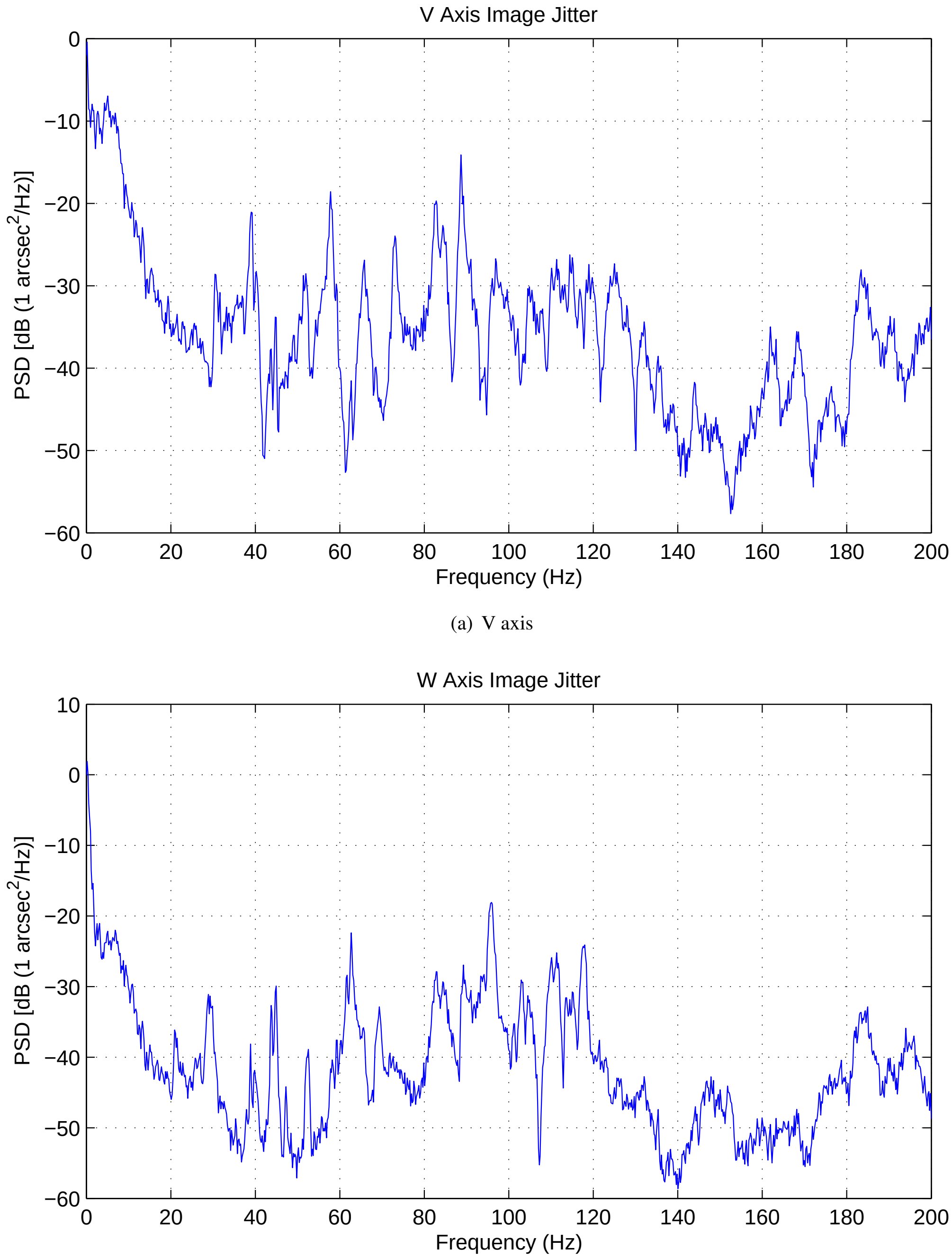

(a) V axis

(b) W axis

Figure 5.8: Power spectral densities of image jitter measurements with the Fast Diagnostic Camera. While most of the energy of the measured image motion is contained in the lower spectrum, representing rigid body motion, a significant number of high energy peaks, originating from flexible modes, occur in the frequency range from 20 to 120 Hz.

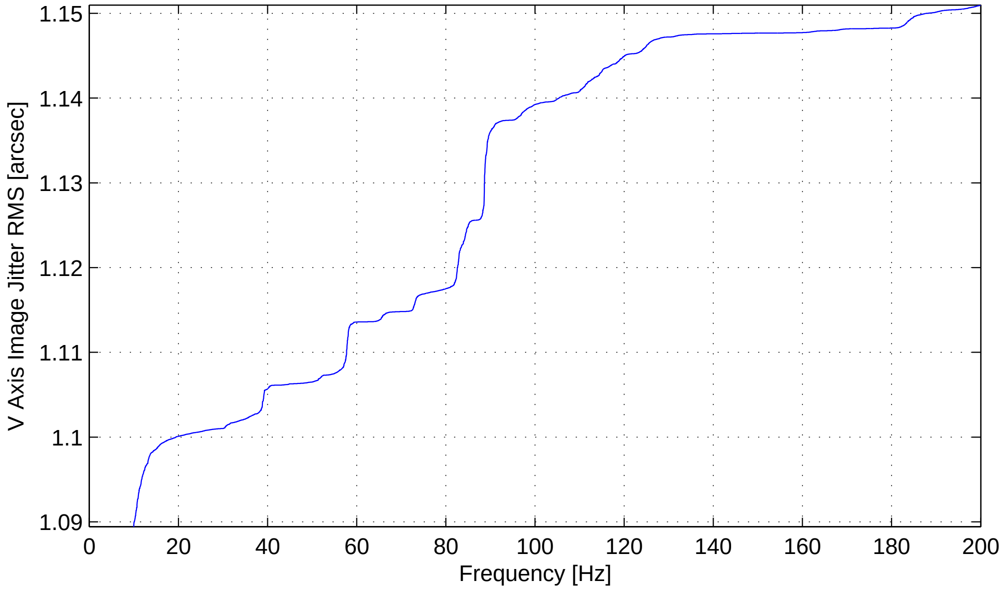

(a) V axis

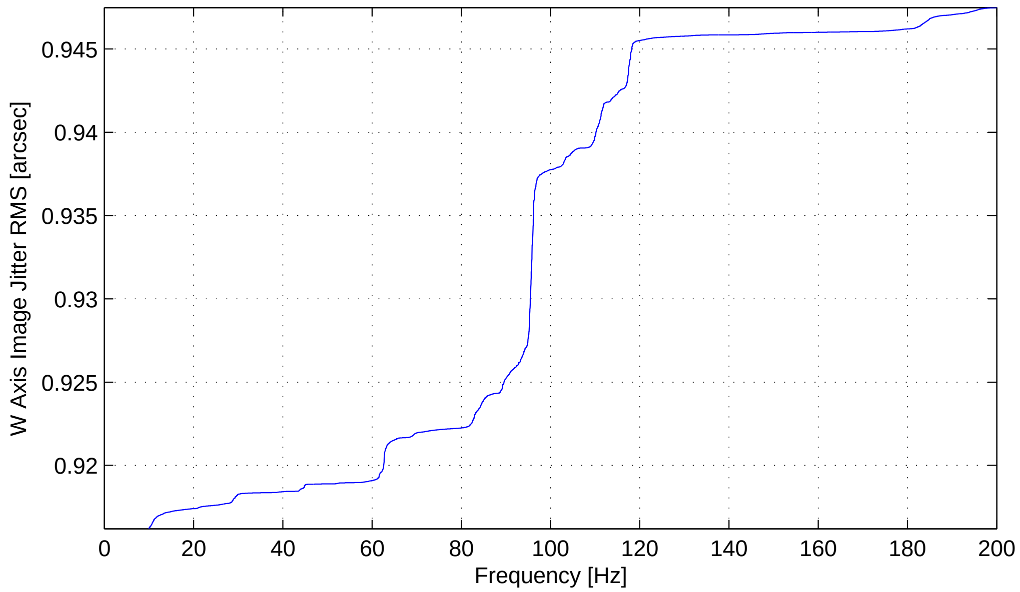

(b) W axis

Figure 5.9: Cumulative root mean square image jitter of Fast Diagnostic Camera measurements. The integration of power spectral densities illustrates how much a peak contributes to the overall image jitter. The higher the "step" in the plot, the more a mode contributes to the total image jitter.

5.4.3 Interpretation and Outlook

The cumulative root mean square plots indicate that especially the rocking modes in the range from 50 to 100 Hz have a major contribution factor towards the image jitter. As it seems, the dumbbell modes ($\sim$ 22 and 24 Hz) do not show any visible contribution to the image jitter. But this should not lead to the conclusion that they do not contribute to the pointing stability and image quality during operational conditions. In the specific experiment at hand, the telescope structure was excited with the Fine Drive actuators distributed around the center of gravity of the Telescope Assembly at the hydrostatic bearing. It is obvious that the dumbbell modes are not well reached with this type of excitation. Fast Diagnostic Camera measurements during operational conditions – an open door flight – would help significantly with the identification of the contribution of structural modes to image jitter.

For future research in this field, it seems promising to use the results of the Fast Diagnostic Camera image jitter analysis and correlate them with future optical path accelerometer vibration measurements while the Telescope Assembly was excited by the Fine Drive actuators in a similar way. This would help to verify and improve the existing model with ray trace equations of the telescope's optical system which yield the image motion in dependency of mirror vibration [23]. There exists an end-to-end simulation model, which incorporates these ray trace equations. A simulation with the conditions of the Fast Diagnostic Camera image jitter experiments would help to gain further insight into the model.

The ultimate goal is to incorporate the advanced knowledge of flexible body vibration into the pointing stabilization controller in order to improve the pointing stability and image quality. This feature is called *Flexible Body Compensation (FBC)* [20], see also Chapter 6.

6 Conclusions and Suggestions for Future Research and Development

The study thesis at hand presents the theory behind *Operational Modal Analysis (OMA)* and shows that its application to the SOFIA Telescope system optimization process is feasible. Operational Modal Analysis promises useful results in order to improve pointing stability and image quality of the Stratospheric Observatory for Infrared Astronomy (SOFIA).

Because the algorithms of Operational Modal Analysis, as implemented in ARTeMIS Extractor, are not just a "black box", but can be well described, the analyst has a powerful tool at hand to describe a complex system such as the SOFIA Telescope Assembly with respect to its dynamical properties. Because the theory behind the methods is well understood, it should be straight forward to choose the correct parameters in a software like ARTeMIS Extractor. The confidence in the evaluation of received results is much higher with a thorough knowledge of how the underlying system of a tool works.

Additionally, the interface of the OMA software has been tested extensively so that many limitations or shortcomings are already known and can be worked around. The experiment with the aluminium plate served very well as a test case in this regard.

Although no operational flight test data could be analyzed within the scope of this study thesis, the analysis of vibration measurement data, as it will hopefully be available very soon, should be possible very quickly. Major effort has been spent within the work of this thesis to prepare the automatization of data processing, aimed at minimizing the time needed, from when the measurement is taken during a mission until the data is loaded into the operational modal analysis software. The *CSV to SVS Conversion Tool* is part of this effort. It converts the available measurement data and automatically incorporates the geometry and channel property information of the Telescope Assembly (TA) instrumentation setup when creating files that are suitable as input for the operational modal analysis software.

Depending on the synchronization properties of measurement data taken by the instrumentation system with a working time syncronization system in the aircraft (IRIG-B), it might be necessary to include a resampling function into the *CSV to SVS Conversion Tool* in order to remove the time shift between channels which belong to different data streams.

Another option to overcome the limitation of not synchronized data channels would be to include a function which takes the time shifts of channels into account directly into the analysis software. For the methods working in the frequency domain – the family of Frequency Domain Decomposition techniques – it would be a fairly easy task to include such a function: Since the damping and natural frequency parameters are taken from power spectral densities, the time lag between channels would not affect the estimation process of these modal parmeters. For the estimation of mode shapes and their animation, the shift in phase angle could easily be added to the mode shape vector. Such a method for compensating time lags in measurement data would eliminate the disadvantage of reducing data quality as it occurs when data channels have to be resampled. However, since SSI works in the time domain, the approach as proposed above is not possible for that method.

The measurements of image jitter with the Fast Diagonostic Camera provide a direct impression of the influence of flexible vibration modes to the image quality. Since it was not possible to correlate the measured image jitter to accelerometer data during the September 2009 Line Ops, this task should be accomplished the next time when the Fast Diagnostic Camera is mounted on the Telescop Assembly. The correlation of Fast Diagnostic Camera measurements to accelerometer data also helps to improve the end-to-end simulation model mentioned in Section 5.4.3, which is also employed in the development of the Flexible Body Compensation controller.

The Flexible Body Compensation, in its current design, uses vibration data obtained from gyroscopes and accelerometers in order to compensate image jitter in a feed forward control scheme. Future development and optimization efforts of the Flexible Body Compensation will include adding the optical path accelerometers into the estimation of image motion, which is a fundamental part of the Flexible Body Compensation. The gyroscopes and accelerometers located at the Telescope Assembly's center of gravity are the driving sensors for the compensation of flexible body motion of lower frequencies, whereas the optical path accelerometers will be the drivers for the compensation of disturbances at higher frequencies such as image jitter created by the rocking modes. In combination with a fast moving Secondary Mirror Mechanism, this sensor fusion approach promises significant improvements for image quality and pointing stability. A diploma thesis, in preparation by Anett Seifert, will deal with this task.

A Estimated Modal Parameters of Aluminium Plate

This appendix contains the results of the preliminary experiment as described in Chapter 4.

A.1 Sensor Setup Layouts

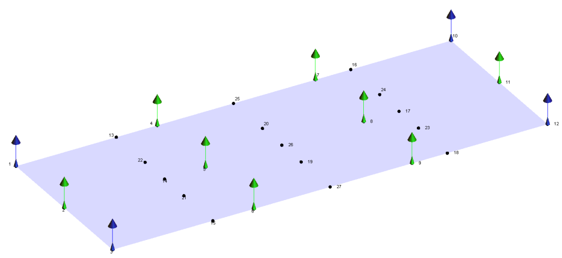

(a) Setup A

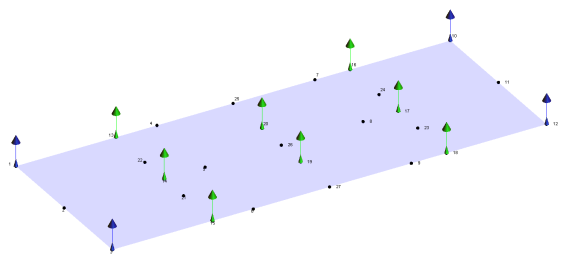

(b) Setup B

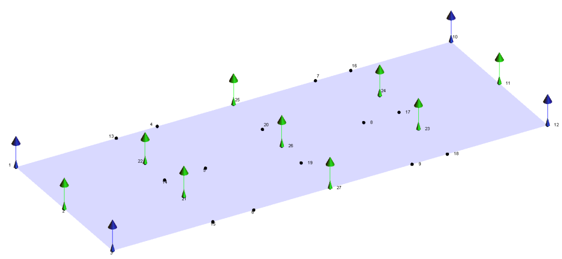

(c) Setup C

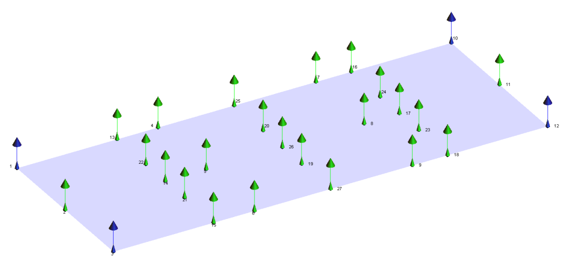

(d) All setups merged for multi setup analysis

Figure A.1: Sensor placement layouts of three different instrumentation sets and the resulting spatial resolution of a merged instrumentation. The sensors at the corners of the plate are common to all setups and are thus marked as reference channels (blue arrow as opposed to green arrow).

A.2 Identified Modes in Individual Test Setups

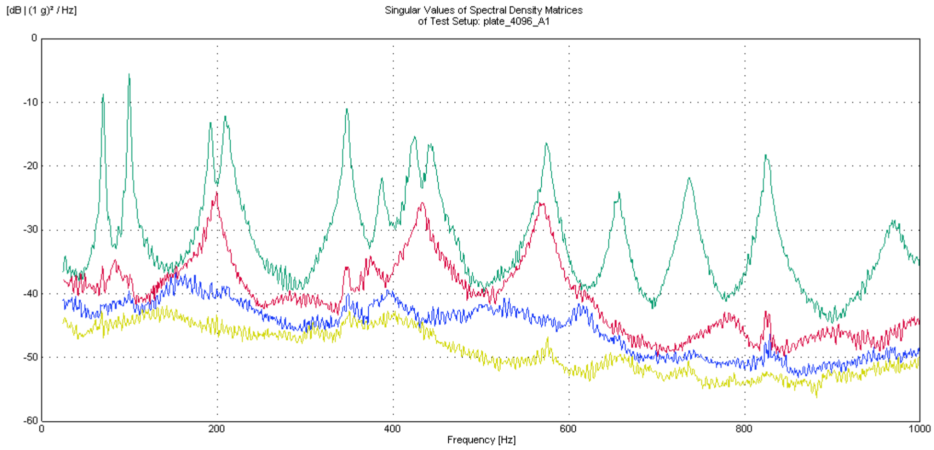

(a) Setup A

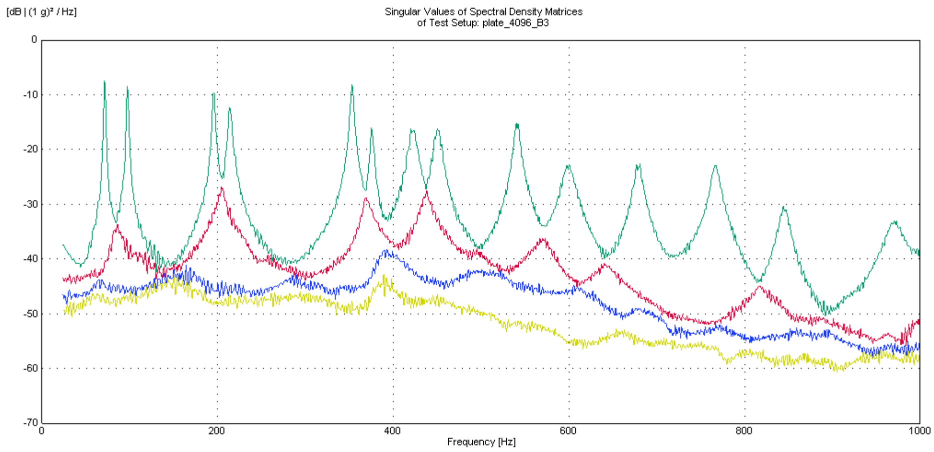

(b) Setup B

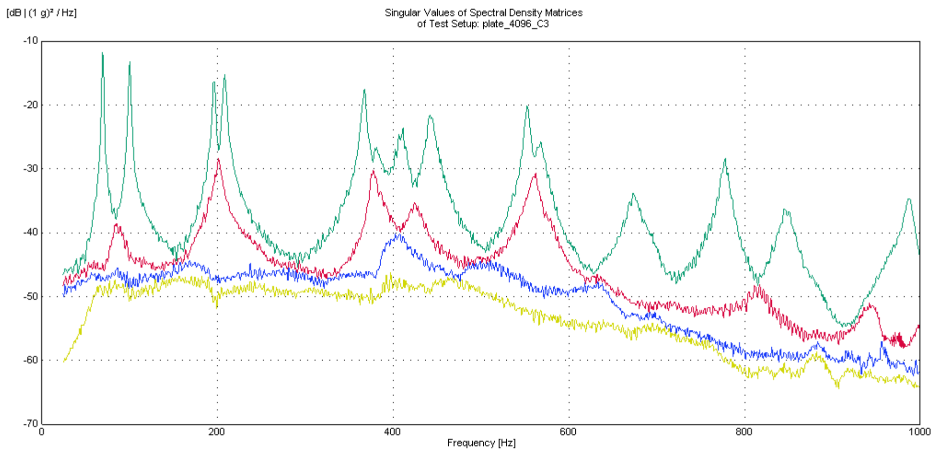

(c) Setup C

Figure A.2: Singular value decomposition of spectral densities measured with three different sensor layouts

Tables A.1 through A.3 list natural frequencies and damping ratios of all identified modes of sensor Setups A, B and C broken down to all employed identification techniques. The labels formatted “X-Y” indicate the number of nodal lines across the longer (X) and shorter (Y) dimension of the plate for that mode. Compare to Figure A.7. As described in Section 4.4.1 the exact classification of mode shapes was not always possible due to limited spatial resolution. Nevertheless, the modes were labeled according to extra information by referring to the multi-setup and FEM results.

In Table A.2 and Table A.3 the labels of the modes 6, 7, 9 and 10 are highlighted in bold in order to indicate that these modes of Setup B and C are shifted when compared to Table A.1 of Setup A. Note that there is no damping ratio estimation by the basic FDD algorithm.

The data of Setups B and C is illustrated by Figures A.3 through A.6. The diagrams for Setup A, Figure 4.4 and Figure 4.5, can be found in Section 4.4.1 on page 47.

Table A.1: Modal parameters of identified modes in setup A

(a) Natural frequencies

Algorithm		FDD	EFDD	CFDD	SSI-UPC	SSI-PC	SSI-CVA	Avg.	Std. Dev.
		Frequency f_i [Hz]							
Mode 1	"2-0"	70	69.6	69.7	69.6	69.3	69.6	69.6	0.24
Mode 2	"1-1"	99	99.2	99.3	99.3	99.2	99.3	99.2	0.10
Mode 3	"3-0"	192	192.0	192.0	191.9	191.9	191.9	192.0	0.05
Mode 4	"2-1"	208	209.8	209.6	210.2	210.2	210.2	209.7	0.85
Mode 5	"3-1"	347	347.1	347.1	347.1	347.1	347.1	347.1	0.04
Mode 6	"0-2"	387	386.1	386.6	386.3	386.6	386.3	386.5	0.32
Mode 7	"4-0"	424	423.4	423.4	423.6	423.6	423.6	423.6	0.22
Mode 8	"1-2"	443	442.5	442.5	442.9	442.8	442.9	442.8	0.22
Mode 9	"2-2"	566	566.6	567.0	567.9	568.7	567.9	567.4	0.99
Mode 10	"4-1"	574	574.7	575.1	575.2	575.3	575.3	574.9	0.51
Mode 11	"5-0"	658	656.0	655.8	656.3	656.4	656.3	656.5	0.78
Mode 12	"3-2"	737	737.2	737.1	737.0	737.0	737.0	737.1	0.08
Mode 13	"5-1"	824	825.5	825.5	825.5	825.5	825.5	825.3	0.61
Mode 14	"6-0"	971	969.6	970.0	969.3	970.1	969.3	969.9	0.64

(b) Damping ratios

Algorithm		FDD	EFDD	CFDD	SSI-UPC	SSI-PC	SSI-CVA	Avg.	Std. Dev.
		Damping Ratio ζ_i [%]							
Mode 1	"2-0"	-	1.2	1.1	0.8	1.2	0.8	1.0	0.22
Mode 2	"1-1"	-	0.8	0.7	0.6	0.7	0.6	0.7	0.08
Mode 3	"3-0"	-	1.2	0.7	1.2	1.2	1.2	1.1	0.21
Mode 4	"2-1"	-	1.7	0.9	1.5	1.5	1.5	1.4	0.29
Mode 5	"3-1"	-	0.6	0.5	0.6	0.6	0.6	0.6	0.04
Mode 6	"0-2"	-	1.2	0.7	1.0	1.1	1.0	1.0	0.19
Mode 7	"4-0"	-	0.9	0.5	0.8	0.8	0.8	0.8	0.16
Mode 8	"1-2"	-	1.0	0.5	1.0	1.0	1.0	0.9	0.22
Mode 9	"2-2"	-	1.5	1.0	1.5	1.5	1.5	1.4	0.24
Mode 10	"4-1"	-	0.6	0.5	0.6	0.6	0.6	0.6	0.05
Mode 11	"5-0"	-	0.8	0.7	0.8	0.8	0.8	0.8	0.07
Mode 12	"3-2"	-	0.8	0.6	0.5	0.6	0.6	0.6	0.11
Mode 13	"5-1"	-	0.4	0.4	0.4	0.4	0.4	0.4	0.02
Mode 14	"6-0"	-	1.3	0.7	1.0	1.0	1.0	1.0	0.21

Table A.2: Modal parameters of identified modes in setup B

(a) Natural frequencies

Algorithm		FDD	EFDD	CFDD	SSI-UPC	SSI-PC	SSI-CVA	Avg.	Std. Dev.
		Frequency f_i [Hz]							
Mode 1	“2-0”	71	71.4	71.4	71.2	71.2	71.7	71.3	0.23
Mode 2	“1-1”	97	97.2	97.3	97.3	97.3	97.2	97.2	0.11
Mode 3	“3-0”	196	195.5	195.5	195.5	195.4	195.5	195.6	0.22
Mode 4	“2-1”	214	213.9	214.0	214.1	214.1	214.1	214.0	0.08
Mode 5	“3-1”	353	353.0	353.1	353.0	353.0	353.0	353.0	0.04
Mode 6	“**4-0**”	375	375.6	375.6	375.9	375.9	375.9	375.7	0.35
Mode 7	“**0-2**”	420	421.9	422.2	422.4	422.4	422.4	421.9	0.94
Mode 8	“1-2”	450	450.6	450.4	450.5	450.5	450.5	450.4	0.21
Mode 9	“**4-1**”	540	540.8	540.9	541.1	541.1	541.1	540.8	0.43
Mode 10	“**2-2**”	600	598.7	599.1	599.5	599.4	599.6	599.4	0.44
Mode 11	“5-0”	681	679.0	679.0	678.7	678.8	678.8	679.2	0.88
Mode 12	“3-2”	767	766.6	766.7	767.3	767.2	767.3	767.0	0.31
Mode 13	“5-1”	844	845.2	844.9	844.7	844.7	844.9	844.7	0.40
Mode 14	“6-0”	973	971.0	971.3	969.3	969.5	969.2	970.6	1.50
Mode 15	“4-2”	996	996.7	996.1	997.0	997.8	1002.0	997.6	2.25

(b) Damping ratios

Algorithm		FDD	EFDD	CFDD	SSI-UPC	SSI-PC	SSI-CVA	Avg.	Std. Dev.
		Damping Ratio ζ_i [%]							
Mode 1	“2-0”	-	0.9	1.0	0.6	0.6	0.8	0.8	0.19
Mode 2	“1-1”	-	0.8	0.8	0.6	0.6	0.6	0.7	0.10
Mode 3	“3-0”	-	0.6	0.5	0.6	0.6	0.6	0.6	0.06
Mode 4	“2-1”	-	1.0	0.7	0.9	1.0	0.9	0.9	0.12
Mode 5	“3-1”	-	0.5	0.4	0.4	0.4	0.4	0.4	0.03
Mode 6	“**4-0**”	-	0.6	0.4	0.4	0.5	0.4	0.5	0.06
Mode 7	“**0-2**”	-	1.1	0.7	0.9	0.9	0.9	0.9	0.14
Mode 8	“1-2”	-	1.0	0.6	0.7	0.8	0.7	0.8	0.15
Mode 9	“**4-1**”	-	0.6	0.5	0.5	0.5	0.5	0.5	0.06
Mode 10	“**2-2**”	-	1.2	0.8	1.0	1.0	1.0	1.0	0.13
Mode 11	“5-0”	-	0.7	0.6	0.6	0.6	0.6	0.6	0.04
Mode 12	“3-2”	-	0.6	0.5	0.6	0.6	0.6	0.6	0.04
Mode 13	“5-1”	-	0.8	0.5	0.6	0.6	0.6	0.6	0.10
Mode 14	“6-0”	-	0.7	0.6	1.0	1.0	1.2	0.9	0.24
Mode 15	“4-2”	-	1.5	1.0	1.2	1.3	1.6	1.3	0.25

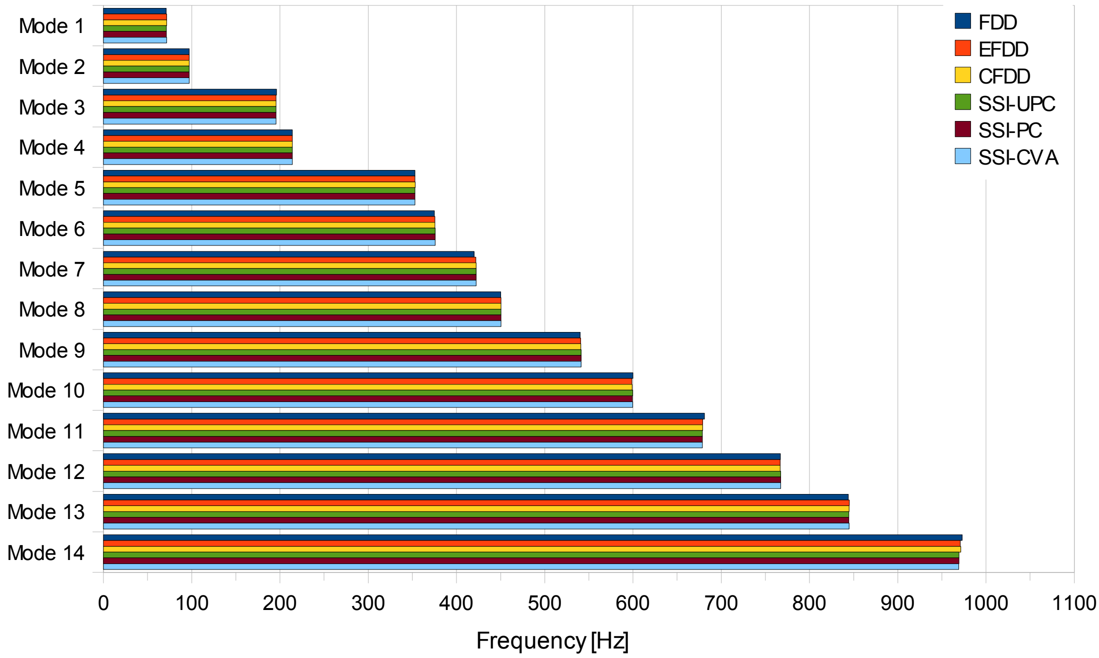

Figure A.3: Identified natural frequencies for sensor setup B

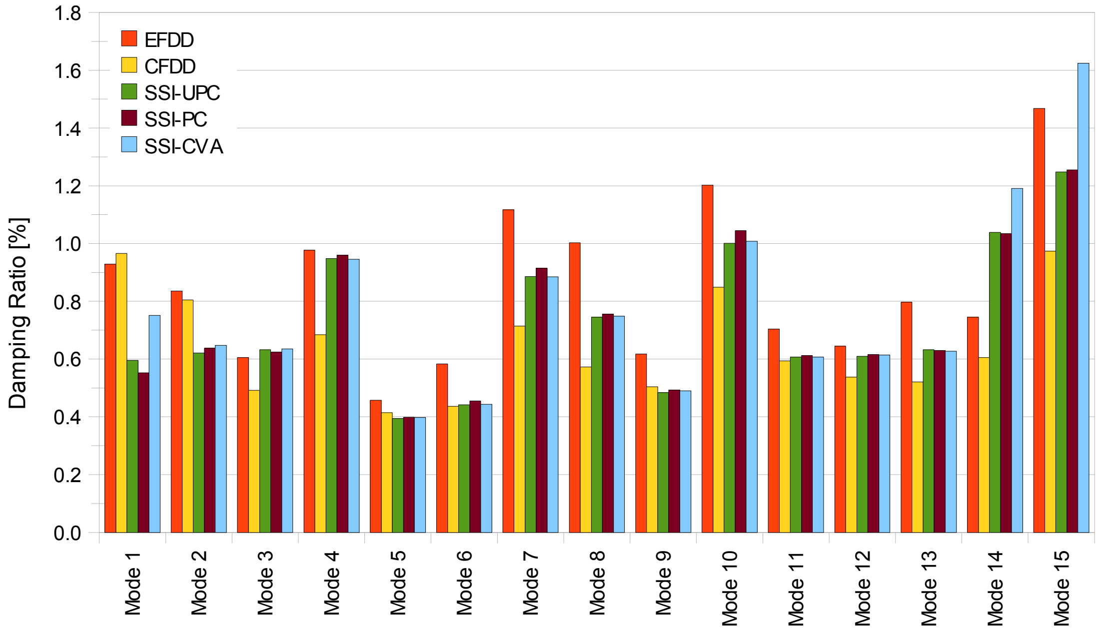

Figure A.4: Identified damping ratios for sensor setup B

Table A.3: Modal parameters of identified modes in setup C

(a) Natural frequencies

Algorithm		FDD	EFDD	CFDD	SSI-UPC	SSI-PC	SSI-CVA	Avg.	Std. Dev.
					Frequency f_i [Hz]				
Mode 1	“2-0”	69	69.3	69.2	69.1	69.1	69.1	69.1	0.10
Mode 2	“1-1”	100	99.8	99.8	99.8	99.8	99.8	99.8	0.09
Mode 3	“3-0”	196	195.9	195.8	195.5	195.5	195.5	195.7	0.23
Mode 4	“2-1”	208	208.0	208.0	208.1	208.1	208.1	208.1	0.05
Mode 5	“3-1”	367	366.7	366.8	366.7	366.7	366.7	366.8	0.12
Mode 6	“**4-0**”	381	381.1	381.3	381.5	381.4	381.5	381.3	0.21
Mode 7	“**0-2**”	411	409.4	409.5	409.3	409.3	409.3	409.6	0.67
Mode 8	“1-2”	442	442.8	442.6	443.3	443.3	443.3	442.9	0.53
Mode 9	“**4-1**”	552	552.8	552.5	552.6	552.7	552.6	552.5	0.28
Mode 10	“**2-2**”	568	566.5	567.1	567.1	567.1	567.1	567.2	0.48
Mode 11	“5-0”	673	674.5	674.6	675.2	675.1	675.3	674.6	0.86
Mode 12	“3-2”	778	777.6	777.3	777.3	777.3	777.3	777.5	0.29
Mode 13	“5-1”	845	847.7	847.1	848.1	848.0	848.2	847.4	1.22
Mode 14	“6-0”	969	971.6	972.2	969.3	969.5	970.7	970.4	1.32
Mode 15	“4-2”	988	987.5	987.4	987.6	987.7	987.6	987.6	0.21

(b) Damping ratios

Algorithm		FDD	EFDD	CFDD	SSI-UPC	SSI-PC	SSI-CVA	Avg.	Std. Dev.
					Damping Ratio ζ_i [%]				
Mode 1	“2-0”	-	1.0	0.9	0.7	0.7	0.7	0.8	0.15
Mode 2	“1-1”	-	0.9	0.8	1.0	1.0	1.0	1.0	0.08
Mode 3	“3-0”	-	0.8	0.5	1.0	1.0	1.0	0.8	0.20
Mode 4	“2-1”	-	1.0	0.6	1.0	1.0	1.0	0.9	0.21
Mode 5	“3-1”	-	0.7	0.6	0.9	0.9	0.9	0.8	0.12
Mode 6	“**4-0**”	-	1.5	0.8	1.2	1.2	1.2	1.2	0.25
Mode 7	“**0-2**”	-	1.2	0.6	1.3	1.3	1.3	1.1	0.30
Mode 8	“1-2”	-	1.1	0.7	1.1	1.1	1.1	1.0	0.18
Mode 9	“**4-1**”	-	0.5	0.3	0.6	0.6	0.6	0.5	0.14
Mode 10	“**2-2**”	-	0.9	0.8	1.1	1.1	1.1	1.0	0.14
Mode 11	“5-0”	-	1.7	1.0	1.3	1.3	1.3	1.3	0.25
Mode 12	“3-2”	-	0.6	0.5	0.6	0.6	0.6	0.6	0.04
Mode 13	“5-1”	-	1.0	0.8	0.9	0.9	0.9	0.9	0.08
Mode 14	“6-0”	-	1.5	1.0	1.5	1.5	1.7	1.4	0.26
Mode 15	“4-2”	-	0.6	0.4	0.4	0.4	0.4	0.5	0.08

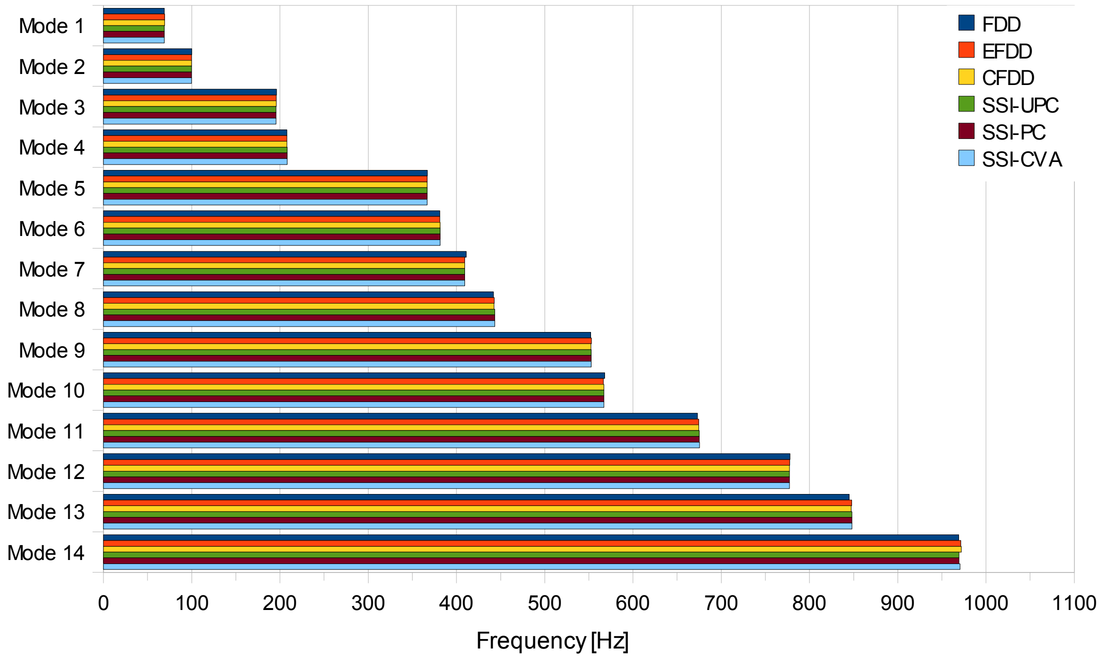

Figure A.5: Identified natural frequencies for sensor setup C

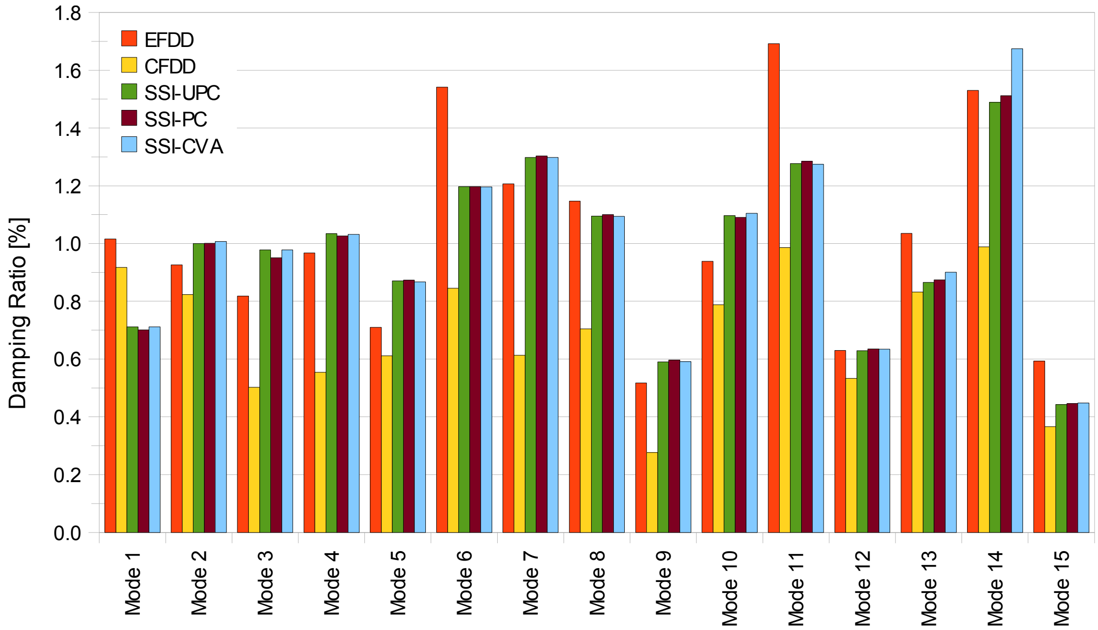

Figure A.6: Identified damping ratios for sensor setup C

Illustrations of mode shapes (Sensor setup A only) are given in Figure A.7. As it can be seen for example in mode 14 (subfigure A.7(n)), the spatial resolution is not high enough to reflect the 6 nodal lines which are shown in subfigure A.8(n) and A.9(n).

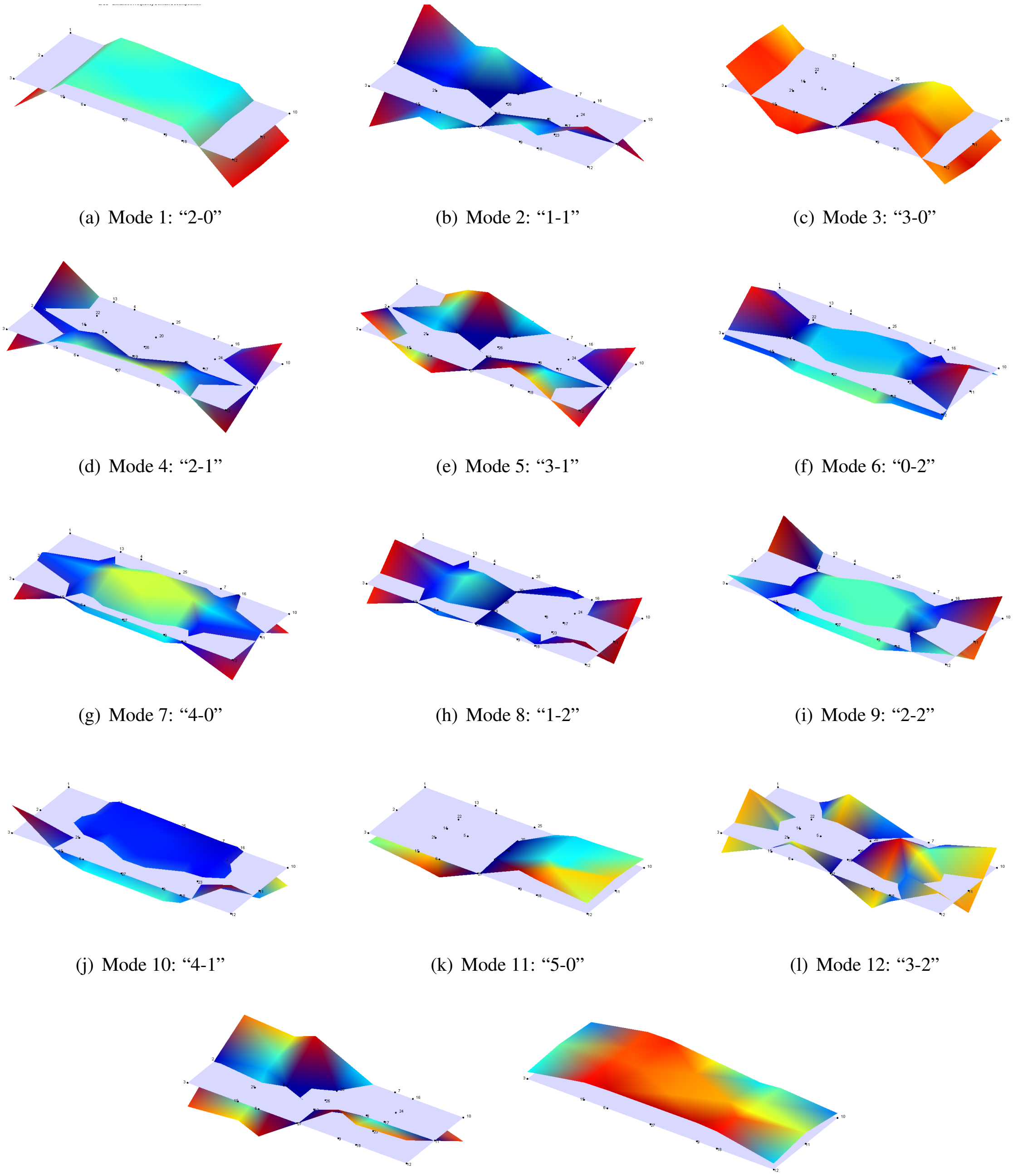

(a) Mode 1: “2-0”
(b) Mode 2: “1-1”
(c) Mode 3: “3-0”
(d) Mode 4: “2-1”
(e) Mode 5: “3-1”
(f) Mode 6: “0-2”
(g) Mode 7: “4-0”
(h) Mode 8: “1-2”
(i) Mode 9: “2-2”
(j) Mode 10: “4-1”
(k) Mode 11: “5-0”
(l) Mode 12: “3-2”
(m) Mode 13: “5-1”
(n) Mode 14: “6-0”

Figure A.7: Identified mode shapes for test setup A

A.3 Multi-Setup Analysis

Since the natural frequencies of the plate are affected significantly by the different sensor setups, it is not useful to average these results in a multi-setup analysis project. The enhanced spatial resolution for mode shapes however shall be illustrated by Figure A.8.

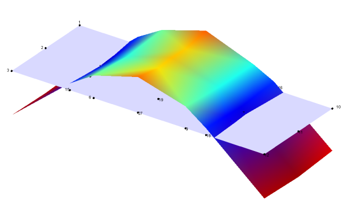

(a) Mode 1: “2-0”

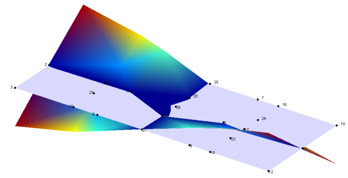

(b) Mode 2: “1-1”

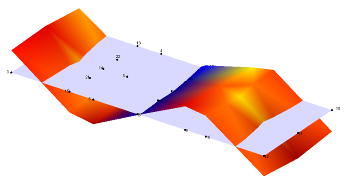

(c) Mode 3: “3-0”

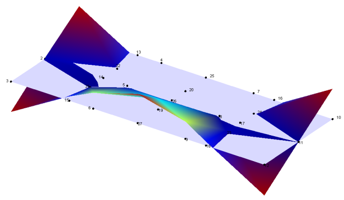

(d) Mode 4: “2-1”

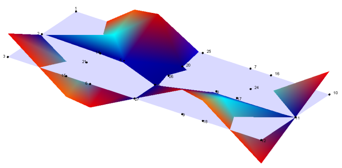

(e) Mode 5: “3-1”

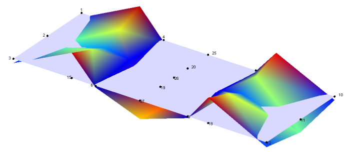

(f) Mode 6: “4-0”

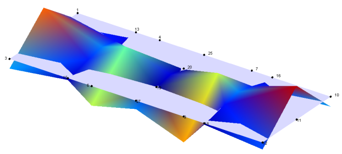

(g) Mode 7: “0-2”

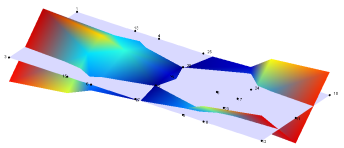

(h) Mode 8: “1-2”

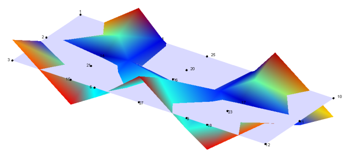

(i) Mode 9: “4-1”

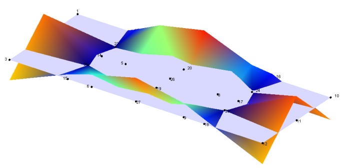

(j) Mode 10: “2-2”

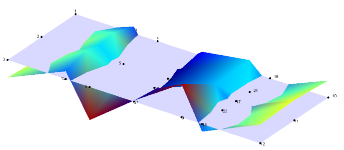

(k) Mode 11: “5-0”

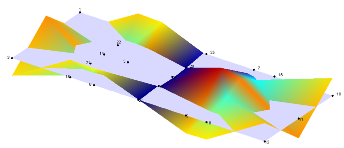

(l) Mode 12: “3-2”

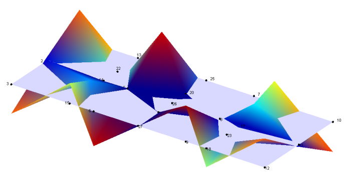

(m) Mode 13: “5-1”

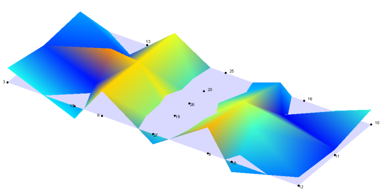

(n) Mode 14: “6-0”

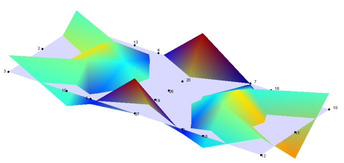

(o) Mode 15: “4-2”

Figure A.8: Mode shapes identified by multi-test setup

A.4 FEM Results

The results of the FEM analyzes are shown in Table A.4 and Figure A.9. Due to the nature of mathematical modal analysis, there are no damping ratios which could be calculated. Since the FEM analyzes were configured to yield only 14 flexible modes, the "6-0"-mode found in the experiment by Setup B and C is not present in the FEM results but the "4-2"-mode is. Like in Table A.2 and A.3, the lines of the modes 6, 7, 9 and 10 are highlighted in bold for Setup B and C in order to emphasize that their order is shifted when compared to Setup A and thus the natural frequencies are not in strictly ascending order.

Table A.4: Comparison of natural frequencies found by experimental identification and FEM analysis

		Setup A			**Setup B**			**Setup C**		
		Exp. [Hz]	FEM [Hz]	Diff.	Exp. [Hz]	FEM [Hz]	Diff.	Exp. [Hz]	FEM [Hz]	Diff.
Mode 1	"2-0"	70	73	4.5 %	71	75	4.9 %	69	73	5.1 %
Mode 2	"1-1"	99	103	3.6 %	97	102	4.7 %	100	104	4.0 %
Mode 3	"3-0"	192	199	3.8 %	196	206	5.1 %	196	206	5.0 %
Mode 4	"2-1"	210	221	4.9 %	214	224	4.3 %	208	219	5.1 %
Mode 5	"3-1"	347	357	2.8 %	353	369	4.3 %	367	381	3.8 %
Mode 6	"0-2"	386	396	2.3 %	**422**	**424**	**0.6 %**	**410**	**415**	**1.4 %**
Mode 7	"4-0"	424	432	2.0 %	**376**	**393**	**4.4 %**	**381**	**398**	**4.1 %**
Mode 8	"1-2"	443	445	0.6 %	450	454	0.8 %	443	451	1.7 %
Mode 9	"2-2"	567	578	1.9 %	**599**	**619**	**3.1 %**	**567**	**578**	**1.8 %**
Mode 10	"4-1"	575	603	4.6 %	**541**	**563**	**4.0 %**	**553**	**573**	**3.6 %**
Mode 11	"5-0"	656	681	3.6 %	679	713	4.8 %	675	711	5.1 %
Mode 12	"3-2"	737	747	1.4 %	767	788	2.7 %	777	810	4.0 %
Mode 13	"5-1"	825	862	4.2 %	845	886	4.7 %	847	892	5.0 %
Mode 14	"6-0"	970	1012	4.2 %	971			970		
Mode 15	"4-2"				998	1019	2.1 %	988	1023	3.4 %

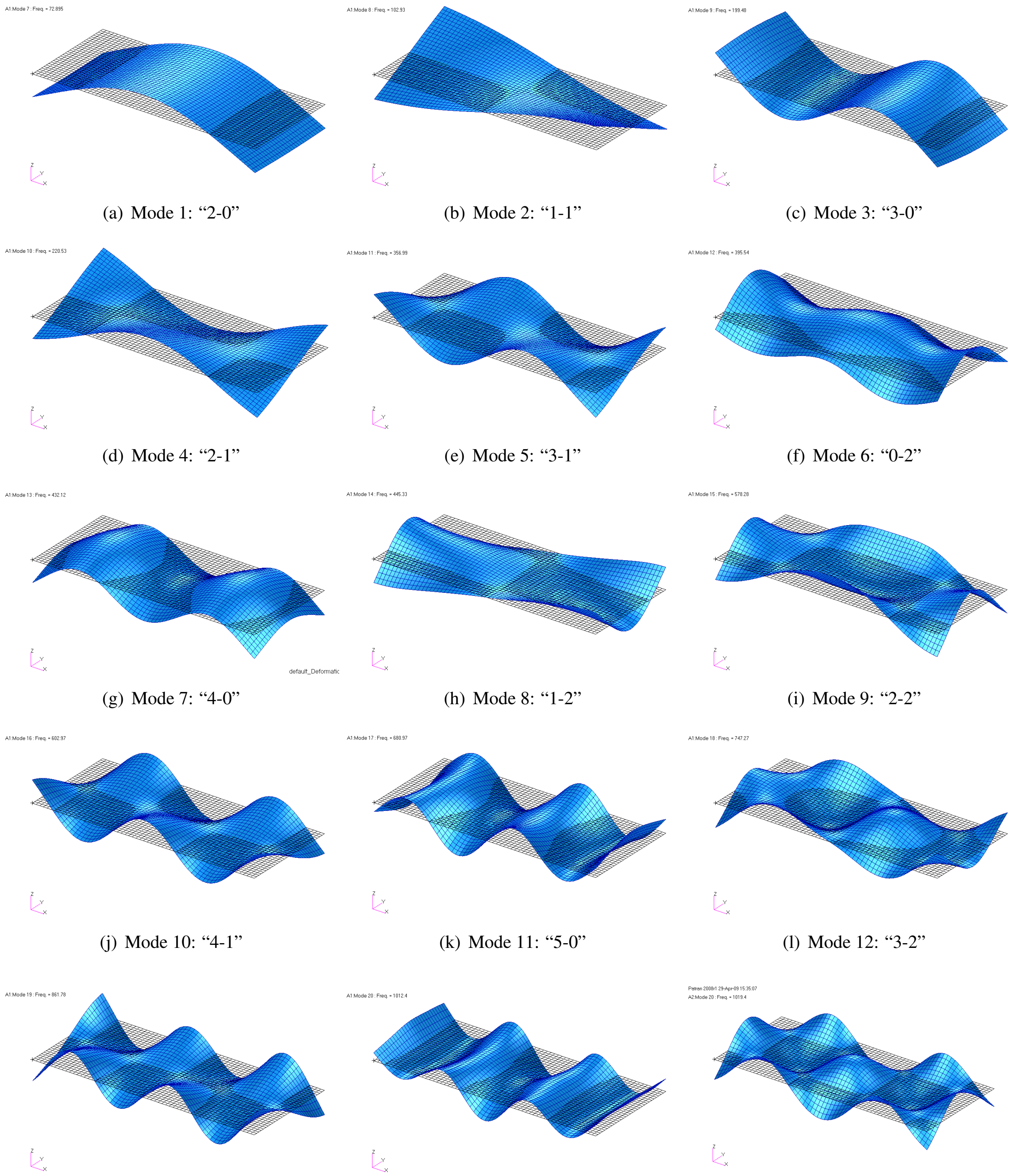

(a) Mode 1: “2-0” (b) Mode 2: “1-1” (c) Mode 3: “3-0”

(d) Mode 4: “2-1” (e) Mode 5: “3-1” (f) Mode 6: “0-2”

(g) Mode 7: “4-0” (h) Mode 8: “1-2” (i) Mode 9: “2-2”

(j) Mode 10: “4-1” (k) Mode 11: “5-0” (l) Mode 12: “3-2”

(m) Mode 13: “5-1” (n) Mode 14: “6-0” (o) Mode 15: “4-2”

Figure A.9: FEM calculated mode shapes

Bibliography

[1] R. J. Allemang. The modal assurance criterion – twenty years of use and abuse. *Sound and Vibration*, Aug. 2003.

[2] R. J. Allemang and D. L. Brown. Experimental modal analysis. In C. M. Harris and A. G. Piersol, editors, *Harris' Shock and Vibration Handbook*, chapter 11. McGraw-Hill, 5th edition, 2002.

[3] B. Allen, U. Lampater, et al. SOFIA Telescope Assembly Modal Survey Test Report. Technical report, CSA Engineering, Inc., 2008.

[4] P. Andersen. *ARTeMIS Extractor Online Help*. Structural Vibration Solutions A/S. Version 2010.

[5] P. Andersen. Technical paper on stochastic subspace identification techniques. ARTeMIS Extractor Online Help. Version 2010.

[6] E. Becklin et al. *The Science Vision for the Stratospheric Observatory For Infrared Astronomy*. NASA Ames Research Center, Moffet Field, CA, 2009.

[7] R. N. Bhattacharya and E. C. Waymire. *A Basic Course in Probability Theory*. Springer, 2007.

[8] R. E. Blake. Basic vibration theory. In C. M. Harris and A. G. Piersol, editors, *Harris' Shock and Vibration Handbook*, chapter 2. McGraw-Hill, 5th edition, 2002.

[9] R. Brincker and P. Andersen. Understanding Stochastic Subspace Identification. In *Proceedings of The 24th International Modal Analysis Conference (IMAC)*, St. Louis, Missouri, 2006.

[10] R. Brincker, P. Andersen, and N.-J. Jacobsen. Automated frequency domain decomposition for operational modal analysis. In *Proceedings of The 25th International Modal Analysis Conference (IMAC)*, 2007.

[11] R. Brincker, L. Zhang, and P. Andersen. Modal Identification From Ambient Responses Using Frequency Domain Decomposition. In *Proceedings of The 18th International Modal Analysis Conference (IMAC)*, pages 625–630, San Antonio, Texas, 2000.

[12] C. Eger. Erstellung einer generischen Prozess-Software in MATLAB für die Auswertung der SOFIA Flugversuchsdaten sowie Charakterisierung des Verhalten des Schwingungsisolations–Systems des Teleskops im Fluge. Diplomarbeit, Universität Stuttgart, Instut für Flugzeugbau, 2008.

[13] G. H. Golub and C. F. V. Loan. *Matrix computations*. Johns Hopkins University Press, 3rd edition, 1996.

[14] B. Greiner. *DSI Handbook for the Operational Modal Analysis Software ARTeMIS Testor and Extractor*. Deutsches SOFIA Institut, 2009.

[15] B. Greiner and U. Lampater. E-mail communication with Structural Vibration Systems A/S. May through Sept 2009.

[16] D. Hanson. *Operational Modal Analysis and Model Updating with a Cyclostationary Input*. PhD thesis, The University of New South Wales, Nov 2006.

[17] F. Harms. *A contribution to Characterizing and Calibrating the Pointing Control System of the SOFIA Telescope*. PhD thesis, Universität Stuttgart, Institute of Space Systems, May 2009.

[18] N.-J. Jacobsen, P. Andersen, and R. Brincker. Using EFDD as a robust technique to deterministic excitation in Operational Modal Analysis. In *Proceedings of The 2nd International Operational Modal Analysis Conference (IOMAC)*, Copenhagen, Denmark, 2007.

[19] N.-J. Jacobsen, P. Andersen, and R. Brincker. Applications of Frequency Domain Curve-fitting in the EFDD Technique. In *Proceedings of The 26th International Modal Analysis Conference (IMAC)*, Orlando, Florida, 2008.

[20] H. Kärcher. SOFIA Telescope Assembly Pointing Subsystem Description & Pointing Budget. SOF-SPE-MG-5000.0.01 Issue 03, MAN Technologies, 2000.

[21] T. Katayama. *Subspace Methods for System Identification*. Springer, 2005.

[22] U. Lampater. Study of the dynamic behavior of sofia's coarse balance weights by means of modal testing. Diplomarbeit, IRS-05-S02, Universität Stuttgart, Institut für Raumfahrtsysteme, 2005.

[23] U. Lampater. SOFIA Telescope Assembly Mode Ranking with respect to Observability in the focal plane using Modal Survey Test Data. SOF-DSI-TN-UKL004, Deutsches SOFIA Institut, Aug 2008.

[24] P. S. Maybeck. *Stochastic models, estimation, and control*, volume 1. Academic Press, 1979.

[25] N.N. *NI 4472 User manual*. National Instruments, May 2001. pp. 3-4 to 3-7.

[26] U. of Cincinnati Structural Dynamics Research Lab. Universal file formats for modal analysis testing. `http://www.sdrl.uc.edu/universal-file-formats-for-modal-analysis-testing-1`.

[27] E. Pfüller, M. Wiedemann, M. Burgdorf, F. Harms, and J. Wolf. First Line Operations with the SOFIA Fast Diagnostic Camera FDC. Test report, Deutsches SOFIA Institut, NASA Ames Research Center, Nov 2009.

[28] K. F. Riley, M. P. Hobson, and S. J. Bence. *Mathematical Methods for physics and engineering*. Cambridge University Press, 3rd edition, 2006.

[29] D. Simon. *Optimal State Estimation*. Wiley, 2006.

[30] P. Stoica and R. Moses. *Spectral Analysis of Signals*. Prentice Hall, 2005.

[31] P. van Overschee and B. D. Moor. *Subspace Identification for Linear Systems*. Kluwer Academic Publishers, 1996.

Declaration

I hereby affirm that this thesis has been written by myself and is based on my own work. No illegitimate appliances have been used. All sources have been referenced and are listed in the bibliography. Where illustrations from foreign sources have been used, they have been marked accordingly.

Erklärung

Ich erkläre hiermit, dass ich die vorliegende Studienarbeit selbständig angefertigt habe und diese auf meiner eigenen Arbeit beruht. Es wurden keine unerlaubten Hilfsmittel verwendet. Alle benutzten Quellen wurden referenziert und sind im Literaturverzeichnis aufgeführt. Alle Abbildungen, denen fremde Quellen zugrunde liegen, sind als solche gekennzeichnet.

Stuttgart, den 22. Dezember 2009